INFORMATION TO USERS

This manuscript has been reproduced from the microfilm master. UMI films the text directly from the original or copy submitted. Thus, some thesis and dissertation copies are in typewriter face, while others may be from any type of computer printer.

The quality of this reproduction is dependent upon the quality of the copy submitted. Broken or indistinct print, colored or poor quality illustrations and photographs, print bleedthrough, substandard margins, and improper alignment can adversely affect reproduction.

In the unlikely event that the author did not send UMI a complete manuscript and there are missing pages, these will be noted. Also, if unauthorized copyright material had to be removed, a note will indicate the deletion.

Oversize materials (e.g., maps, drawings, charts) are reproduced by sectioning the original, beginning at the upper left-hand corner and continuing from left to right in equal sections with small overlaps.

Photographs included in the original manuscript have been reproduced xerographically in this copy. Higher quality 6" x 9" black and white photographic prints are available for any photographs or illustrations appearing in this copy for an additional charge. Contact UMI directly to order.

Kinetic Processes in the Plasma Sheet Observed during Auroral Activity

Matthew Owen Fillingim

.

A dissertation submitted in partial fulfillment
of the requirements for the degree of

Doctor of Philosophy

University of Washington

2002

.

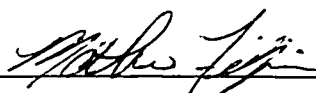Program Authorized to Offer Degree: Geophysics Program

UMI Number: 3041021

UMI®

In presenting this dissertation in partial fulfillment of the requirements for the Doctoral degree at the University of Washington, I agree that the Library shall make its copies freely available for inspection. I further agree that extensive copying of this dissertation is allowable only for scholarly purposes, consistent with "fair use" as prescribed in the U.S. Copyright Law. Requests for copying or reproduction of this dissertation may be referred to Bell and Howell Information and Learning, 300 North Zeeb Road, Ann Arbor, MI 48106-1346, to whom the author has granted "the right to reproduce and sell (a) copies of the manuscript in microform and/or (b) printed copies of the manuscript made from microform."

Signature_____

Date__3/19/02_____

University of Washington

Graduate School

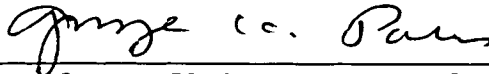This is to certify that I have examined this copy of a doctoral dissertation by

Matthew Owen Fillingim

and have found that it is complete and satisfactory in all respects,
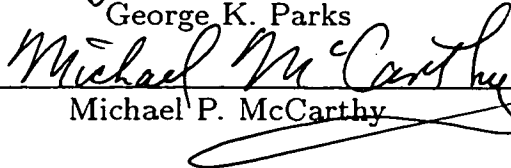
and that any and all revisions required by the final

examining committee have been made.
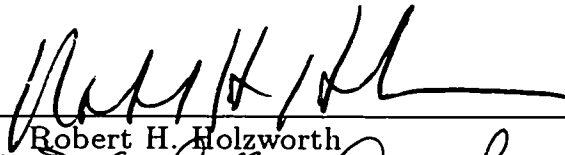
Co-Chairs of Supervisory Committee:
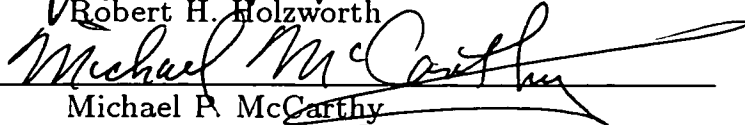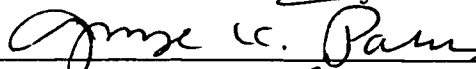
George K. Parks

Michael P. McCarthy

Reading Committee:

Robert H. Holzworth

Michael P. McCarthy

George K. Parks

Robert M. Winglee

Date: 3/19/02

University of Washington

Abstract

Kinetic Processes in the Plasma Sheet Observed during Auroral Activity

by Matthew Owen Fillingim

Co-Chairs of Supervisory Committee:

Professor Emeritus George K. Parks
Geophysics Program

Research Associate Professor Michael P. McCarthy
Geophysics Program

In this dissertation we analyze plasma sheet magnetic field and plasma data observed during varying levels of auroral activity from very small, isolated events known as pseudobreakups to large, global events known as substorms. The plasma and magnetic field data are taken from instruments onboard the WIND spacecraft while it traverses the near-Earth plasma sheet. Simultaneous global auroral images from PO-LAR/UVI allow us to determine the auroral activity level. The goal of this dissertation is to provide the most complete set of plasma sheet observations during auroral activity currently available. The kinetic aspects of the plasma dynamics which have largely been ingnored in other works are emphasized here. We have the capability to resolve changes in the three dimensional ion distribution functions with a time resolution comparable to or faster than the local ion gyroperiod. In addition, we consider the typically neglected electron dynamics when relating plasma sheet processes to the aurora. We find that the plasma sheet signatures of both pseudobreakups

and substorms appear very similar. During both types of events, increases in auroral precipitation into the ionosphere are associated with large amplitude, high frequency magnetic field fluctuations, large Earthward ion $\langle v \rangle$, increases in the fluxes of high energy ions and electrons, and hardening of the electron spectrum. Both ion and electron distributions appear to be composed of multiple components. Electromagnetic waves with power at frequencies up to and above the local proton gyrofrequency area also observed. Additionally, the ion distributions can change significantly in one gyroperiod. Together, these results imply that the microphysical processes occurring in the plasma sheet during pseudobreakups and substorms are the same and that kinetic effects are important. Therefore, magnetohydrodynamics (MHD) cannot adequately describe the physics occurring during large ion $\langle v \rangle$ events.

TABLE OF CONTENTS

LIST OF FIGURES

LIST OF TABLES

ACKNOWLEDGMENTS

are countless others who have regretfully been excluded because I don't have space on the page or in my brain to include them all.

Just about every member of the faculty, staff, and students of the Space Physics group and the Geophysics Program in general (and a few in Geological Sciences now that we've combined to form the Department of Earth and Space Sciences), past and present, have each in their own way contributed to my education and experience. I would like to acknowledge my office mates in particular, past and present, for their help and camaraderie. They include (in alphabetical order) Dr. Ben Barnum, Dr. Li-Jen Chen, Damien Chua, Dr. Kerry Deutch (to whom I am indebted for housing me when I came to visit the University and for housing my wife and me for several days while we were looking for a place to live), Dr. Kirsten Lorentzen, Andrew Meadows, Carol Paty, Jeremy Thomas (two recent additions), and John Williams. These and other friends from the University of Washington, from Seattle, and those scattered around the world have helped me to keep my sanity somewhat intact by offering their experience and encouragement and simply being there.

My family and my wife's family deserve the utmost recognition for continuously supporting us and encouraging us to follow our dreams now and always and for understanding our absences throughout several family tragedies.

Most importantly, I need to thank Michelle. Her unwavering desire for me to finish kept me moving forward, and all of her sacrifices have made this possible. (See the Dedication page.) Now it's payback time.

DEDICATION

One more time, to Michelle.

> You moved 3,000 miles from everything you knew and loved.

> You delayed your dreams so I could follow mine.

> You supported me.

> You endured.

> All of this and more for me.

> That's love.

This is also dedicated to the memory of

> Clara Frances (Gardner) Wilson (1917 – 1998)

> Joseph Edwin Fillingim (1922 – 2000)

> Angela Ruth (Wilson) Russ (1959 – 2001)

who left while I was gone.

Chapter 1

INTRODUCTION

Auroral displays can be very dynamic and can transfix an auroral observer for hours. The active aurora is just one manifestation of activity which occurs throughout large regions of Earth's magnetosphere. The auroral ionosphere acts like the television screen of the magnetosphere. Energetic particles from the magnetosphere are guided by Earth's magnetic field toward high latitude regions where they collide with the atoms and molecules of the atmosphere. The excited atmospheric atoms and molecules then emit light similar to the phosphor which coats television screens.

The plasma sheet is the part of the magnetosphere that is magnetically linked to the auroral regions. There is evidence that the dynamics of the plasma sheet are intimately associated with the aurora [*Hones et al.*, 1976; *Fairfield et al.*, 1999]. However, the causal relationship has not been established. Therefore, in order to understand the aurora, we need to understand the processes in the plasma sheet that give rise to the aurora. The current understanding of the plasma dynamics in the plasma sheet is based on observations of the behavior of macroscopic plasma parameters, such as density, velocity, and temperature [*Baumjohann et al.*, 1990; *Angelopoulos et al.*, 1992; *Fairfield et al.*, 1999]. These parameters are normally obtained on time scales as long as tens of seconds, much longer than the typical plasma time scales. With the exception of *Hada et al.* [1981], most previous work has also ignored the electron behavior. These data to not give a full picture of the processes responsible for the dynamics of the plasma sheet. It is becoming increasingly

clear that it is important to base our understanding of the plasma sheet dynamics on higher time resolution data and also to include the behavior of the electrons.

The purpose of this dissertation is to contribute to the understanding of the plasma sheet behavior during different kinds of auroral activity from very small, isolated events to large, global events. To this end we systematically analyze the plasma in the near-Earth plasma sheet with a resolution and detail not previously done so that a more comprehensive picture of the dynamics is obtained. We emphasize the kinetic aspects of the plasma and do not just focus on the bulk properties as is usually the case. In addition, we include the often neglected electron behavior in our analysis. We begin by studying the plasma sheet during small, isolated auroral events known as pseudobreakups [*Elvey*, 1957]. Then we compare these observations with those from expansive auroral events known as substorms [*Akasofu*, 1964], looking for similarities and differences in the plasma sheet dynamics.

A detailed examination of the processes occurring in the plasma sheet during periods of active aurora can lead to a better understanding of the physical mechanisms which give rise to these processes. By studying the plasma behavior during different levels of auroral activity, we can investigate the effects of the local plasma sheet properties on the size of the aurora. These effects are associated with how mass and energy are transported throughout the magnetosphere and how plasma sheet processes are related to the generation of the aurora.

In the following sections, we will briefly survey the large scale structure of the magnetosphere and discuss how different magnetospheric regions are connected. Then we will introduce the concept of a substorm using both auroral and magnetospheric observations. We contrast observations of substorms with those of pseudobreakups and describe several of the prevailing theories attempting to explain the differences between these two types of auroral phenomena. Finally we will discuss some of the differences between the kinetic and fluid approaches to describing the plasma dynamics and some of the limitations associated with the fluid formulation.

1.1 Earth's Magnetosphere

Earth's magnetosphere is that region of space which is carved out of the solar wind by Earth's magnetic field. Figure 1.1 shows a simplified diagram of Earth's magnetosphere. Pertinent regions of the magnetosphere have been labeled. As the supersonic solar wind impinges upon Earth's magnetic field, it slows to subsonic speeds at the bow shock. The slowed, thermalized solar wind plasma flows around Earth through the magnetosheath between the bow shock and the magnetopause, the boundary of the magnetosphere. On the side facing the Sun, the magnetosphere is compressed; on the nightside, it is stretched out to form a long magnetotail. Observations of oppositely directed magnetic field in the northern and southern portions of the magnetotail indicate that a current sheet exists near the equator separating these two hemispheres. The region of hot plasma near the equator that encompasses the current sheet is known as the plasma sheet. The lines of magnetic force that thread the plasma sheet map down to the ionosphere in the auroral regions. Active auroral displays are created when the energetic particles of the plasma sheet are brought close to Earth and collide with the atoms and molecules of the atmosphere.

The Sun is the ultimate energy source for the magnetosphere's dynamics. The solar wind transfers energy to the magnetosphere, although the exact processes by which this occurs are not well understood. Magnetic and plasma energy stored in the magnetotail are episodically released and brought toward Earth, commonly in a series of events known as a magnetospheric substorm (see Section 1.3). This energy is then dissipated in processes resulting in active auroral displays and atmospheric heating at high and middle latitudes and in processes leading to the formation of the radiation belts at equatorial latitudes. What causes this "explosive" energy release, and how the energy is transported Earthward are subjects of intense study.

As shown in Figure 1.1, the auroral region is linked magnetically to the distant regions of the magnetosphere and plasma sheet. Global auroral images can thus
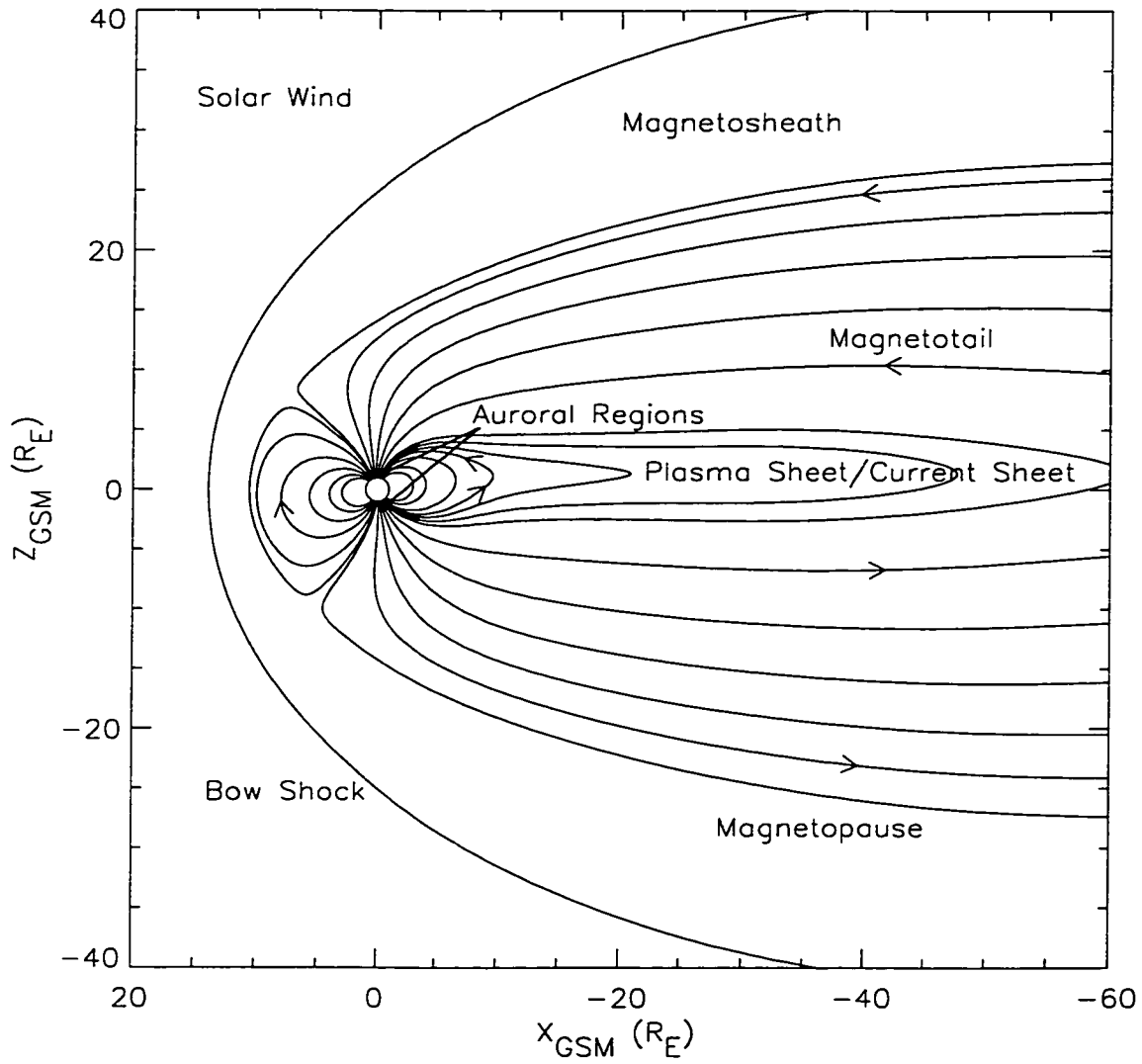
Figure 1.1: A simplified diagram of Earth's magnetosphere. The X-axis points toward the Sun. Earth's magnetic dipole axis lies in the X-Z plane. The arrows indicate the direction of the magnetic force.

provide a global perspective of activity in the plasma sheet not available from single point in situ measurements. However, in situ satellite measurements are necessary for a detailed look at the physical processes occurring in the plasma sheet. To try to understand what active processes in the magnetosphere are associated with aurora, we combine global auroral images with plasma and magnetic field observations made in the near-Earth plasma sheet.

1.2   Auroral Substorm

A ground or space-based observer of the aurora will notice, after an adequate length of time, a somewhat repeatable global pattern of increasing intense auroral emission followed by subsidence. This global pattern was first described by *Akasofu* [1964], and is termed an auroral substorm.

Figure 1.2 illustrates some of the features of an auroral substorm. This early picture was derived from multiple, simultaneous, ground-based observations. The pattern begins with the aurora in a quiescent state (A). From the ground, an observer may see a series of stable auroral arcs. From space, the aurora appears as a rather diffuse band encircling the entire polar region known as the auroral oval. Occasionally, typically one or more times per day depending upon solar activity, the equatorward-most portion of the aurora brightens abruptly near local midnight (B). This is termed the "breakup" or onset of the expansive phase. The region of intense emission then rapidly expands in latitude and longitude in tens of minutes (C, D). Intense currents flowing through the ionosphere, which can be measured with ground based magnetometers, are associated with the bright auroral emissions. Once the region of intense auroral emission reaches its maximum size and ceases its poleward expansion, the substorm is said to have entered the recovery phase (E, F). During the recovery phase, the intensity of the auroral emission decreases and the region of emission retreats equatorward over the course of a few hours. In some cases, auroral
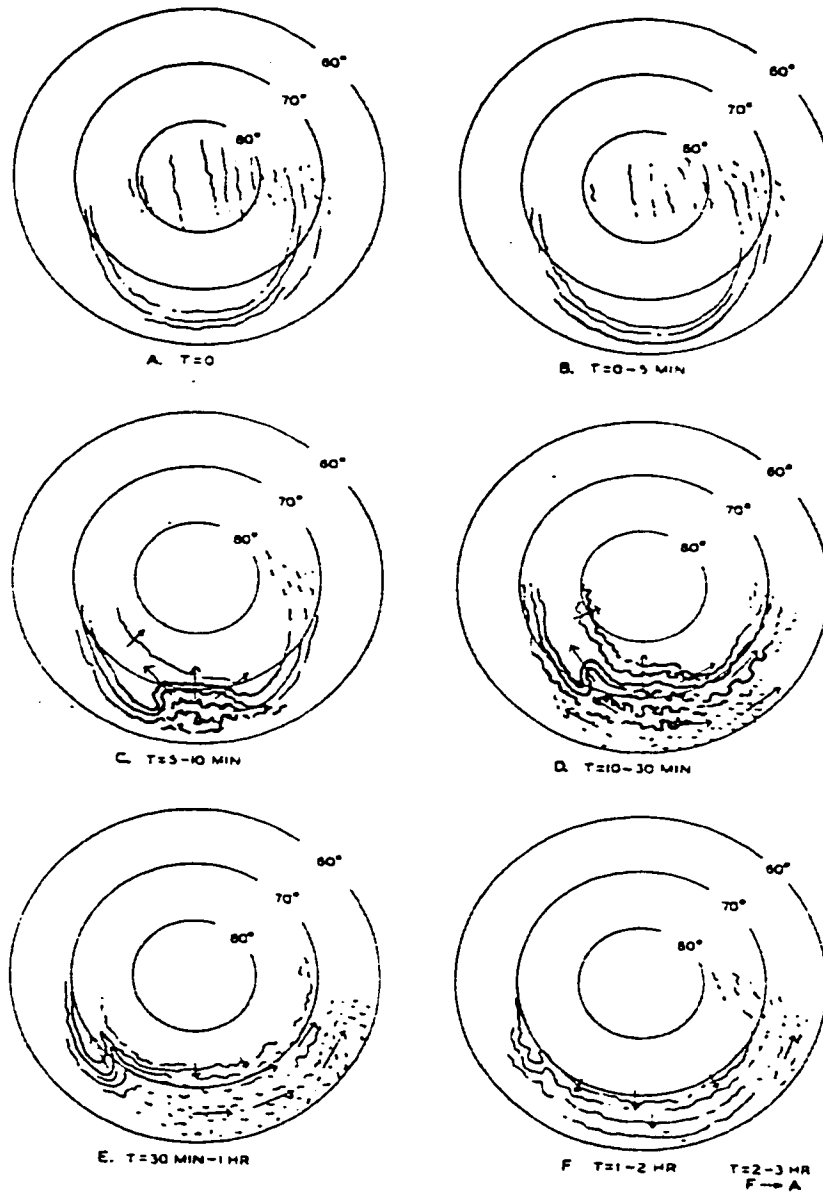
Figure 1.2: A schematic diagram illustrating the phases of an auroral substorm (from *Akasofu* [1964]).

activity may continue in the poleward portions of the auroral oval, and additional intensifications similar to and as intense as the onset of the expansive phase may occur during the recovery phase.

A modern version of the observations summarized in Figure 1.2 is shown in Figure 1.3, where a sequence of global auroral images taken by the UltraViolet Imager (UVI) onboard the POLAR spacecraft on 12 January 1997 is presented. As in the previous figure, the images are in magnetic coordinates with the Sun toward the top of the page and local midnight at the bottom. The aurora is not continuous on the dayside in the last three images because the entire auroral region does not lie within the UVI field of view at these times. Compare the images with the drawings in Figure 1.2. The top left image shows the global aurora in the quiet state. The initial brightening occurs in the top right image near 07:25 UT. Over the next several minutes, the aurora expands poleward and in longitude. Several intensifications occur during the next hour or so. Near 08:14 UT the region of intense emission reaches its most poleward point. The intensity of the emission decreases as the aurora begins to retreat equatorward. In this example the region of moderate emission persists at high latitudes on the dawnside. Several hours after onset, the aurora returns to its quiescent state.

Later researchers noticed that the entire auroral region can move equatorward during the hour or so before the initial onset. The original two phase description of the auroral substorm by *Akasofu* [1964] was then amended to include a "growth phase" [*McPherron*, 1970] immediately preceding the expansive phase.

1.3   Magnetospheric Substorm

Once the "Space Age" began with the launch of Earth orbiting satellites, it was possible to study the magnetospheric environment in situ. Over the past several decades, many studies have been done relating the magnetospheric plasma and magnetic field

1997-01-12 07:21:50 UT
1997-01-12 07:24:54 UT
1997-01-12 07:27:58 UT
1997-01-12 08:13:58 UT
1997-01-12 08:44:38 UT
1997-01-12 10:08:03 UT
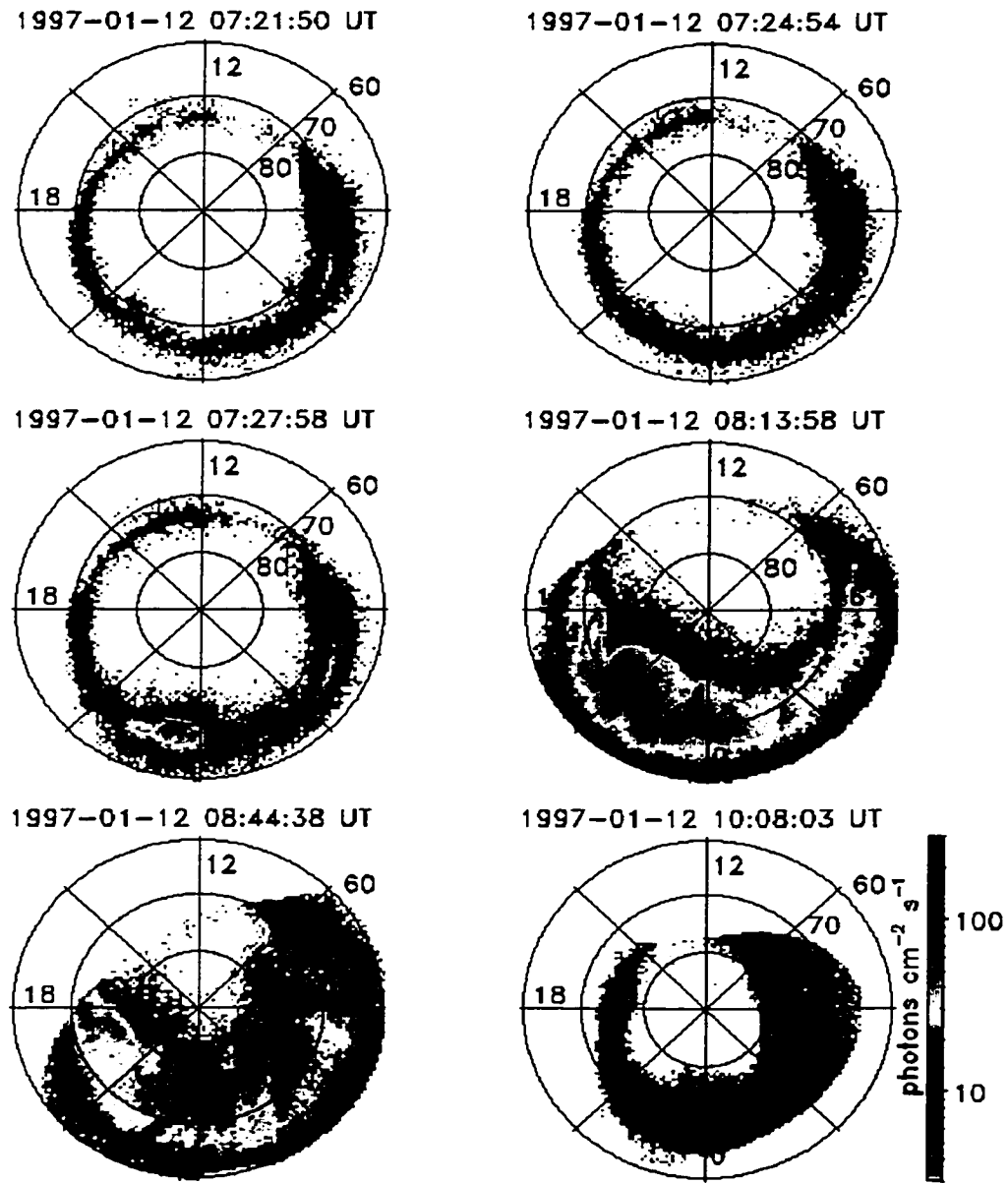
Figure 1.3: A sequence of global auroral images showing the phases of an auroral substorm.

properties to auroral substorm phase. Early on it was noted that a wide variety of magnetospheric processes were correlated with auroral substorms, hence the term "magnetospheric substorm" [*Coroniti et al.*, 1968] (as mentioned in Section 1.1) was coined to describe the accompanying magnetospheric processes.

The magnetospheric processes described here will be limited to those observed in the near-Earth plasma sheet, $X \sim -10$ to -20 R_E near the equatorial plane, since it is in this region that the data presented in this dissertation are observed. This region plays an important role in the development of substorms. Magnetic field models show that the location of the initial auroral brightening maps to this region in the equatorial magnetosphere. This is also the region of the magnetosphere where the magnetic field transitions from "tail-like" tailward of this region to dipolar Earthward of this region, as can be seen in Figure 1.1. This transition region figures prominently in several models of substorm initiation and development.

During the growth phase when the quiet aurora is drifting equatorward, particle instruments often detect decreases in both the electron and ion fluxes known as "particle dropouts" [*Hones et al.*, 1967]. At the same time, the direction of the magnetic field becomes predominantly in the X-direction, that is, the magnetic field is said to become more "stretched" and "tail-like" [*McPherron*, 1972]. These two observations are interpreted to imply that the plasma sheet thins and the cross tail current becomes more intense during the growth phase [*Kaufmann*, 1987].

At the onset of the expansive phase, the particle fluxes recover very rapidly. Usually, energetic particles fluxes recover to more intense levels than pre-dropout levels. The Z-component of the magnetic field increases and the X-component of the magnetic field decreases leading to a "dipolarization" of the tail field. Often there is an accompanying perturbation in the Y-component [*Cummings et al.*, 1968]. More recent studies [*Angelopoulos et al.*, 1997; *Fairfield et al.*, 1999] have suggested that a substorm onset is also accompanied by intervals of fast ion velocities in the plasma sheet known as bursty bulk flows (BBFs) [*Angelopoulos et al.*, 1992]. These authors

have proposed that BBFs are responsible for the Earthward transport of mass, energy, and magnetic flux from the tail.

For a more detailed look at what happens in the magnetosphere during a magnetospheric substorm, the reader is referred to the review article by *McPherron* [1979] and the references contained therein, to *Sauvaud et al.* [1987], and to *Parks* [1991].

1.4   Pseudobreakup Aurora

Not every type of auroral activity is classified as an auroral substorm. An observer of the aurora will notice that occasionally the aurora may abruptly brighten, but, instead of rapidly advancing poleward, it will fade over the course of a few minutes. This is termed a "pseudobreakup" and was first described in the scientific literature by *Elvey* [1957]. Both *Elvey* [1957] and *Akasofu* [1964] noted that a pseudobreakup was usually the result if the initial brightening was not at the equatorward edge of the aurora; that is, pseudobreakups usually occur poleward of substorm onset. However, this is not always the case. For example, *Nakamura et al.* [1994] reported that a major expansion onset on January 8, 1986, occurred poleward of the pseudobreakup region which was active 5 to 10 minutes earlier.

In Figure 1.4 another set of UVI images shows a pseudobreakup followed by a substorm. The initial auroral brightening occurs near 07:19 UT. The aurora brightens over the next few minutes, reaching maximum intensity near 07:22 UT. Then, rather than expanding as a substorm, the region of intense emission decreases in size as the aurora fades.

The aurora brightens again at 07:47 UT, nearly 30 minutes after the initial brightening. This brightening appears very much the same as the first brightening in terms of scale size and location. This time, however, the region of intense emission continues to expand, reaching its maximum extent in about an hour. Comparing the image taken at 08:39 UT in Figure 1.4 with the image taken at 08:13 UT in Figure 1.3, it is

noted that there is not much difference between the area covered by intense emission and only a minor difference in the intensity; they appear quite similar.

In the aurora, a pseudobreakup appears as an auroral substorm onset, or breakup, which is not followed by a global expansion. Often pseudobreakups are noticed before a substorm expansion during the growth phase and are typically discussed as growth phase phenomena [McPherron, 1991]. However, pseudobreakups are also seen in the auroral data during relatively quiet periods [Berkey and Kamide, 1976; Fillingim et al., 2000] and during substorm recovery and periods of enhanced continuous activity [Sergeev et al., 1986; Aikio et al., 1999]. These observations show that pseudobreakups and the magnetospheric processes associated with them occur over a wide variety of magnetospheric conditions.

1.5 Magnetospheric Observations of Pseudobreakups

Several case studies [Sergeev et al., 1986; Koskinen et al., 1993; Ohtani et al., 1993; Nakamura et al., 1994; Rostoker, 1998; Aikio et al., 1999] using both ground and satellite based observations have shown that pseudobreakups are associated with many of the same features as substorm onsets. On the ground, weak magnetic deflections indicative of currents flowing through the ionosphere have been observed, as well as weak magnetic pulsations. In the magnetotail, magnetic field dipolarizations, energetic particle injections, and fast ion velocities both Earthward and tailward have been measured. However, these features are much more localized and short lived in the case of pseudobreakups than for substorm onset.

Many of these results have suggested that, in the right location in the magnetotail, pseudobreakup signatures can be as intense as those seen at substorm onset. However, the effects fall off rapidly with distance. Therefore, from a single point measurement, it is impossible to tell whether a pseudobreakup or a substorm is occurring. Several authors also noted that the physical process responsible for pseudobreakups is the

1997-01-09 07:16:36 UT

1997-01-09 07:19:40 UT

1997-01-09 07:22:44 UT

1997-01-09 07:44:12 UT

1997-01-09 07:47:16 UT

1997-01-09 08:39:24 UT
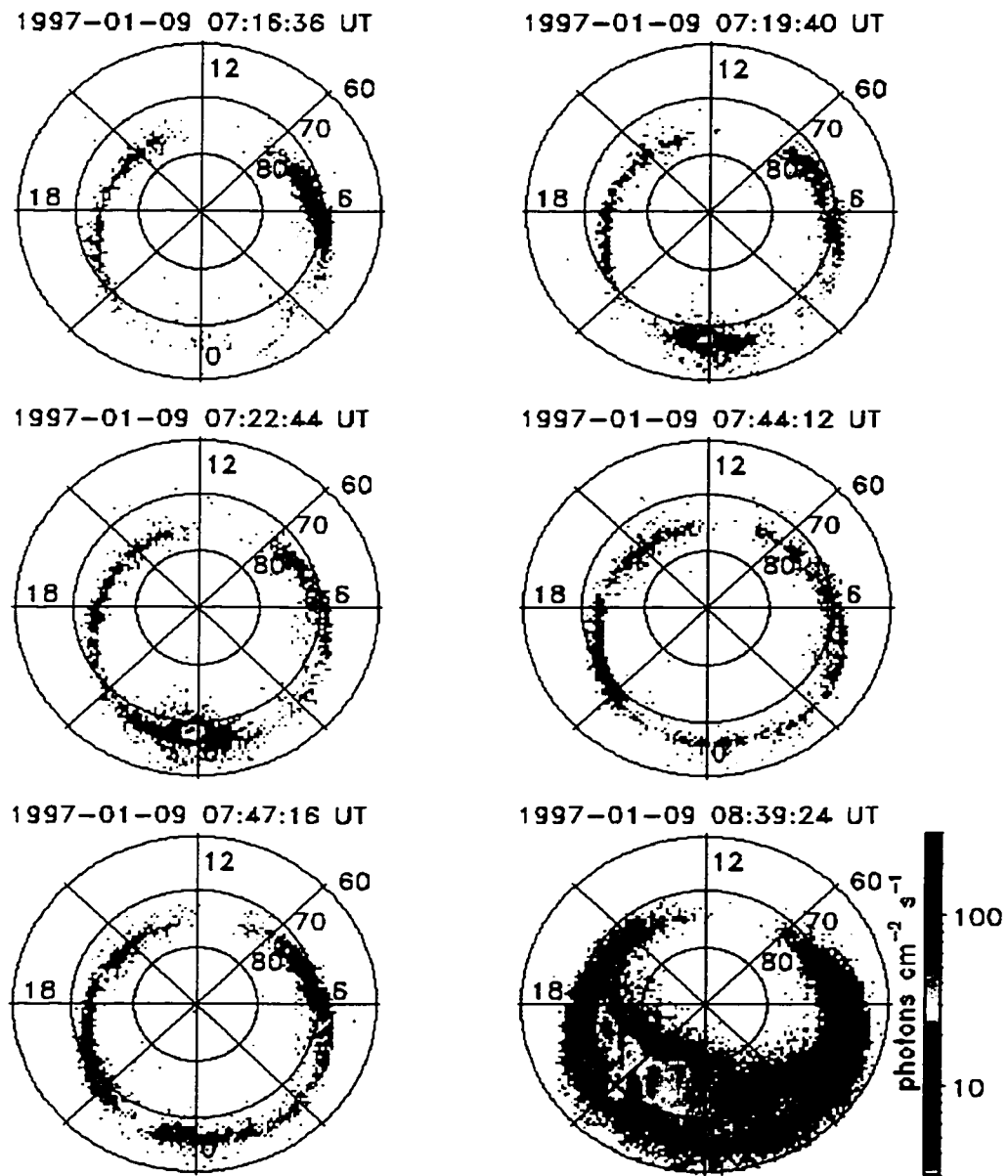
Figure 1.4: A sequence of global auroral images showing a pseudobreakup followed by a substorm.

same as that for substorm onset, and that the only observable difference between pseudobreakups and substorm onset is the size and duration of the auroral features and the global magnetospheric consequences.

A natural question arising from this comparison is what physical mechanism prevents a pseudobreakup from expanding globally. Several phenomenological models have been put forward to explain the absence of an expansion phase during a pseudobreakup. These can be divided into three broad categories: solar wind-magnetosphere coupling, magnetosphere-ionosphere coupling, and internal magnetospheric control.

1.5.1 Solar Wind-Magnetosphere Coupling

Since it is generally regarded that the transfer of momentum and energy from the solar wind to the magnetosphere provides the energy to power magnetospheric phenomena, the pseudobreakup observed by *Koskinen et al.* [1993] was inferred to have occurred before sufficient energy was input into the magnetosphere to power a substorm expansion phase onset. They observed a period of enhanced solar wind input, signified by a southward directed interplanetary magnetic field (IMF), punctuated by a brief northward excursion of the IMF and followed by a pseudobreakup. Following the pseudobreakup, an even higher solar wind energy input rate followed by a northward turning of the IMF and a substorm expansion was observed. Similarly, *Nakamura et al.* [1994] concluded that the amount of energy stored in the magnetotail is the dominant factor in determining whether an onset will expand globally (a substorm) or remain localized (a pseudobreakup), though they stated that the release of energy is triggered by an internal magnetospheric instability.

In contrast, calculations by *Pulkkinen* [1996] suggest that there is always enough energy present in the magnetotail to power a substorm expansion phase. In a later work, *Pulkkinen et al.* [1998] hypothesized that continuing energy input into the magnetosphere may somehow play a role in quenching the growth of whatever instability process is responsible resulting in a pseudobreakup rather than a substorm. *Rostoker*

[1998] also suggested that pseudobreakups occur during periods of increasing energy input from the solar wind into the magnetotail while substorm onset is associated with a decline in the rate of energy input into the magnetotail.

Arballo et al. [1998] reported a sequence of several pseudobreakups shortly after the arrival of a solar wind pressure pulse with a northernly directed magnetic field. The Y- (duskward) component of the solar wind magnetic field following the pressure pulse oscillated with a quasiperiod of about 10 minutes. They suggested that the solar wind B_Y may have been related to the quasiperiodicity of the pseudobreakup sequence. All of these theories imply that solar wind-magnetosphere energy coupling may play the dominant role in preventing a pseudobreakup from expanding globally.

1.5.2 Magnetosphere-Ionosphere Coupling

It has been suggested that the ionospheric conductivity may play an important role in determining whether a pseudobreakup or substorm expansion will occur. Theories proposed by *Kan et al.* [1988] and by *Lui* [1991] explicitly include the occurrence of a pseudobreakup during conditions in which the ionospheric conductivity and gradients in the ionospheric conductivity are insufficient to allow the development of a strong current system in the ionosphere associated with substorm onset and expansion.

Nakamura et al. [1994] asserted that ionospheric conductivity, being the result of auroral precipitation, would have only a secondary effect. Observations of *Aikio et al.* [1999] do not show any evidence of a change in ionospheric conductivity from pseudo-breakup to substorm. However, they did not measure gradients in the conductivity, which is one of the important parameters in the model presented by *Kan et al.* [1988].

In the model proposed by *Erickson et al.* [1996], the ionospheric conditions must be such that an Alfvén wave launched from the equatorial region of the magnetosphere be reflected in phase for a substorm to expand. If the reflection from the ionosphere is out of phase, growth is quenched and a pseudobreakup is the result. *Koskinen et al.* [1993], *Ohtani et al.* [1993], and *Pulkkinen* [1996] did not rule out the possibility that

the condition of the ionosphere may play a role in inhibiting the global expansion of a substorm.

1.5.3 Internal Magnetospheric Control

Finally, another group of theories specifies that the conditions in the magnetosphere are responsible for controlling the growth of magnetospheric instabilities which lead to substorm phenomena, or, if growth is inhibited, pseudobreakups. Even though the ultimate energy source for magnetospheric processes is the solar wind, *Pulkkinen* [1996] stressed that the local conditions in the tail are important in the development of a large-scale instability leading to substorm expansive phase onset. Similarly, *Parks et al.* [2002] argued that the local properties such as the amount of free energy contained in the ambient plasma distributions determine the size and intensity of auroral and plasma sheet disturbances. *Ohtani et al.* [1993] proposed that the magnitude and spatial gradients of magnetic distortions in the magnetotail may be sufficient to quench the growth of an instability and thus prevent a global expansion. The mechanism, however, by which magnetic distortion inhibits instability growth was not proposed. It is very difficult to test these types of hypotheses with single point in situ measurements since the local properties in the plasma sheet vary from place to place with unknown spatial scales.

1.6 Magnetohydrodynamics (MHD)

In order to completely describe the plasma dynamics in the magnetosphere, it is necessary to know the position and velocity of every particle. Therefore, we have 6N variables, where N is the number of particles, plus time and the electric and magnetic fields. Even in a region as sparsely populated as the magnetotail where densities are of the order of one particle per cubic centimeter (1 cm^{-3}) or less, this requires an unrealistically huge amount of data and computational power. To simplify matters,

moments of the velocity phase space distribution function are commonly used to describe the plasma dynamics. This simplification reduces the 6N variables to three quantities:

- scalar density $(n(\mathbf{r},t) = \int_{-\infty}^{\infty} f(\mathbf{r},\mathbf{v},t)d\mathbf{v}$, where $f(\mathbf{r},\mathbf{v},t)$ is the distribution function);

- mean velocity vector $(\langle\mathbf{v}\rangle = \frac{1}{n}\int_{-\infty}^{\infty} \mathbf{v}f d\mathbf{v})$; and

- mean square velocity tensor $(\langle\mathbf{ww}\rangle = \frac{1}{n}\int_{-\infty}^{\infty}(\mathbf{v}-\langle\mathbf{v}\rangle)(\mathbf{v}-\langle\mathbf{v}\rangle)f d\mathbf{v}$, where $\mathbf{w} = \mathbf{v}-\langle\mathbf{v}\rangle)$, which can be related to pressure and temperature.

(For an in depth description of the velocity phase space distribution function and moments of the distribution function, the reader is referred to *Parks* [1991].)

This averaging of the distribution function necessarily involves a loss of information as 6N variables are reduced to 10 (the mean square velocity tensor is symmetric, composed of only 6 independent variables). By using moments of the distribution function, the plasma, a rarefied collection of charged particles interacting via electromagnetic forces, is, in effect, described as a fluid. The study of this magnetized fluid is known as magnetohydrodynamics (MHD). Fluid behavior usually arises due to the effects of collisions between particles. Space plasmas, in general, are collisionless. However, particles can interact though electromagnetic "collisions," e.g., long range interactions due to the Coulomb force.

Inherent in the MHD formulation is the assumption that the plasma can be accurately described by the three parameters density, velocity, and pressure (or temperature). That is, the plasma must be composed of a single component and behave as a fluid in the usual sense. Consider the case of two counter streaming beams of equal intensities and moving at equal but opposite speeds. By only looking at the moments, the conclusion is that the plasma is stagnant with a zero $\langle\mathbf{v}\rangle$ and has a physically

meaningless temperature. An MHD analysis would miss the presence of these beams and give an incomplete picture of the plasma dynamics.

Another limitation of MHD is the problem of closure. The reduction in the number of variables also requires a reduction in the number of equations relating the variables. As a result, in the MHD formulation, there are fewer equations than unknowns; the system is indeterminate. Additional, sometimes quite restrictive, properties of the fluid must be assumed to close the set of equations.

The typical hydrodynamic formulation for ordinary fluids is only valid over time scales greater than the time between collisions and over length scales longer than the distance a particle travels between collisions. Since space plasmas are usually collisionless, these criteria are insufficient. The MHD formulation for space plasmas does not follow the trajectories of individual particles; the gyro motion of charged particles about the magnetic field are "averaged out." Hence, in the MHD formulation, the temporal scales must be longer that the gyroperiod and the spatial scales larger than the gyroradius. Therefore, if the region of interest is smaller than the gyroradius or if the time interval of interest is shorter than the gyroperiod or if the plasma doesn't behave as a single fluid, then the MHD description is not accurate.

MHD calculations and simulations have reasonably described the global features of Earth's magnetosphere. Plasma sheet dynamics are also often described and interpreted in the MHD framework. Many authors justify this interpretation by citing the work of *Nakamura et al.* [1991]. *Nakamura et al.* [1991] analyzed several distributions observed in the plasma sheet near the current sheet. They concluded that even though the mean bulk velocity, $\langle v \rangle$, can be very large as noted previously by *Baumjohann et al.* [1990], the plasma is typically composed of a single component. In a later study, *Nakamura et al.* [1992] found that, during periods of large ion $\langle v \rangle$, the plasma in the outer portion of the plasma sheet (the plasma sheet boundary layer, PSBL) is not composed of just a single component, in agreement with previous work [*Eastman et al.*, 1984; *Takahashi and Hones*, 1988].

Since the plasma is assumed to be composed of a single component, and since a significant fraction of the mean velocity is directed perpendicular to the ambient magnetic field [*Baumjohann et al.*, 1990; *Angelopoulos et al.*, 1992], bursty bulk flows (BBFs) are thought to be caused by large duskward directed electric fields. The resulting velocity, $\mathbf{v} = \mathbf{E} \times \mathbf{B}/B^2$, is primarily in the Earthward direction. This leads to a net transport of mass, energy, and magnetic flux toward Earth from the tail to fuel the aurora.

More recent observations suggest that the single component assumption may not always be valid in the plasma sheet [*Chen et al.*, 2000a, b; *Parks et al.*, 2001]. *Chen et al.* [2000a] have studied the plasma distributions near the current sheet and have shown that the plasma, at times, may be composed of multiple components. Additionally, *Chen et al.* [2000b] have shown that only a fraction of the total ion $\langle \mathbf{v} \rangle$ during some BBFs is in the $\mathbf{E} \times \mathbf{B}$ direction. Similarly, *Parks et al.* [2001] argued that the large $\langle \mathbf{v} \rangle$ observed during BBFs are due to a highly anisotropic high energy ion component, not $\mathbf{E} \times \mathbf{B}$ flows.

As is nearly always the case with experimental physics, with new and better instrumentation, new unanticipated and unexplained features are seen in the data. These new features suggest that MHD does not accurately describe the plasma sheet dynamics and that a kinetic approach is warranted.

1.7 Scope of this Dissertation

As noted earlier, the current understanding of plasma sheet behavior during auroral activity is based on observations of the bulk ion moments. These observations are limited by the fact that they only take into account the ions, assume the plasma acts as a single component fluid, and only consider changes in the dynamics on time scales much longer than the local proton gyroperiod. However, recent findings of *Chen et al.* [2000a, b] and *Parks et al.* [2001] suggest that the plasma can often be composed

of multiple components, and, therefore, MHD cannot accurately describe the plasma sheet behavior. Additionally, *Fillingim et al.* [2002] have shown that the ion plasma distributions can change dramatically on kinetic time scales. The present picture of plasma sheet dynamics during auroral activity is based on incomplete observations.

Our goal in this dissertation is to provide the most complete set of plasma sheet observations during auroral activity currently available. We go beyond previous work by emphasizing the kinetic aspects of the plasma dynamics which have largely been ignored since *Nakamura et al.* [1991]. Our primary sources of particle data are the three-dimensional distribution functions rather than moments of the distributions. In addition, we have the capability to resolve changes in the ion dynamics with a time resolution comparable to or faster than the local ion gyroperiod. Here we also pay considerable attention to the electron behavior when relating plasma sheet processes to the aurora. This makes sense since it is the electron interactions with the atmosphere which are responsible for most of the auroral emissions. For a complete picture of how the plasma sheet behaves during auroral activity, we include both ion and electron observations at the highest time resolution available.

We work toward achieving this goal by analyzing coincident plasma sheet and global auroral data. The plasma and magnetic field data were obtained by instruments onboard the WIND spacecraft when it was in the near-Earth plasma sheet ($X \sim -10$ to -20 R$_E$). During these intervals, the UltraViolet Imager (UVI) [*Torr et al.*, 1995] on the POLAR spacecraft was imaging the entire northern auroral region. We begin by analyzing the plasma sheet dynamics during an interval when UVI recorded a series of pseudobreakups. By comparing these observations with observations taken during substorm intervals, we try to determine if there is any difference in the plasma sheet dynamics during different types of auroral activity.

In Chapter 2 we briefly cover the attributes of the instrumentation used in this research. UVI, which has the capability to image the entire northern auroral region continuously for several hours with high spatial and temporal resolution, allows us to

directly compare auroral activity, morphology, and location to plasma sheet processes. In the plasma sheet, the three-dimensional plasma and energetic particle investigation (3DP) on the WIND spacecraft measures the three-dimensional particle distributions for both ions and electrons over an energy range from a few eV up to several hundred keV with unprecedented sensitivity and temporal resolution [Lin et al., 1995]. The ambient magnetic field in the plasma sheet is measured by the WIND Magnetic Field Investigation (MFI) [Lepping et al., 1995].

In Chapter 3 we present coincident auroral and plasma sheet observations from July 26, 1997. During the WIND perigee pass of July 26, 1997, UVI observed several pseudobreakup events. The position of the auroral emission mapped to the equatorial magnetosphere coincides very closely with the position of WIND. Using this favorable conjunction, we focus on this interval in order to learn about the behavior of the plasma sheet plasma during pseudobreakups.

This is an especially fortuitous interval because during several pseudobreakup events 3DP was operating in "burst mode," collecting three-dimensional ion and electron distribution functions every three seconds. This integration time is comparable to the proton gyroperiod in the plasma sheet. We are able to directly observe the ion behavior on kinetic time scales with unprecedented resolution.

Chapter 4 compares the plasma and magnetic field behavior observed during pseudobreakups with observations from other perigee passes when substorms were observed. The plasma sheet signatures of both kinds of auroral activity appear very similar. During both types of events, increases in auroral precipitation into the ionosphere are associated with large amplitude, high frequency magnetic field fluctuations, large Earthward ion $\langle v \rangle$, increases in the fluxes of high energy ions and electrons, and hardening of the electron spectrum. Both ion and electron distributions appear to be composed of multiple components. Electromagnetic waves with power at frequencies up to and above the local proton gyrofrequency area also observed. Additionally, the ion distributions can change significantly in one gyroperiod. Together, these results

imply (1) that the microphysical processes occurring in the plasma sheet during pseu-dobreakups and substorms are the same and (2) that kinetic effects are important, hence MHD cannot adequately describe the physics occurring during large ion $\langle v \rangle$ events.

Finally in Chapter 5, we summarize our observations and put them into context with previous observations and theories. Lastly, we address some of the issues which remain unresolved by this work and identify some areas in which future research may be directed.

Chapter 2

INSTRUMENTATION

2.1 POLAR/UVI

Global images of the aurora presented in this dissertation are taken by the UltraViolet Imager (UVI) [*Torr et al.*, 1995] onboard the POLAR spacecraft. POLAR was launched in early 1996 into a high inclination, highly eccentric, polar orbit. The apogee of POLAR is 8 Earth radii (R_E) above Earth's surface, and perigee is just under 1 R_E above the surface of Earth. Initially, apogee was above Earth's north pole. The instrument has an 8° field of view and is mounted on a pointable despun platform which permit simultaneous imaging of the entire auroral oval as the spacecraft rotates. These attributes allow UVI to continuously look down on the northern auroral region for a significant fraction of POLAR's 18 hour orbit.

An 8° field of view divided by about 200 pixels in each dimension yields a per pixel angular resolution of about 0.04° or 0.7 milliradians. At apogee 8 R_E above the surface, this translates into a resolution of roughly 35 km in the ionosphere at an altitude of 100 km. This is equivalent to about $\frac{1}{3}^{\circ}$ in latitude and a little less than 1° in longitude at auroral latitudes (60 to 70°) which corresponds to about 4 minutes of local time. Away from apogee, of course, the imager can detect smaller spatial scales.

Due to the unsuccessful deployment of one of the electric field booms, the POLAR spacecraft "wobbles" with a period of about 6 seconds. Since the nominal image integration time is about 37 seconds, the effect of the wobble is to smear the images by 10 pixels in the wobble direction. This greatly reduces the resolution in the wobble direction; the resolution perpendicular to the wobble direction is unaffected. Note that

the images shown in Chapter 1 have been dewobbled. Since the present dewobbling algorithm is not flux conserving, quantitative analysis must be done with uncorrected images leading to reduced spatial resolution.

UVI images the aurora in the ultraviolet region of the spectrum using four narrow band filters. The images shown in this dissertation are all taken with a filter which is sensitive to the wavelength range from 160 to 180 nanometers (nm), in the wavelength region of the Lyman-Birge-Hopfield (LBH) system of emission bands. The auroral LBH emissions are the result of excitation of molecular nitrogen (N_2) by electron impact. Since these emissions in the wavelengths passed by the filter are not significantly absorbed by the atmosphere, the intensity of the emission is nearly directly proportional to the electron energy flux into the ionosphere [*Torr et al.*, 1995; *Germany et al.*, 1998]. Therefore, we obtain a spatial image of the total electron energy flux. Multiplying by the area covered by each pixel, we are able to derive a quantitative spatial map of the electron energy deposition rate (power) into the auroral ionosphere.

For a more complete description of the UVI instrument, the reader is referred to *Torr et al.* [1995].

2.2 WIND/3DP

The main goal of the WIND spacecraft, launched in 1994, is to monitor and study the upstream solar wind. For this reason, a majority of each orbit is outside of Earth's magnetosphere. However, during perigee, WIND passes through the magnetosphere in the vicinity of the near-Earth plasma sheet at distances of about 10 to 20 R_E from Earth. During this time, the three-dimensional plasma and energetic particle investigation (3DP) [*Lin et al.*, 1995] provides high time, angular, and energy resolution measurements of the magnetospheric plasma.

The 3DP experiment is made up of three detector systems: the ion (proton)

electrostatic analyzers (PESA), the electron electrostatic analyzers (EESA), and the semi-conductor detector telescopes (SST). Together, these instruments are able to measure the full three dimensional ion and electron distributions in the energy range from a few eV to > several hundred keV (up to MeV energies for ions) in one spacecraft spin, about 3.14 seconds. Typically, the distributions that we use are averaged over several spacecraft rotations.

3DP is the ideal platform for studying plasma kinetics. Compared to currently operating and previously flown plasma instruments in the magnetosphere, 3DP has unprecedented sensitivity and temporal resolution. Table 2.1 compares some of the attributes of 3DP with those of other recent magnetospheric plasma instruments. The geometric factor of 3DP is several times greater than that of previously flown instruments. Additionally, full three-dimensional particle distributions can be obtained in one three-second spacecraft rotation – comparable in time scale to the proton gyroperiod in the near-Earth plasma sheet.

The detector systems can operate in several different modes depending upon the spacecraft location and scientific objectives. In the following subsections, we describe each of the detector systems; however, the pertinent attributes that are quoted (temporal, angular, and energy resolutions) apply only to the modes of operation when WIND is in the magnetosphere. A more detailed description of the 3DP instrumentation can be found in *Lin et al.* [1995].

2.2.1 PESA

PESA is made up of two ion electrostatic analyzers with widely different geometrical factors: PESA-L with a low geometrical factor, and PESA-H with a geometrical factor about 100 times larger. The use of dual analyzers increases the range of fluxes that can be measured without detector saturation.

Both PESA-L and PESA-H (as well as EESA-L and EESA-H to be discussed later) are symmetrical spherical section electrostatic analyzers [*Carlson et al.*, 1982]. This

Table 2.1: Attributes of some selected magnetospheric particle instruments

Spacecraft/ instrument	Energy range	Angular resolution (degrees)	Geometric factor (cm^2 sr eV/eV)	Time resolution 3-D distribution (seconds)
WIND/3DP [*Lin et al.*, 1995]				
PESA-H (i^+)	3 ev–30 keV	22.5×22.5[a]	0.015	3
EESA-H (e^-)	100 ev–30 keV	22.5×22.5[a]	0.1	3
POLAR/HYDRA [*Scudder et al.*, 1995]				
i^+	2 ev–35 keV	10×10	0.0066	6
e^-	2 ev–35 keV	10×10	0.0066	6
POLAR/TIMAS [*Shelley et al.*, 1995]				
i^+	15 ev–32 keV	11.25×11.25	0.015–0.1	3
GEOTAIL/CPI [*Frank et al.*, 1994]				
i^+	1.3 ev–48.2 keV	40×45[b]	$5.1×10^{-4}$	3 (18)[c]
e^-	1.3 ev–48.2 keV	40×45[b]	$1.3×10^{-4}$	3 (18)[c]
GEOTAIL/LEP [*Mukai et al.*, 1994]				
i^+	32 ev–39 keV	22.5×22.5	0.008	12
e^-	8 ev–38 keV	22.5×22.5	0.002	12

[a] For PESA-H and EESA-H the angular resolution is 5.6×5.6° within ±22.5° of the ecliptic plane, 11.25×11.25° to ±45°, and 22.5×22.5° beyond.

[b] Typical value. The angular resolution depends upon the instrument mode.

[c] CPI is designed to measure 3-D distributions in 3 seconds, but due to telemetry constraints, the operational time resolution is typically 18 seconds.

Table 2.1: (continued)

Spacecraft/ instrument	Energy range	Angular resolution (degrees)	Geometric factor (cm^2 sr eV/eV)	Time resolution 3-D distribution (seconds)
AMPTE IRM/plasma instrument [*Paschmann et al.*, 1985]				
i$^+$	20 ev–40 keV	22.5×22.5^d	1.6×10^{-4}	4
e$^-$	15 ev–30 keV	22.5×22.5^d	1.1×10^{-4}	4
AMPTE UKS/ion experiment [*Coates et al.*, 1985]				
i$^+$	10 ev–20 keV	22.5×22.5^e	0.0056	5
AMPTE UKS/electron experiment [*Shah et al.*, 1985]				
e$^-$	6 ev–25 keV	28×36	0.0013	5
ISEE 1, 2/FPA [*Bame et al.*, 1978]				
i$^+$	70 ev–40 keV	27.5×22.5		24
e$^-$	10 ev–20 keV	27.5×22.5		24
ISEE 1, 2/LEPEDEAS [*Frank et al.*, 1978]				
i$^+$	1 ev–45 keV	23×22.5	0.001	128
e$^-$	1 ev–45 keV	23×22.5	1.5–7×10^{-4}	128

^{d} Typical value. The angular resolution depends upon the instrument mode.

^{e} The angular resolution is 11.25 (polar angle)×22.5° (azimuthal angle) within ±22.5° of ecliptic plane.

type of instrument measures the energy per charge (E/q) of the incoming particles. Throughout the analysis, all particles are assumed to be singly charged. This is typically a good assumption in the magnetosphere and allows us to directly relate the instrument response to particle energy. Additionally, all positively charged particles are assumed to be protons, and all negatively charged particles are assumed to be electrons.

Since the main purpose of the experiment is to study the solar wind, PESA-L is operated in a mode which gives a detailed picture of the solar wind plasma without wasting telemetry. The angular resolution of PESA-L is very good (5.625° × 5.625°), but the total angular coverage is small compared to the unit sphere (28° × 28° ≈ 2% of unit sphere). In addition, since the geometrical factor is low, few particles are detected in the magnetosphere. Therefore, we do not use PESA-L data in our analysis and do not discuss its attributes further.

PESA-H has an operational field of view of 180°. As the spacecraft spins, a full 4π steradians is covered in one rotation (3.14 seconds). Typically the integration time is 8 or 16 spacecraft rotations (25 or 50 seconds) due to telemetry limitations. When the instrument is in "burst mode," three-dimensional distributions are obtained during each spin. Due to the large increase in the amount of data to be telemetered, the angular resolution during burst mode is somewhat decreased.

The angular resolution of PESA-H is non-uniform. The angular resolution is finer in the Sunward pointing direction near the equator to provide better coverage of the solar wind plasma when WIND is outside the magnetosphere. There are 120 different angular bins with varying sizes from 11.25° × 11.25° to 45° × 90° (elevation × azimuth). During burst mode, the number of angular bins is decreased to 56 because of the reduced angular resolution. Again, the angular bin size during burst mode is non-uniform; Sunward pointing bins are smaller.

For the data shown here, the PESA-H counts are binned into 15 logarithmically spaced energy channels from 70 eV to 30 keV. During burst mode intervals, the

energy coverage and the number of energy channels remains the same.

2.2.2 EESA

Similar to PESA, EESA is composed of two electrostatic analyzers with different geometric factors. The geometric factor of EESA-L is 10 times smaller than that of EESA-H.

Both instruments have operational fields of view of 180° and sweep out 4π steradians in one spacecraft spin. The fields of view of the EESA-L and EESA-H are offset by 90°. The integration time for both instruments is typically one spin (3.14 seconds). As noted later, this makes it possible to look at two dimensional electron spectra with sub-spin time resolution. However, except during burst mode intervals, EESA-L distributions are only transmitted once every 16 spacecraft rotations (25 seconds). Similarly, EESA-H distributions are transmitted once every 16 or 32 spacecraft rotations (25 or 50 seconds). During burst mode intervals, EESA-L distributions are available for each spacecraft spin, so we have continuous data. In the data presented here, there is no change in EESA-H for the burst mode of operation.

The angular resolutions of EESA-L and EESA-H are very similar to each other and are much more uniform than the angular resolution of PESA-H. Both instruments have 88 angular bins in each of the 15 logarithmically spaced energy channels. EESA-L covers energies from 7 eV to 1 keV. The lowest energy channels, less than about 100 eV, are usually contaminated by photoelectrons. The energy range of EESA-H is 100 eV to 30 keV. There is some overlap in the energy ranges of EESA-L and EESA-H. This allows for the comparison of the two instruments in the overlapping energy range.

2.2.3 SST

The SST system is composed of three arrays of two double-ended semi-conductor detector telescopes for a total of six telescopes and 12 semi-conductor detectors. One

end of each telescope is covered with a thin foil to stop ions with energies up to 400 keV; electrons pass through the foil relatively unperturbed. On the other end of each telescope, a broom magnet is mounted which sweeps away electrons with energies up to 400 keV but leaves ions unaffected. Therefore, in the absence of higher energy particles, the foil covered detectors measure only electrons while the open ended (magnet) detectors measure only ions (assumed to be protons).

Each end of each telescope has a 36° field of view. Five telescopes are arranged to cover 180°. As the spacecraft rotates, the five foil detectors (as well as the five open detectors on the other end of the telescopes) cover 4π steradians in one spin. The sixth telescope points in the same direction as one of the other five, but its geometric factor is reduced by a factor of 10 to accommodate the most intense fluxes.

Due to telemetry limitations, the integration time of the detectors is typically two to four spacecraft rotations. During burst mode, three dimensional distributions are obtained for each spin. As a result, higher energy channels can have very few, if any, counts.

There are a total of 48 angular bins for the foil detectors and 48 for the open detectors. In each case 8 bins are from the sixth, low geometric factor detectors and are redundant. Therefore, 40 bins for each set of detectors, foil and open, cover the unit sphere.

The foil detectors measure electrons in the energy range from 20 keV to about 600 keV. Protons in the energy range from 70 keV to 7 MeV are measured by the open detectors. Particles with energies above the stated energy ranges are able to penetrate through the semi-conductor detectors. Two of the double-ended telescopes have a third semi-conductor detector sandwiched between the other two detectors which are able to measure penetrating electrons up to > 1 MeV and penetrating protons up to 11 MeV. Due to limited spatial coverage and low counts, data for penetrating particles are not used.

2.3 WIND/MFI

Magnetic field data used in this dissertation are measured by the WIND Magnetic Field Investigation (MFI) [*Lepping et al.*, 1995]. MFI is a dual triaxial fluxgate magnetometer with a well tested, flight proven design. The instrument has a variable resolution depending upon the range of operation. There are 8 different ranges from ±4 nT to ±65,536 nT incremented by factors of 4. The resolution is 0.025% of the maximum field detectable in each range. In the magnetosphere, the range of MFI is typically ±16 nT or ±64 nT with a resolution of ±0.004 nT and ±0.016 nT, respectively. Magnetic field vectors are supplied by the MFI Science Team with a time resolution of 3 seconds. During interesting intervals, usually when 3DP is operating in the burst mode, the MFI Team provides us with magnetic field vectors with a time resolution of 46 milliseconds. For an in-depth discussion of MFI, see *Lepping et al.* [1995].

Chapter 3

PSEUDOBREAKUP OBSERVATIONS

This chapter examines the auroral and plasma sheet observations during the WIND perigee pass on July 26, 1997. During this interval, POLAR/UVI recorded a series of quiet-time pseudobreakups unaccompanied by a globally expanding substorm while WIND was monitoring the near-Earth plasma sheet. We focus on this event because it serves as a "typical" example of the plasma dynamics seen on the plasma sheet during auroral activity. It exemplifies many of the features observed during the numerous WIND perigee passes through the near-Earth plasma sheet. First, an overview of five hours of data from 03:00 to 08:00 UT is presented and the important main features are highlighted.

Next, to get a better understanding of the processes involved, we take a detailed look at one hour of data. We go beyond the extent of previous work by not just considering the bulk plasma moments. We also consider the energy and pitch angle spectrograms for ions and electrons, respectively, and examine in detail the particle distribution functions. We also investigate the relative timing between auroral brightenings and the plasma and magnetic field changes in the plasma sheet. Additionally, by mapping the region of intense auroral emission out to the equatorial magnetosphere, we can estimate the size of the disturbed region in the plasma sheet.

Lastly, we examine the plasma behavior on kinetic time scales using high resolution (46-millisecond) magnetic field data and three-second resolution plasma data, which is comparable to the proton gyroperiod in the plasma sheet. We also stress the importance of high time resolution data by showing how the structure in the data is smeared out by time averaging, and how this changes the subsequent interpretation

of the plasma dynamics.

3.1 Overview

3.1.1 Auroral Observations

Figure 3.1 shows a sequence of UVI images taken on July 26, 1997, as POLAR was passing through apogee. The integration time of each image is nearly 37 seconds, and the time between images is about 3 minutes. The images have been transformed into magnetic apex coordinates [Richmond, 1995]. Local noon is at the top and midnight is at the bottom. It is clear that the auroral intensity caused by electron precipitation is confined to a few degrees in latitude and a few hours in local time. Additionally, the period of intense emission lasts for only about 10 minutes. Due to the short duration and localization of the auroral emission, this event is classified as a pseudobreakup.

The POLAR spacecraft wobble is mostly in the noon-midnight direction at this time. Because of this, the latitudinal extent of the aurora is exaggerated by $1.5°$ (5 pixels) or 180 km at both the equatorward and poleward edges. The longitudinal extent is accurate to about 35 km or one degree in longitude at these latitudes.

The position of the WIND spacecraft magnetically mapped down to auroral altitudes using the model of Tsyganenko [1989] for a quiet magnetosphere ($K_p = 1$) is shown on each UVI image. One can see that WIND maps to the region of intense auroral emission.

Figure 3.2 gives an overview of the auroral activity covering a 5 hour period, from 03:00 to 08:00 UT, on July 26, 1997. The top panel shows a "keogram" constructed from UVI images. It shows the latitudinal profile of the auroral activity over a range of local times as a function of time. The energy deposition rate due to electron precipitation, which is proportional to the auroral intensity as mentioned in Chapter 2, was binned into $\frac{1}{2}°$ magnetic latitude by $\frac{1}{4}$ hour magnetic local time bins. These were then summed over local times from 21 to 03 MLT to produce the top plot. The
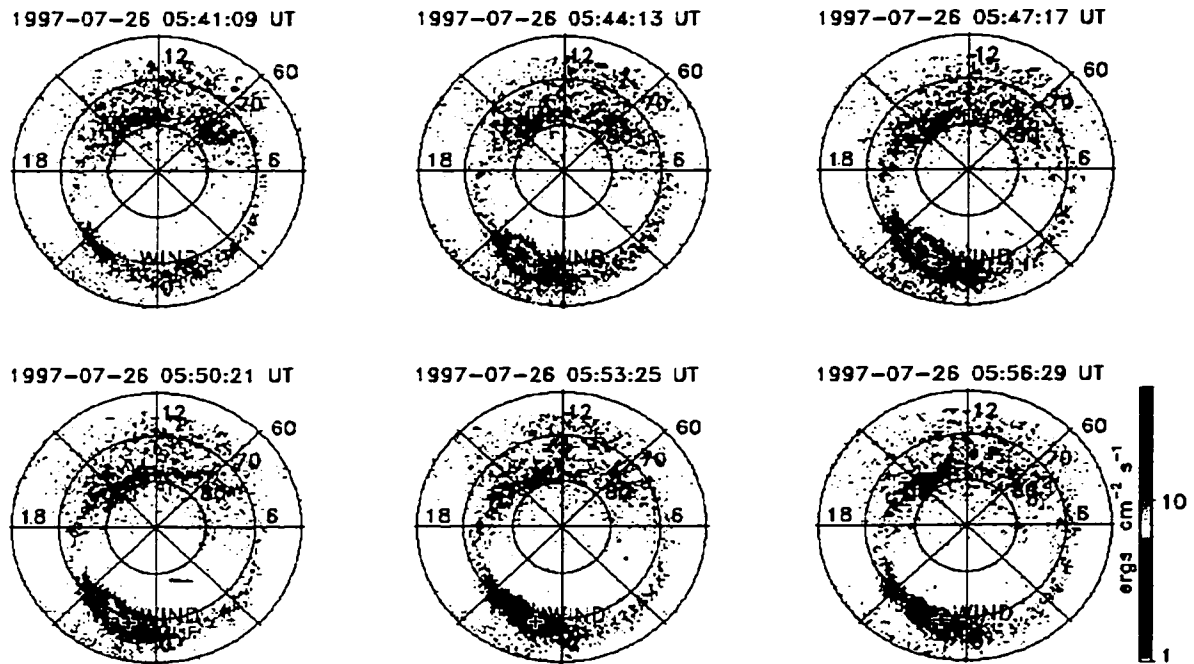
Figure 3.1: A sequence of UVI images from July 26, 1997, showing a pseudobreakup. The magnetic footprint of WIND is also shown.

line just below 70° latitude shows the latitudinal position of the footprint of WIND throughout this period.

The second plot, showing auroral activity as a function of local time and UT, was produced by summing the binned data over magnetic latitudes from 60 to 90°. Local times from dawn toward midnight are on the bottom half of the plot, and local times from midnight toward dusk are on the top half of the plot. Note that only local times from the nightside hemisphere, 18 MLT to 6 MLT, are included in this plot, since we are concerned with auroral activity that maps to the nightside plasma sheet. The magnetic local time position of the WIND footprint throughout this interval is shown by the black line. At the beginning of this interval at 03 UT, the footprint of WIND
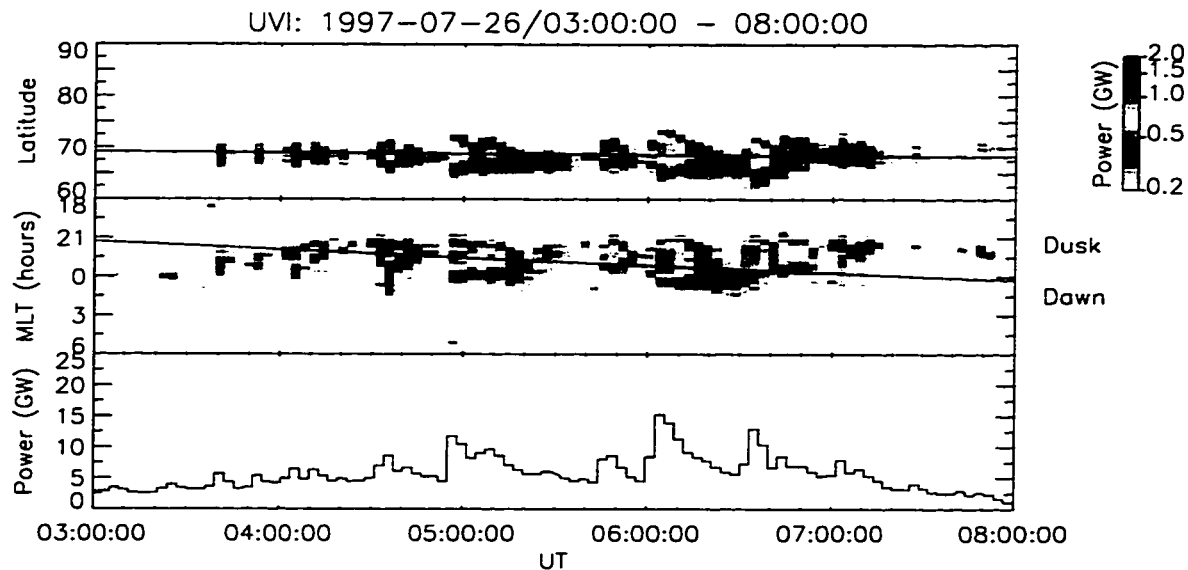
Figure 3.2: Overview of auroral imagery data. From top to bottom: "keogram," auroral intensity as a function of latitude and Universal Time; auroral intensity as a function of magnetic local time and Universal Time; energy deposition rate (power) from precipitating electrons.

is near 21 MLT. At the end of this interval at 08 UT, the footprint is just past local midnight.

The bottom panel of Figure 3.2 shows the energy deposition rate due to precipitating electrons into the entire nightside quadrant of the ionosphere. The binned energy deposition rate data is summed over local times from 21 to 03 MLT and over latitudes from 60 to 90°. Summing of this area includes all of the active aurora during this interval. As expected, as the aurora becomes more intense and expands in latitude and longitude, the energy deposition rate increases.

Starting shortly before 07 UT, it appears as though the equatorward edge of the auroral emission moves poleward. At the same time, the auroral emission appears to be increasingly confined to the dusk sector. Neither of these effects are physical, but

are the result of the auroral oval moving out of the UVI field of view. Therefore the latitudinal position, local time position, and energy deposition rate after 06:45 UT is not accurate. However, it is clear that limited auroral activity is continuing.

Each of the auroral brightenings is small, only a few degrees in latitude and a few hours in local time, and short-lived, a few minutes to a few tens of minutes for the largest events. Additionally, the energy deposition rate into the nightside ionosphere is low, just over 15 GigaWatts (GW) for the strongest event. UVI routinely observes substorms which have energy deposition rates of nearly 100 GW. Therefore, these auroral brightenings are interpreted as pseudobreakups. It should be noted that since these are subjective criteria, others may argue that these are actually small substorms. However, there is a lack of accepted, quantitative criteria to distinguish between pseudobreakups and substorms [*Rostoker*, 1998; *Aikio et al.*, 1999]. Later it will be argued that there is no difference in the magnetospheric dynamics during pseudobreakups and substorms, so the distinction will become a moot point.

3.1.2 Plasma Sheet Magnetic Field Observations

On July 26, 1997, the WIND spacecraft was making a perigee pass through Earth's magnetosphere. Figure 3.3 shows the orbit of WIND. The left hand plot shows the projection of the orbit in the X-Y plane in the geocentric solar ecliptic (GSE) coordinate system (looking from the north toward the south), where the X-axis points from toward the Sun and the Y-axis points toward dusk. Also shown in this figure is the average location of Earth's bow shock and magnetopause. The heavy black line emphasizes the position of WIND during the five hour interval between 03 and 08 UT.

The middle plot shows the projection of the orbit in the GSE Y-Z plane (looking from the Sun toward Earth), where the Z-axis is northward and perpendicular to the ecliptic plane. Since structures within Earth's magnetosphere are often constrained by the internal magnetic field rather than the solar wind, the gray curve represents the
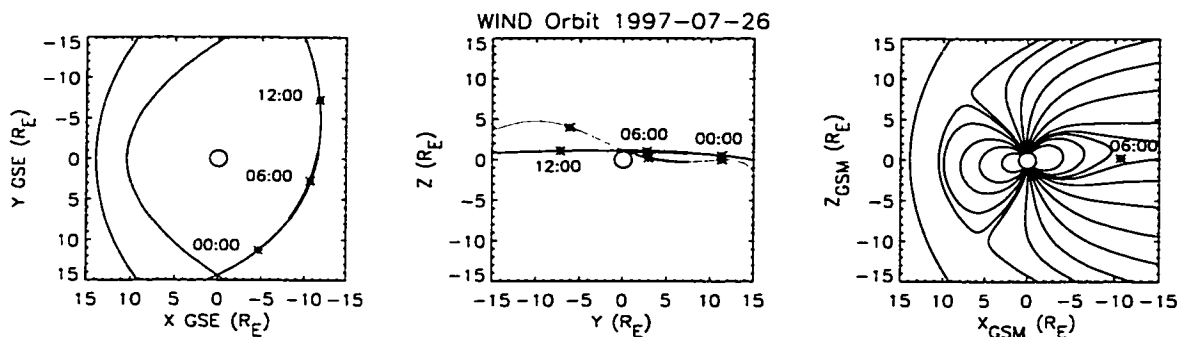
Figure 3.3: Orbit of the WIND spacecraft on July 26, 1997. From left to right: position in the X-Y plane; position in the Y-Z plane; position in the X-Z plane at 06:00 UT.

projection of the WIND orbit in the Y-Z plane in the geocentric solar magnetospheric (GSM) coordinate system. The only difference between the GSE and GSM coordinate systems is a rotation about the X-axis in the direction of Earth's magnetic pole. Since Earth rotates once per day, the GSM Y-Z plane oscillates with respect to the GSE Y-Z plane once per day.

Finally, on the right hand side of Figure 3.3, is the position of WIND in the GSM X-Z plane at 06:00 UT. Also plotted are several lines of magnetic force calculated using the model of *Tsyganenko* [1989] showing the configuration of Earth's magnetic field at this time. Together these plots show that WIND was very deep in the magnetosphere and near the equatorial plane throughout this interval.

Figure 3.4 compares the UVI auroral data with the magnetic field recorded by MFI in the plasma sheet. The first two panels are identical to the top and bottom panels of Figure 3.2. The third panel shows the GSM components of the magnetic field along with the magnitude of the magnetic field (uppermost black curve) at three second time resolution. The next panels displays the azimuth and the elevation angle of the magnetic field in GSM coordinates. The black dotted lines show where the azimuth (elevation) angle equals 90° and 270° (±45°). The red line indicates

Figure 3.4: Comparison of auroral imagery data with plasma sheet magnetic field data. From top to bottom: keogram; energy deposition rate; magnetic field in GSM coordinates; azimuth (black) and elevation (red) angle of the magnetic field; time derivative of the magnetic field; root-mean-square (rms) deviation of the magnetic field.

where the elevation angle equals zero and where the azimuth angle equals 180°. The fifth plot shows the time derivative of the magnitude of the magnetic field with three-second time resolution. The root-mean-square (rms) deviation of the magnitude of the magnetic field within each three-second data point is shown in the bottom plot.

Throughout most of this interval, the dominant component of the magnetic field is the X-component. The X-component is negative indicating that WIND is in the southern hemisphere below the current sheet in agreement with the modeled magnetic field in the previous figure. It is clear from this figure that during times of auroral activity, the magnetic field in the plasma sheet can be rapidly changing. Large amplitude, high frequency fluctuations in all three components of the magnetic field occur during periods of intense auroral emission. The magnetic field signatures are not simple dipolarizations (step-wise increases in the Z-component). The Z-component increases and the magnitude of the X-component decreases, but it appears as though high frequency fluctuations are superposed on dipolarization trends. Close inspection shows that the amplitudes of the fluctuations can be as large and larger than the ambient magnetic field magnitude. This indicates that the responsible processes involve may nonlinear effects.

The dipolarization trends are also apparent in the elevation angle curve. After 05 UT, the elevation angle begins to steadily decrease. Some fluctuations are apparent at 05:30 UT, which interrupt the elevation angle decrease. The elevation angle then resumes its decrease and continues to decrease until 05:45 UT at which point it increases in conjunction with large fluctuations in all three components of **B** and a brightening of the aurora. The elevation angle increases even further again accompanied by large fluctuations in **B** and a sudden brightening of the aurora near 06 UT. Once the magnetic fluctuations stop, elevation angle steeply decreases until 06:30 UT. Then the elevation angle tends to increase amid large fluctuations throughout the duration of the auroral brightening. The behavior of the plasma sheet magnetic field elevation angle undergoing a steady decrease punctuated by a dipolarization, is similar

to that observed during substorms [*Cummings et al.*, 1968] and implies a restructuring of the plasma sheet currents on rapid time scales [*Kaufmann*, 1987].

The fifth plot, which shows $\partial|\mathbf{B}|/\partial t$, gives a quantitative measure of the magnetic field fluctuations. Since $\partial\mathbf{B}/\partial t = -\nabla \times \mathbf{E}$, this quantity is also related to the induced electric field present in the plasma sheet. Typical values of ~ 5 nT/s yield induced electric fields of a few mV/m at length scales comparable to the thermal proton gyroradius. The rms deviation of the magnitude of $\mathbf{B}$ within each three-second data point, shown in the bottom plot, gives an indication that $\partial|\mathbf{B}|/\partial t$ can be much larger than what is shown here. There can be considerable variation within a three-second sample, especially when the magnetic field is strongly fluctuating. This suggests that there are variations present in the magnetic field on time scales shorter than 3 seconds.

3.1.3 Ion Observations

Figure 3.5 compares the plasma data taken by 3DP in the plasma sheet with the magnetic field data and auroral data presented earlier. The first two panels of Figure 3.5 again show the keogram and energy deposition rate derived from UVI images. The third panel contains the three-second resolution magnetic field data in GSM coordinates. The next three panels show the first three moments calculated from the PESA-H ion distribution functions: density, velocity, and temperature. The three components of velocity and temperature are shown in GSM coordinates. In this case the distribution functions were measured for ions with energies from 70 eV to 30 keV with a resolution of either 25 or 50 seconds depending upon the PESA-H instrument mode.

There are several interesting features to notice in this figure. Again, note that rapid, large amplitude fluctuations in all three components of the magnetic field occur at the onset of the auroral brightenings. Sharp decreases in the ion density can occur during the magnetic field fluctuations and auroral intensifications, most notably in the intense events occurring after 04:50 UT. The density recovers between
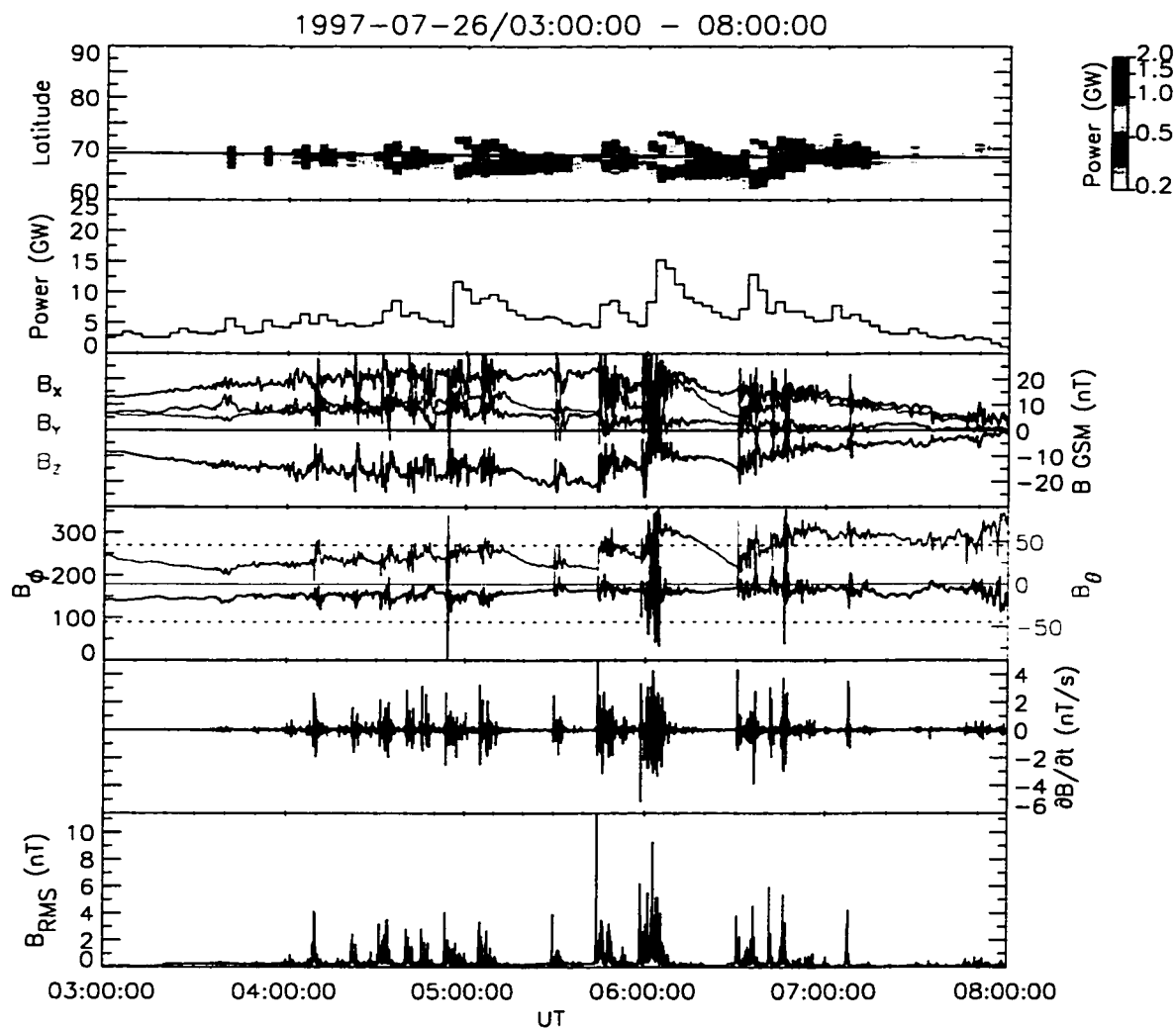
Figure 3.5: Comparison of auroral imagery data with plasma sheet magnetic field data and ion moments. From top to bottom: keogram; energy deposition rate; magnetic field in GSM coordinates; ion density; ion velocity in GSM coordinates, ion temperature in GSM coordinates.

the decreases when **B** is steady and the aurora is fading.

Also, increases in the ion velocity moment, $\langle \mathbf{v} \rangle$, particularly the X-component, correspond very well to fluctuations in the magnetic field, and, as a result, auroral brightenings. Large $\langle \mathbf{v} \rangle$ coincide with the onset of auroral brightenings, but the magnitude of $\langle \mathbf{v} \rangle$ is not correlated with the intensity of the aurora. Similarly, the magnitude of $\langle \mathbf{v} \rangle$ is not correlated with the intensity of the fluctuations in the magnetic field. However, every magnetic field fluctuation is accompanied by an increase in $\langle \mathbf{v} \rangle$, usually in the positive X- (Earthward) direction. There is sometimes a significant component of $\langle \mathbf{v} \rangle$ in the negative X-direction (near 04:55 UT) or in the positive or negative Y-direction. While a one-to-one correspondence is not present, the density generally decreases during large $\langle \mathbf{v} \rangle$; this is especially apparent after 04:50 UT.

The behavior of the ion temperature is a little more complicated. After 04:50 UT increases in the ion temperature are also associated with auroral brightenings, fluctuations in the magnetic field, decreases in density, and increases in $\langle \mathbf{v} \rangle$. During the two high $\langle \mathbf{v} \rangle$ events immediately before this time (just after 04:30 and 04:40 UT), the temperature decreases slightly. Between 05:10 and the temperature increase at 05:45 UT (except for a brief increase at 05:30 UT), the ion temperature is decreasing. During the same interval, $|\mathbf{B}|$, $|B_X|$, and density are all increasing and steadily approaching their local maximum values. This may suggest that the distance between the WIND spacecraft and the current sheet was temporarily increased. A similar effect is noticed just before 06:30 UT as well. At the 05:45 UT auroral brightening (and again at 06:30 UT), large fluctuations in the magnetic field are observed, B_Z increases as $|B_X|$ decreases, the density decreases, large Earthward ion $\langle \mathbf{v} \rangle$ are present, and the temperature increases. The density and temperature appear somewhat anti-correlated throughout this interval. However, since the density decreases are larger than the temperature increases, the plasma pressure ($P = nkT$) is not constant. In general during this period, the plasma pressure decreases during times of plasma sheet activity.

Next we go beyond looking at only moments. In Figure 3.6 we again show the auroral keogram and the plasma sheet magnetic field and ion $\langle v \rangle$ in GSM coordinates for comparison. In addition, the fourth panel shows the ion omnidirectional flux (in units of $(cm^2 \cdot s \cdot eV \cdot ster)^{-1}$) at selected energies from 3 keV up to 1 MeV. The curves at 100 keV, 300 keV, and 1 MeV have been multiplied by factors of 100, 1000, and 3000, respectively, for clarity. The bottom four panels show the Earthward (fifth and sixth panels) and tailward (bottom two panels) energy spectrograms from $\sim$ 70 eV to $>$ 1 MeV. The Earthward (tailward) energy spectrograms were made by averaging the fluxes within 45° of the Sun-Earth line in the Earthward (tailward) direction.

Increases in the fluxes of high energy ions from about 30 keV to several hundred keV appear to correlate well with the large ion $\langle v \rangle$, magnetic field fluctuations, and subsequently, with auroral brightenings. For the most intense events, ion flux modulations are seen at energies up to 1 MeV. At energies about 10 keV and below, a different behavior is seen. Fluxes of ions below about 10 keV typically decrease when fluxes of more energetic ions are increasing.

The energy spectrograms give us directional information. During periods of large $\langle v \rangle$, the flux of energetic ions from a few 10s of keV to several hundred keV (and to 1 MeV in a few cases) increases in the Earthward direction (fifth panel). A similar effect is seen at high energies in the tailward direction (seventh panel), but the increase in flux in the tailward direction is not as large as the flux increase in the Earthward direction. While the high energy ion flux increases in both directions, there is an anisotropy present between the two directions with higher fluxes in the Earthward direction.

Similar anisotropies are seen at energies below about 10 keV, but their character is different (panels six and eight). In some cases, the fluxes decrease in both directions with larger decreases occurring in the tailward direction, as seen at 05:45, 06:00, and 06:30 UT. In other cases, the flux of ions below 10 keV increases in the Earthward direction, while the flux decreases in the tailward direction, as seen during the
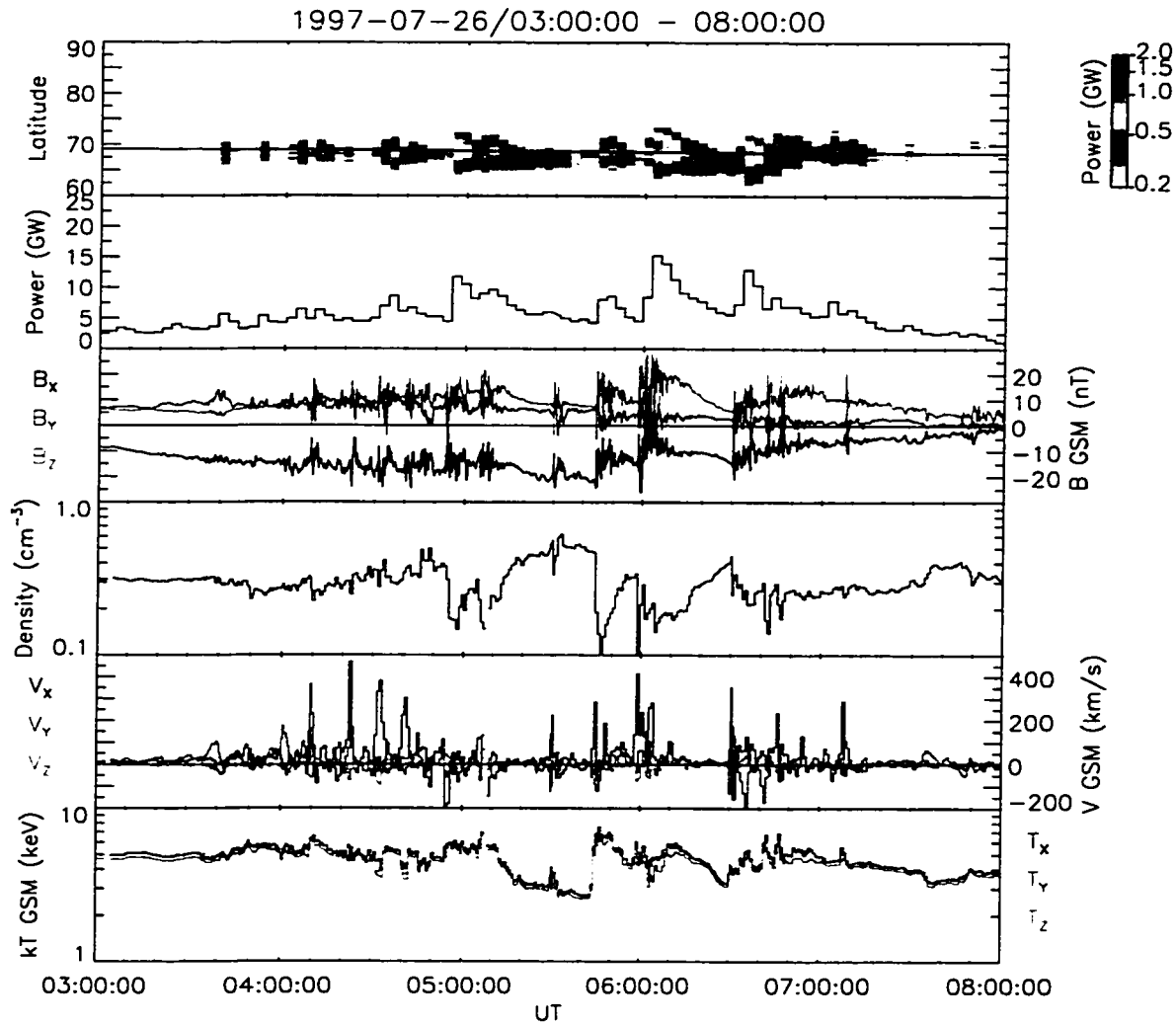
Figure 3.6: Comparison of auroral imagery data with plasma sheet magnetic field and ion data. From top to bottom: keogram; magnetic field; ion velocity; ion omnidirectional flux; ion energy spectrograms.

four large $\langle v \rangle$ in the Earthward direction between 04:00 and 05:00 UT. Just before 05:00 UT, the situation is reversed; the flux in the tailward direction increases while the flux in the Earthward direction decreases, resulting in a tailward $\langle v \rangle$. At lower energies, less than 1 keV or so, the fluxes in the Earthward and tailward directions are usually equal; that is, the distribution is isotropic at low energies.

In all cases during large $\langle v \rangle$, the fluxes of ions at high energies (> 10 keV) increase in both directions, with the Earthward flux increasing more than the tailward flux during Earthward directed $\langle v \rangle$. Below this energy, the ion flux in the tailward direction decreases during Earthward $\langle v \rangle$, while the Earthward flux can either increase or decrease. If the Earthward flux does decrease, it does not decrease as much as the tailward flux. It is the large anisotropy in the ion fluxes that gives rise to the large $\langle v \rangle$.

3.1.4 Electron Observations

We now turn our attention to the electron behavior. Figure 3.7 compares the auroral activity and plasma sheet magnetic field with the plasma sheet electron temperature perpendicular and parallel to the ambient magnetic field, the omnidirectional electron flux from 1 keV to several hundred keV, and the electron pitch angle spectrograms at selected energies from 1 keV to 100 keV. The omnidirectional flux curves for the 100 and 300 keV electrons have been multiplies by 10 and 50, respectively, for clarity. The electron temperature was calculated from the three-dimensional electron distribution functions measured from 100 eV to 30 keV and integrated over 3 seconds.

First, notice that the electron temperature and the electron flux at high energies ($\sim$ 10 keV) increase during the most intense auroral brightenings and magnetic field fluctuations at 04:55, 05:45, 06:00, and 06:30 UT. At the same time, the flux of lower energy electrons, with energies below about 1 keV, decreases. This simultaneous increase in high energy flux and decrease in lower energy flux leads to a hardening of the electron spectrum. The pitch angle spectrograms also clearly show this effect.
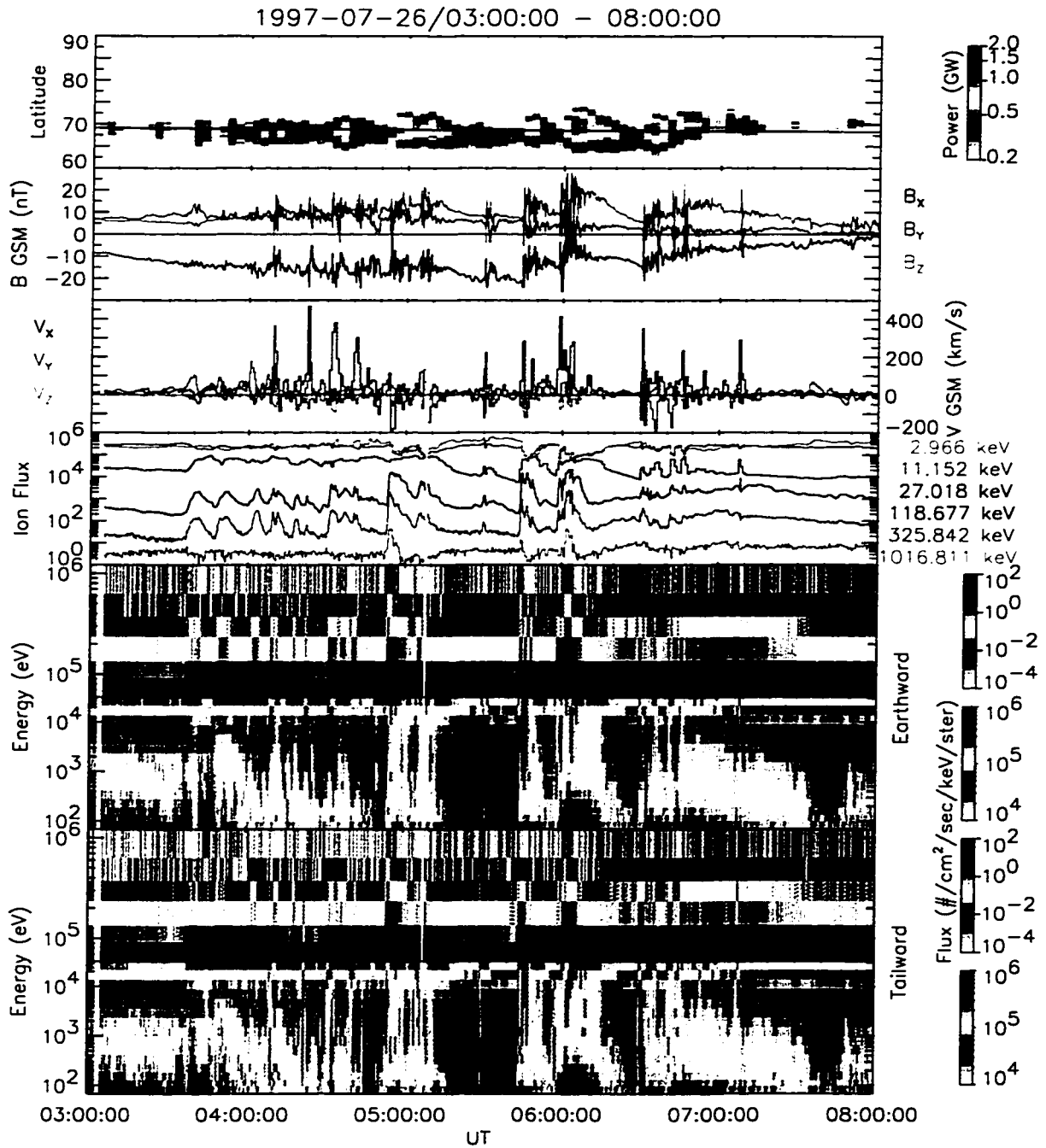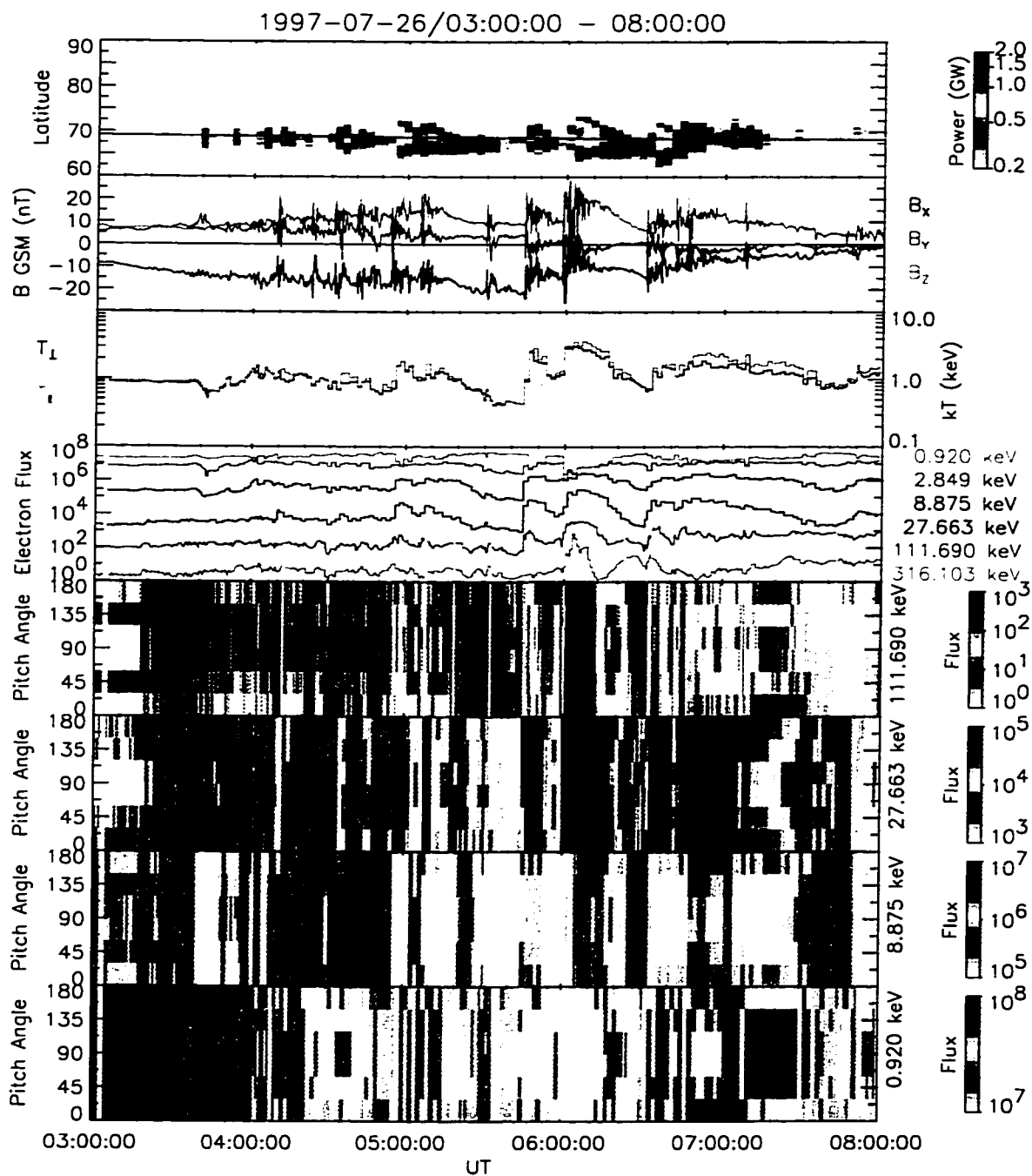
Figure 3.7: Comparison of auroral imagery data with plasma sheet magnetic field and electron data. From top to bottom: keogram; magnetic field; electron temperature; electron omnidirectional flux; electron pitch angle spectrograms.

Comparing the bottom spectrogram ($\sim$ 1 keV) with the other three spectrograms, we see that when the higher energy fluxes increase, the low energy flux decreases. Also, when the low energy flux increases, the higher energy fluxes generally decrease, though this process usually happens more gradually.

The electron temperature plot shows that after large temperature increases the parallel electron temperature is slightly higher than the perpendicular electron temperature. This is also clearly seen in the pitch angle spectrogram plots. Several minutes after the temperature and energetic electron flux increases at 06:30 UT, the pitch angle distributions at all energies from 1 keV to 100 keV are field aligned.

Throughout this interval, the electron distributions at energies above about 10 keV (top two pitch angle spectrograms) are usually peaked in the field aligned and anti-field aligned directions. Exceptions occur when the fluxes are rapidly increasing; in these cases, the distributions are mostly isotropic. At the beginning of the interval, the pitch angle distributions at energies less than 10 keV (the bottom two panels of Figure 3.7) are either isotropic or peaked slightly in the perpendicular direction near 90°. After about 04:00 UT, the distributions become peaked in the field aligned and anti-field aligned directions. This suggests that the magnetic fluctuations may play a role in creating field aligned distributions at lower energies ($<$ 10 keV), as was proposed by *Hada et al.* [1981]. Again, when rapid changes in the flux are occurring, the distributions appear isotropic at all energies.

The difference in the behavior of the electrons at high and low energies suggests that there are at least two populations of electrons present: a high energy population above about 10 keV and a lower energy component below a few keV, similar to the ions. The fluxes of these two components appear anti-correlated. Again, whether these two components are separated by a spatial boundary or a time varying energization process is unknown.

3.1.5 Size of Active Auroral Region in the Ionosphere and Magnetosphere

We can derive and estimate of the size of the disturbed region in the plasma sheet by mapping the area of intense electron precipitation in the ionosphere out to the equatorial magnetosphere. The present dewobbling routine is not flux conserving, so quantitative analysis of the auroral energetics cannot use dewobbled images in their present form. However, dewobbled images are used here to give a more accurate representation of the size and shape of the region of intense emission.

Most of the smaller auroras observed during this interval on July 26, 1997, have similar sizes, morphologies, and positions. The top image of Figure 3.8 shows the dewobbled UVI image at 05:59:33 UT in magnetic coordinates. This image looks very similar to the images at 03:39:06, 03:51:22, 04:03:38, 04:09:46, 04:55:09, 05:44:13 and 06:30:13 UT. Even though the size, shape, and position of the aurora in all of these images are similar, the maximum intensity (energy flux) varies from event to event. The bottom plot in Figure 3.8 shows the approximate region in the plasma sheet that the aurora maps to (looking down on the nightside plasma sheet from high above the north pole). The nightside of Earth is shown at the top of the plot. Also the position of WIND at 06:00 UT is shown.

At 05:59:33, the aurora is confined to a relatively narrow band only a few degrees wide in latitude located just near 70° magnetic latitude. In local time, it extends from about 21 MLT toward midnight, less than 3 hours in width. An arbitrary energy flux threshold of 3.5 ergs/cm^2/s was used to delineate the region of intense emission. (The limit of the UVI sensitivity is about 1 erg/cm^2/s.) Emissions above this threshold covered an area of 240,000 km^2 in the ionosphere, about 0.006 R_E^2.

The centroid of the aurora maps to about 13 R_E ([$-11.5, 6.3, 1$] R_E in GSM). A simple magnetic flux scaling suggests that the area should increase by a factor of 10,000 as the magnetic field decreases from 56,000 nT (at auroral altitudes) to about 6 nT near the current sheet at this position. A slightly more rigorous method,
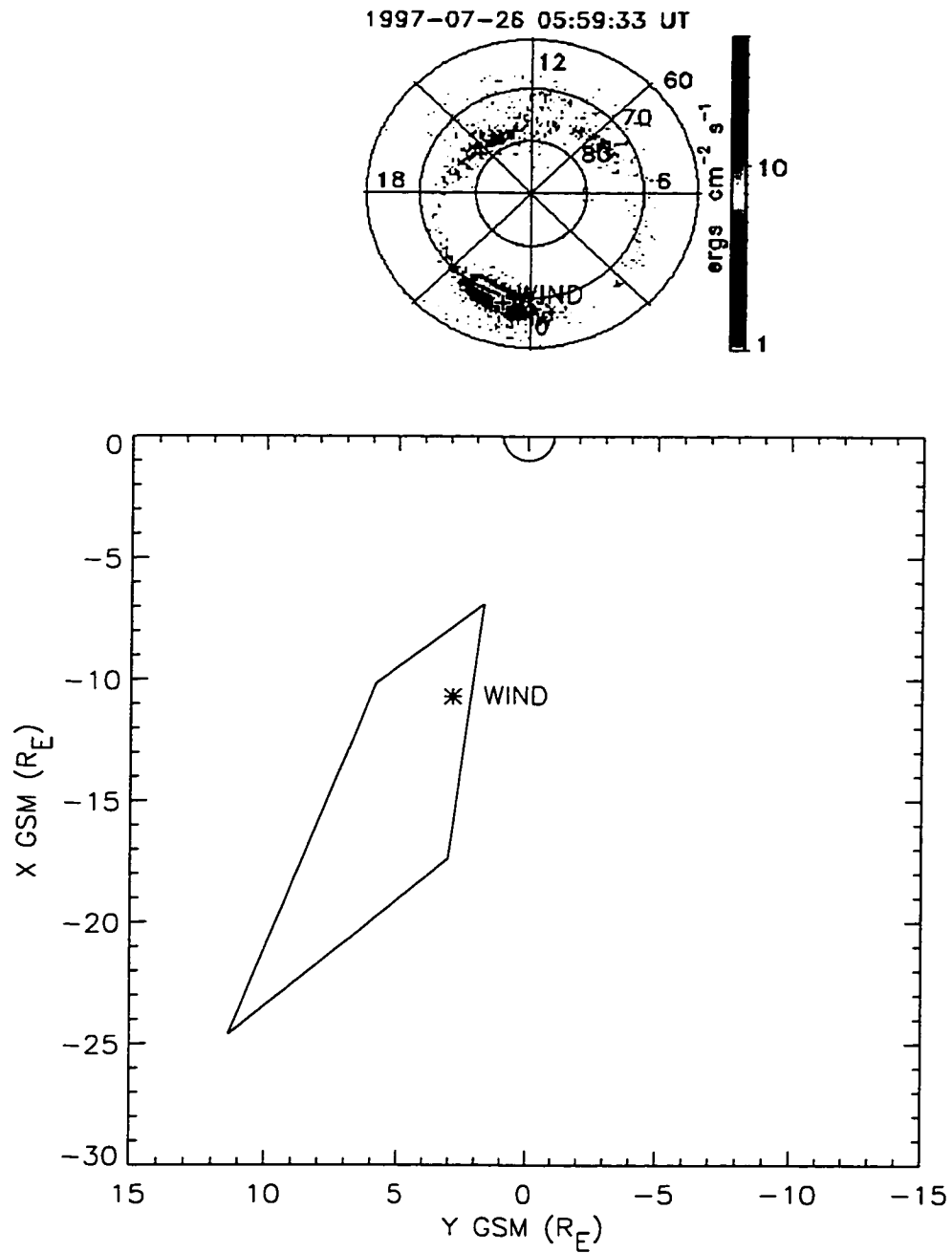
Figure 3.8: The region of intense auroral emission mapped the the equatorial magnetosphere. Top: area of emission in the ionosphere. Bottom: projection of area mapped to the equatorial magnetosphere.

approximating the aurora as a quadrilateral, mapping the four corners to the plasma sheet, and calculating the area of the mapped quadrilateral, yields an area in the plasma sheet of about 60 R_E^2, covering a total of about about 20 R_E in the X-direction and a maximum of about 5 R_E in the Y-direction. WIND is located within this region near the upper right corner at a position of $[-11, 3, 0]$ R_E.

At 06:02:37, three minutes after this image, the aurora expands to cover about 700,000 km^2 in the ionosphere, about 0.02 R_E^2. This is the largest area covered by intense emission throughout this five hour interval. A simple magnetic flux scaling suggests that the region of intense emission should now cover an area of about 200 R_E^2. As the aurora spreads poleward, the area that the aurora maps to in the plasma sheet increases very quickly in the X-direction since the field lines are stretched and tail-like. This suggests that the region of disturbed plasma in the plasma sheet can cover a large area in the equatorial magnetosphere and that this region can be quite extended in the X-direction.

The initial brightening of the aurora was noted to have occurred sometime between 05:58:20 and 05:59:33 UT. By 06:00:10 UT, the end of the integration time of the image shown here, the disturbed region in the plasma sheet is estimated to be 60 R_E^2, with an extent in the X-direction of $\sim$ 20 R_E. For a disturbance to propagate through the plasma sheet 20 R_E in 120 seconds, it must travel an average of 1000 km/s. We note that this speed is approximately equal to the local Alfvén velocity in the plasma sheet. Also, no large $\langle v \rangle$ of this magnitude have been observed in this data set.

Finally, these sizes should be regarded only as estimates. It is relatively straight forward to map things from the plasma sheet to the ionosphere, from a region of low magnetic field strength to a region of high magnetic field strength. It is much more uncertain to map features from the ionosphere to the plasma sheet. A small uncertainty in position in the ionosphere can result in a large uncertainty in position in the equatorial magnetosphere.

3.1.6 Estimate of Potential Drop Between the Plasma Sheet and Ionosphere

During auroral activity, the electron energy flux into the ionosphere increases, producing intense auroral emissions. At the same time, we note that the temperature and flux of high energy electrons in the plasma sheet increases, increasing the electron energy flux measured in the plasma sheet. We can thus make a quantitative comparison of the measured electron energy flux in the plasma sheet to the electron energy flux into the ionosphere due to precipitating electrons derived from UVI images. If the two measurements are in good agreement, then the ambient plasma sheet electrons can provide the energy flux necessary to power the aurora. If there is more energy flux entering the ionosphere than seen in the plasma sheet, then energy flux must be entering the loss cone, presumably through the presence of a parallel potential drop. If there is more energy flux in the plasma sheet than seen precipitating into the ionosphere, then the plasma sheet energy flux must be prevented from reaching ionospheric altitudes.

Figure 3.9 makes just such a comparison for July 26, 1997. The top panel shows the keogram with the WIND footprint marked, as shown before. The second panel shows electron energy flux into the ionosphere derived from UVI measurements (top curve) and the electron energy flux measured in the plasma sheet mapped to ionospheric altitudes (bottom curve). The bottom panel shows the estimated parallel potential drop between the plasma sheet and ionosphere necessary to bring the two measurements into agreement.

The ionospheric energy flux curve was created by computing the energy flux "near" the WIND footprint. Since the magnetic field model is not perfect, we don't know exactly where WIND maps to in the ionosphere. Therefore, we draw a box $10°$ in latitude (~ 1000 km) and 2 hours in local time (~ 1000 km at $70°$ latitude) centered on the projected footprint. We use the maximum and minimum values of the energy flux within this box as the upper and lower limits of the ionospheric energy flux. Due
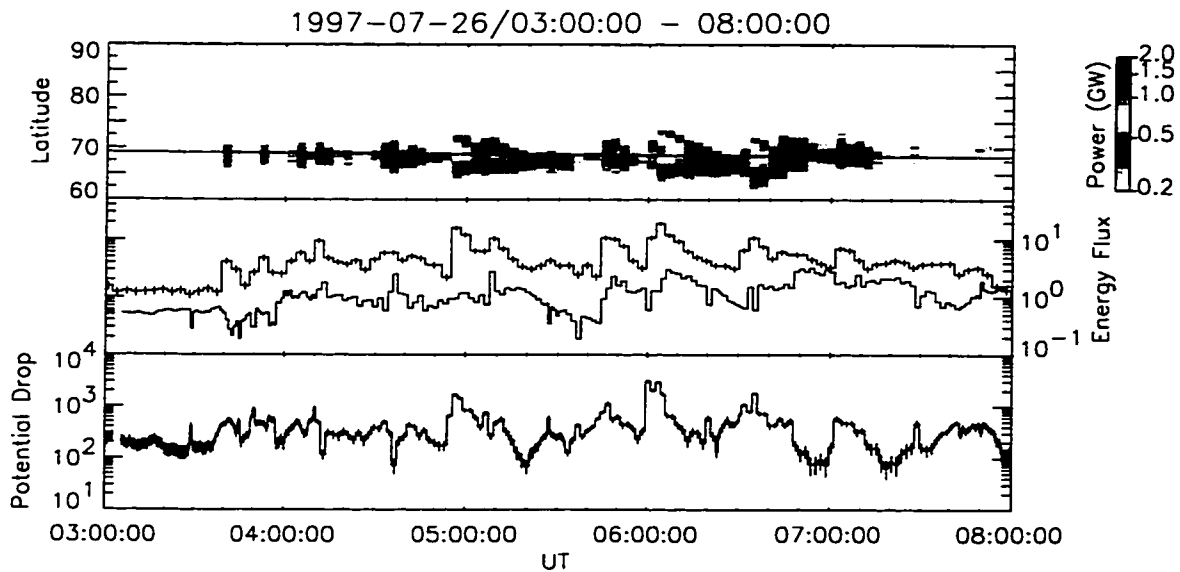
Figure 3.9: Estimate of the potential drop between the plasma sheet and ionosphere. From top to bottom: keogram; auroral and plasma sheet electron energy flux; total potential drop.

to the spacecraft wobble, the peak energy fluxes in the aurora can be diminished by up to a factor of three. In this case, the UVI energy flux may be regarded as a lower bound.

The plasma sheet energy flux was calculated by integrating the differential energy flux measured by 3DP over energy and mapping the fraction of the energy flux in the loss cone down to auroral altitudes. Since the loss cone in the plasma sheet at this distance ($<$ 1°) is much smaller than the angular resolution of the detector, we assume that the energy flux in the field aligned detector bin is evenly distributed over that bin. In reality, there should be a loss cone present with diminished energy flux in the field aligned direction, but this loss cone cannot be resolved by the detector. In this case, the 3DP energy flux can be regarded as an upper limit.

As expected, whenever the intensity increases, the energy flux into the ionosphere

increases. Throughout this interval, WIND maps "close" to the region of the most intense auroral emission. There is a significant small amplitude structure in the plasma sheet energy flux curve. During the brightest aurora, the plasma sheet electron energy flux increases. These energy flux increases occur at the same times as the electron temperature and high energy electron flux increases. Therefore, processes in the plasma sheet associated with auroral activity increase the electron energy flux incident on the ionosphere. However, even though the UVI energy flux is a lower limit and the 3DP energy flux is an upper limit, the ionospheric electron energy flux is always greater than the plasma sheet electron energy flux. During intervals of active aurora, the difference is even greater, up to an order of magnitude. This suggests that additional processes are adding energy flux to the loss cone. This is consistent with a field aligned potential above the active aurora.

Using the ratio of the ionospheric and plasma sheet energy fluxes, we can estimate the magnitude of the potential drop that would be necessary to bring the energy fluxes into agreement. As shown in the bottom plot, there is a considerable amount of structure in the estimated potential, but again we see significant increases in the potential during auroral brightenings. The values of the estimated potential drop are of about the same order of magnitude as that determined from low altitude space-craft particle measurements. The potential drop decreases as the aurora fades and is generally small during quiet intervals with little auroral activity. Given that the UVI-derived electron energy flux may be treated as a lower limit and that the measured plasma sheet electron energy flux may be considered an upper limit, the estimation of the potential drop should be considered a lower limit.

This technique shows that when the global auroral distribution is being imaged and when a spacecraft in the plasma sheet maps to the auroral region, the value of the total potential drop between the plasma sheet and the ionosphere can be remotely monitored for several hours. This technique is very dependent upon spacecraft location and also upon the magnetic field model used to map the spacecraft to ionospheric

altitudes. Additionally, due to the numerous assumptions inherent in this method, the results should be regarded as crude estimates only.

3.1.7 Summary of Observations

In summary, we find a good correlation between small scale auroral brightenings in the ionosphere and high frequency, large amplitude magnetic fluctuations in the plasma sheet when the footprint of the WIND spacecraft in the ionosphere is in close proximity to the auroral brightening. There is an increase in the ion $\langle v \rangle$ during every magnetic fluctuation often, but not always, in the Earthward direction. The large $\langle v \rangle$ are typically associated with decreases in the ion density and increases in the ion temperature. All of the large $\langle v \rangle$ are also associated with increases in the energetic ion flux with energies from several tens of keV to several hundred keV and sometimes up to 1 MeV. The energetic ion flux increases in all directions simultaneously, but the fluxes are anisotropic. At the same time, the ion fluxes at lower energies down to about 1 keV usually decrease and are likewise anisotropic. Below 1 keV or so, the ion flux is isotropic. It is, in fact, the anisotropic fluxes at the high energy range of PESA-H from 10 to 30 keV (and extend up into the SST energy range) that is the cause of the large $\langle v \rangle$.

The electron temperature and the energetic electron flux with energies from a few keV to several hundred keV increase during the most intense auroral brightenings and magnetic field fluctuations. The energetic electron distributions are usually field aligned except during times of rapid flux increase when the distributions are isotropic. The flux of lower energy electrons decreases when the high energy flux increases. Finally, the electron distributions at all energies become more field aligned several minutes after strong magnetic field fluctuations and energetic electron flux increases. This shows up as an increase in the parallel electron temperature over the perpendicular electron temperature.

These observations suggest that there are at least two populations present for

both the ion and electron distributions. Each species has a low density, high energy ($>$ 10 keV) component and a relatively high density, low energy ($<$ a few keV) component. The behavior of these two populations appears anticorrelated. From a single point measurement, it is impossible to determine whether a spatial boundary separates the two populations or whether they are the result of a time dependent energization process.

There is a nearly one-to-one correspondence between the auroral activations and magnetic fluctuations and large $\langle v \rangle$ in the magnetotail. This suggests a causal relationship between them. However, not every auroral brightening is accompanied by large magnetic fluctuations and an increase in $\langle v \rangle$, and not every large $\langle v \rangle$ event has an associated auroral brightening. It is easy to explain the former as a matter of spacecraft location; the flux tube of the spacecraft may not be connected to the region of the ionosphere where the brightening is occurring. For example, looking at the MLT plot in the middle of Figure 3.2, the auroral activity occurs just eastward of the WIND footprint at the beginning of the interval. Likewise, near the end of the period, the auroral activity is mostly occurring westward of the WIND footprint. Conversely, a large increase in $\langle v \rangle$ that is not associated with a brightening in the aurora (e.g. 04:20 UT or 05:30 UT) suggests that the supposed communication between the plasma sheet and ionosphere can be disrupted.

Mapping the region of auroral emission to the equatorial magnetosphere suggests that an area of 60 R_E^2 in the plasma sheet may become disturbed in a few minutes. Finally, a comparison of the plasma sheet and ionospheric electron energy fluxes shows that there is an increase in the plasma sheet electron energy flux coincident with auroral brightenings. However, the ionospheric electron energy flux is always greater than the plasma sheet energy flux indicating that additional energy flux is entering the loss cone. An estimation of the parallel potential drop between the plasma sheet and ionosphere suggests that a total potential of at least several kV is necessary to explain the ionospheric electron energy flux during auroral brightenings.

3.2 Detailed Plasma Behavior

3.2.1 Ion Dynamics

Now we take a closer look at the plasma behavior during the one hour period between 05:20 and 06:20 UT on July 26, 1997. Here we will first examine the ion and electron behavior at coarse ($\sim$ 1 minute) resolution in order to directly compare these measurements to earlier observations with similar resolution. In the next section, we analyze the plasma dynamics using high resolution data.

Figure 3.10 is similar in format to Figure 3.5 except the energy deposition rate into the ionosphere is not plotted. During this one hour interval there are three large $\langle v \rangle$ events. Each of these events, as pointed out in the last section, is associated with strong magnetic fluctuations, density decreases and increases in the ion temperature. There are auroral brightenings associated with two of the events, at 05:45 and 06:00 UT. There is no clear auroral brightening associated with the shortest and least intense event at 05:30 UT.

In the earlier analyses using bulk parameters, these quantities were usually the only ones that were considered when discussing the plasma sheet ion dynamics. Figure 3.11 moves one step beyond this limited view. Figure 3.11, similar to Figure 3.6, presents the UVI keogram, magnetic field data, $\langle v \rangle$ in GSM coordinates and in magnetic field aligned coordinates, and the Earthward and tailward energy spectrograms covering energies from 70 eV to about 1 MeV.

It is clear that the large $\langle v \rangle$ are associated with increases in the energetic ion flux above 10 keV in both the Earthward and tailward directions, though the increases during the 05:30 UT event are relatively minor. In all three cases, the increase in the energetic ion flux is greater in the Earthward direction than it is in the tailward direction. At lower energies, the flux levels drop in the tailward direction during all three events. In the Earthward direction, the lower energy ion flux is relatively unchanged during the 05:30 UT event. The lower energy ion flux drops off dramatically

Figure 3.10: Comparison of one hour of auroral imagery data with plasma sheet magnetic field and ion moments. From top to bottom: keogram; magnetic field; ion density; ion velocity; ion temperature.

Figure 3.11: Comparison of one hour of auroral imagery data with plasma sheet magnetic field and ion data. From top to bottom: keogram; magnetic field; ion velocity in GSM and magnetic field aligned coordinates; ion energy spectrograms.

during both the 05:45 and 06:00 UT events; however, the Earthward flux is still larger than the tailward flux for energies greater than a few hundred eV. Notice that after about 06:00 UT, the flux of ions with energies about 100 eV or so begins to increase in both directions. While not ubiquitous, this very low energy relatively isotropic ion component is seen in the plasma sheet quite often [*Chen et al.*, 2000a].

In all 3 cases, even though $\langle v \rangle$ is primarily directed Earthward, there is a significant component of the velocity parallel to the magnetic field (third panel). This is due to the fact that the X-component is the dominant component of $\mathbf{B}$. However, during the 06:00 UT event, initially there is a significant fraction of $\langle v \rangle$ parallel to the magnetic field. A few minutes later, most of the velocity is directed perpendicular to the magnetic field as $|B_X|$ decreases and B_Z increases. Throughout the magnetic field change, however, $\langle v \rangle$ remains pointed in the Earthward (positive X) direction. This shows that the direction of $\langle v \rangle$ is not dependent upon the direction of $\mathbf{B}$ but remains constant as $\mathbf{B}$ changes in direction.

3.2.2 Electron Dynamics

Figure 3.12 gives us a view of the electron dynamics on an expanded time scale. Similar to Figure 3.7, Figure 3.12 shows the UVI keogram, the magnetic field data, the electron temperature, and the electron pitch angle spectrograms at about 1, 10, 30, and 100 keV. Additionally, the third panel shows the ion velocity for comparison with the electron dynamics.

During the magnetic field fluctuations and the large ion $\langle v \rangle$ events, the electron temperature increases (with a very minor increase at 05:45 UT). Also the fluxes of electrons with energies greater than 10 keV increase while the flux at lower energies decreases. Shortly after the energetic flux increases, the electron distribution becomes more field aligned at all energies. As the energetic electron flux gradually decreases after 06:00 UT, the fluxes at pitch angles near 90° decrease first leaving the distribution highly field aligned.
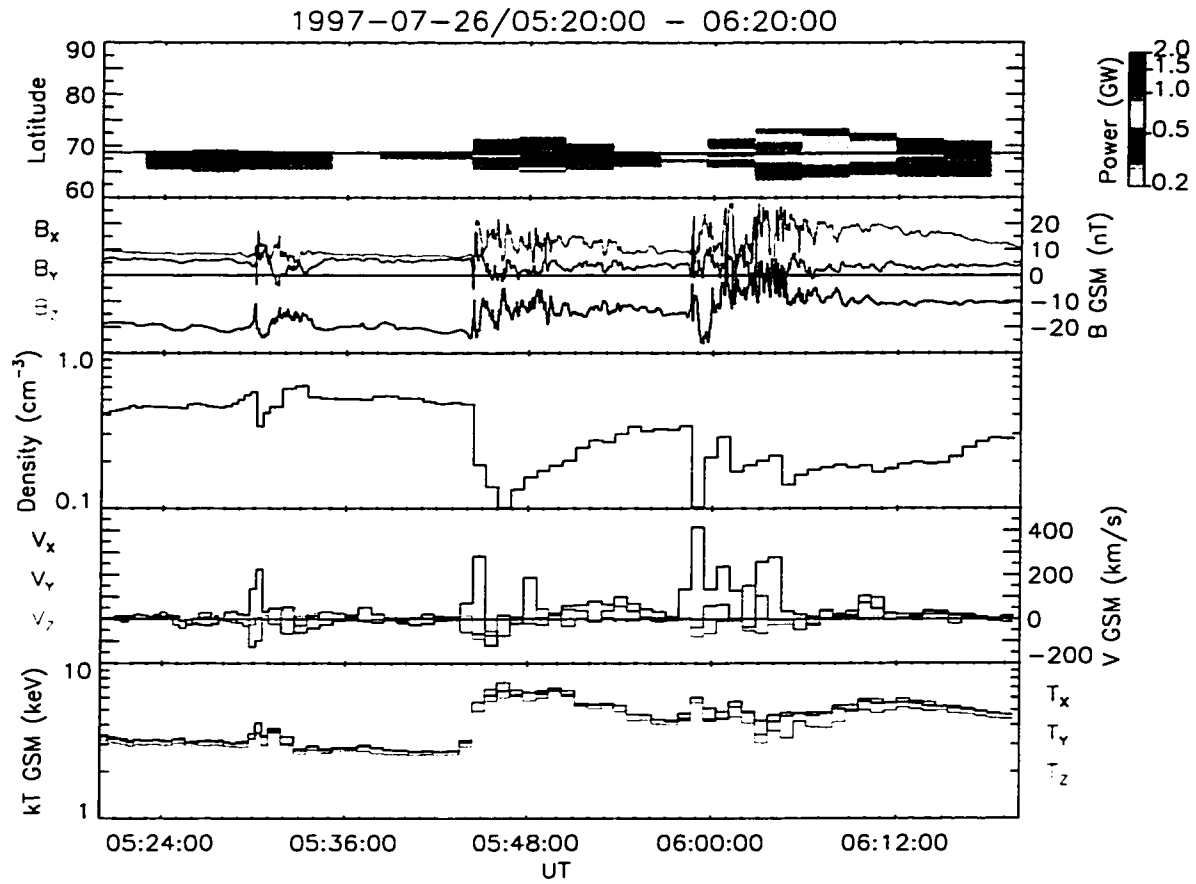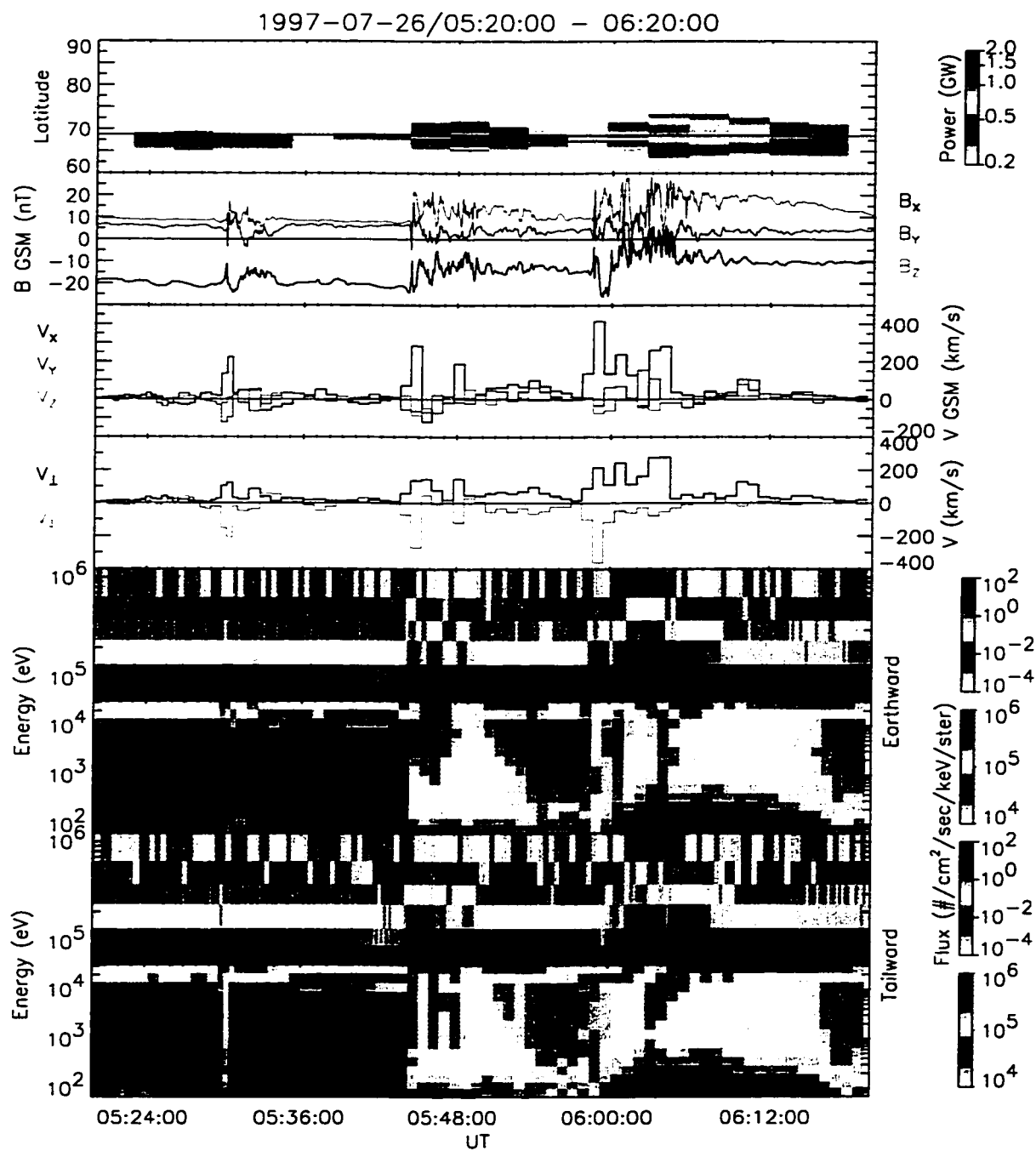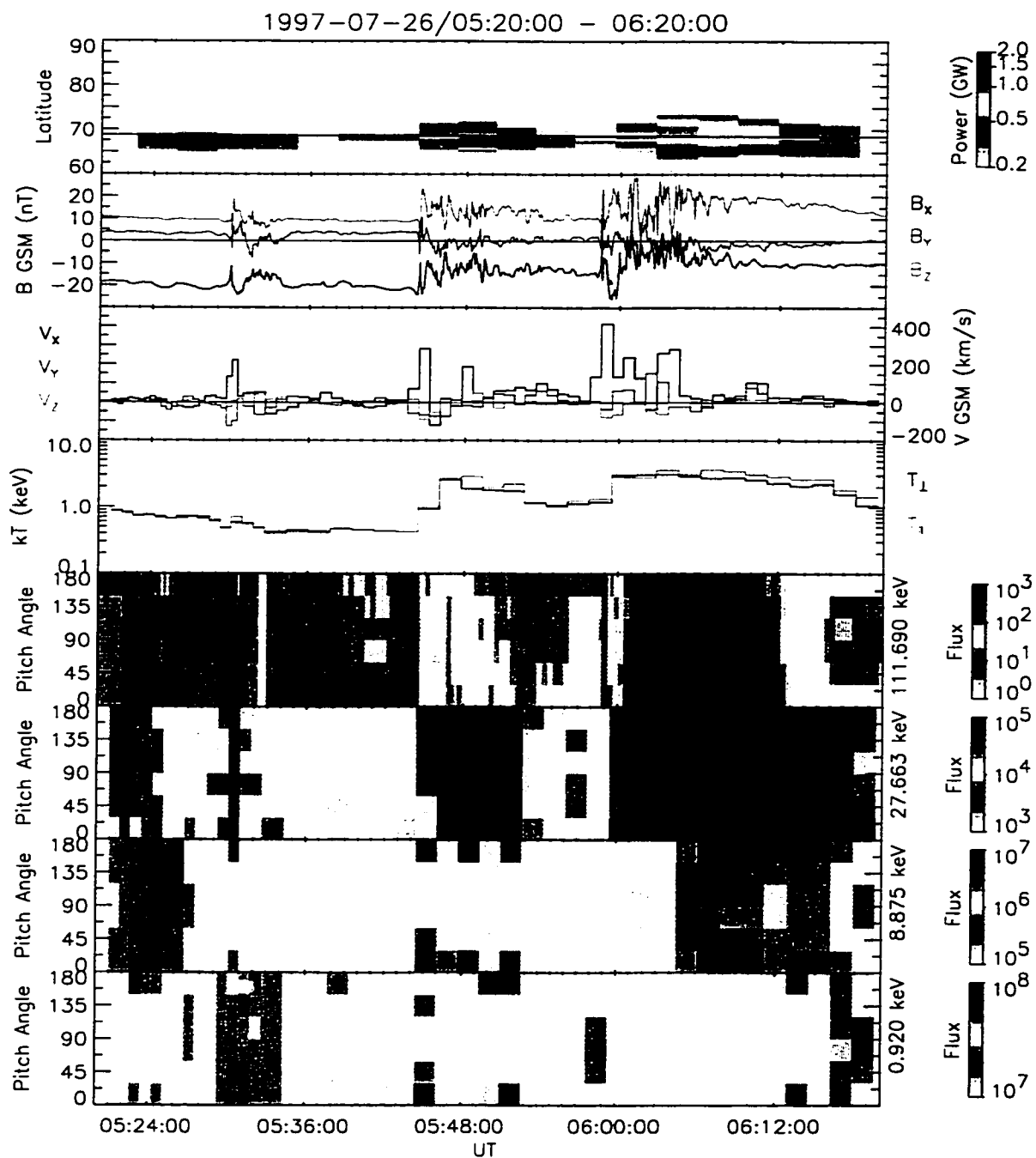
Figure 3.12: Comparison of one hour of auroral imagery data with plasma sheet magnetic field and electron data. From top to bottom: keogram; magnetic field; ion velocity; electron temperature; electron pitch angle spectrograms.

3.2.3 Plasma Distribution Functions and Spectra

Next, in order to better understand the detailed dynamics of the plasma sheet during large $\langle v \rangle$ events, we look at representative ion and electron distribution functions before, during, and after the large $\langle v \rangle$ events at 05:45 and 06:00 UT. Figure 3.13 shows the magnetic field, ion distribution functions, and electron distribution functions for the 05:45 UT large $\langle v \rangle$ event. The top plot shows the high resolution (46-millisecond) magnetic field data in GSM coordinates. The middle panels show five consecutive PESA-H distribution functions each integrated over 50 seconds. The first row shows isocontours of the ion velocity distribution functions. These are two-dimensional slices of the full three-dimensional distributions in the $\mathbf{B} - \mathbf{V}_\perp$ plane in the spacecraft frame of reference. The horizontal and vertical axes are velocities parallel and perpendicular to the magnetic field, respectively. The numbers in the upper left, upper right, and lower right are the magnetic field elevation, azimuth (both in GSM), and magnitude averaged over the integration time. The small cross in each contour plot indicates the direction and magnitude of $\langle v \rangle$. The next row shows cuts of the contour plots in the directions parallel (red asterisks) and perpendicular (blue diamonds) to the averaged magnetic field. The horizontal axis is velocity; the vertical axis is the logarithm of the phase space density in $\text{sec}^3\text{cm}^{-6}$. The smooth solid red and blue lines represent the instrument noise level in the particular direction. Since the detector has a variable angular resolution depending upon look direction, the one-count level depends upon look direction. The bottom panels show the isocontour plots and one-dimensional cuts for three consecutive electron distributions. Each distribution is integrated over 3 seconds, and the time between distributions is 1 minute 40 seconds.

The first ion and electron distributions are integrated during a period when the magnetic field is steady. The distributions are isotropic as shown by the circular, concentric contours and by the agreement in the parallel and perpendicular cuts. Near the end of the integration of the next ion distribution, the magnetic field has
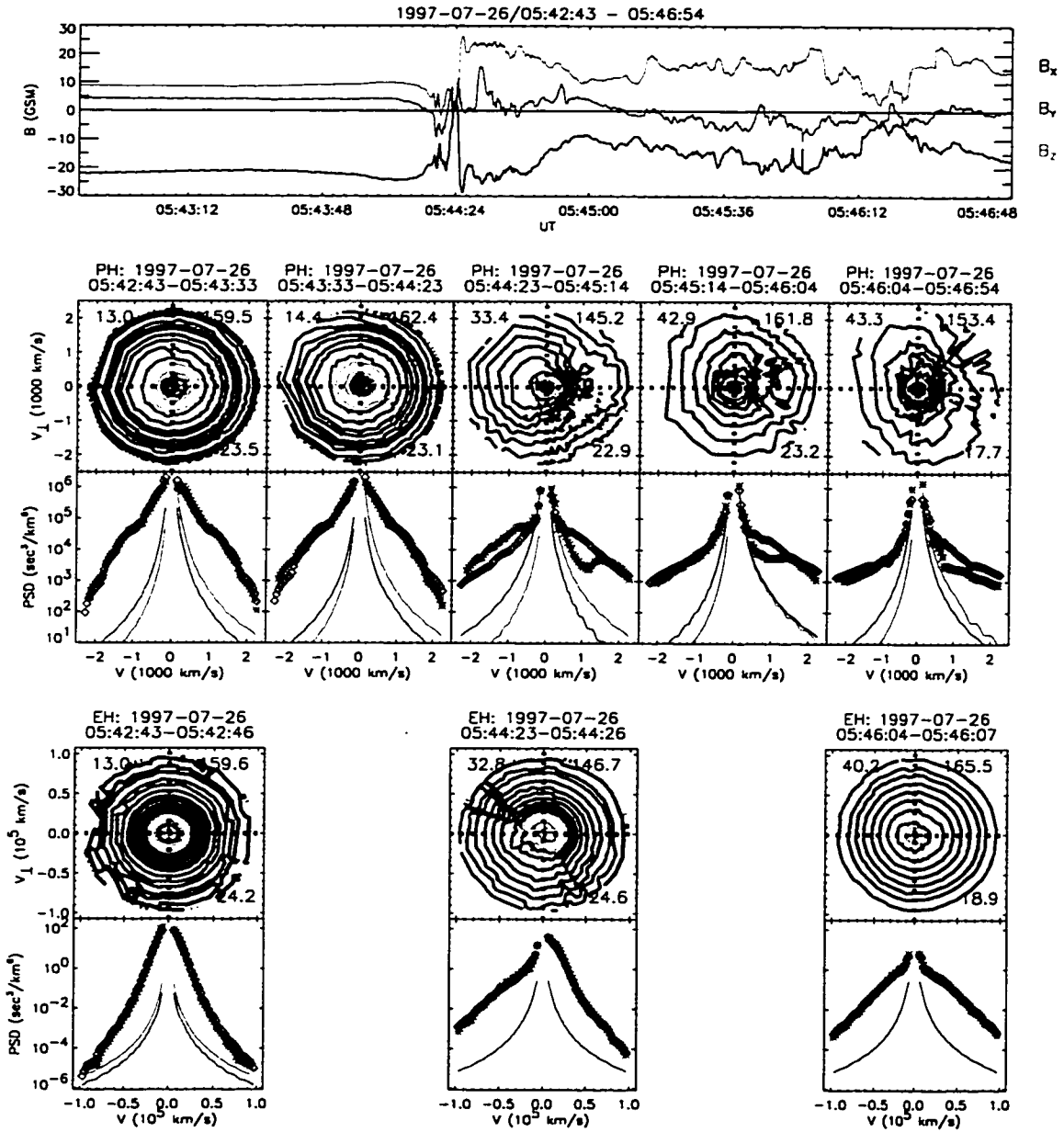
Figure 3.13: Ion and electron distribution functions covering the time interval 05:42:43 to 05:46:54 UT. The magnetic field is plotted for comparison.

begun to fluctuate. Also, we see a change in the behavior of the high energy ions. There is an increase in the ion phase space density in the upper left quadrant of the contour plot at energies above 10 keV (velocities above about 1500 km/s). This also appears in the 1-D cuts as an anisotropy at high energies. Note that $\langle v \rangle$ is about 100 km/s at this time (Figure 3.10 and Figure 3.11). The next distribution, which corresponds to the peak $\langle v \rangle$ of ~ 300 km/s during this event, is much more complex and displays multiple components. The increase in the energetic ion component in upper left quadrant that was present in the last distribution is now much larger. Also there is a beam directed along the magnetic field centered at about 10 keV. However, the direction of $\langle v \rangle$ as indicated by the small cross is almost $180°$ away from the beam. Neither the velocity moment nor the energy spectrograms give an indication of the complexity and dynamical nature of this distribution. In the fourth ion distribution, the field aligned, energetic beam is still present but not as intense as in the previous distribution. The phase space density enhancement in the upper left quadrant is no longer present; however the phase space density in the "positive" perpendicular direction (that is, the $(\mathbf{B} \times \mathbf{V}) \times \mathbf{B}$ direction) at the top of the contour plot is enhanced over the phase space density at the bottom of the plot. In the final ion distribution, the field aligned beam is no longer present. The distribution appears much hotter in the perpendicular direction than it does in the parallel direction. An anisotropy remains at high energies resulting in a $\langle v \rangle$ of < 100 km/s.

The first electron distribution is isotropic. The second electron distribution, integrated when the magnetic field is fluctuating and when the parallel beam is observed in the ions, appears very complex. There appears to be two populations present, a hot one and a lower energy one, that are not organized by the magnetic field but separated by a line that runs approximately from upper left to lower right. This is thought to be the result of time aliasing and will be discussed more in the following paragraphs. The final electron distribution again appears mostly isotropic. This distribution is composed of two populations: a low energy component that has decreased

relative to the first distribution and a higher energy component that has increased relative to the first distribution. They are separated by a break in the spectrum seen in the 1-D cuts around 1 keV. The low energy component also appears to be slightly field aligned.

Another way to study the dynamics of these particles is to examine the behavior of the differential energy spectra. Figure 3.14 shows examples of the ion and electron energy spectra for the same time interval shown in Figure 3.13. The top row contain the energy spectra for ions. For each plot there are 120 curves in the energy range from 70 eV to 30 keV corresponding to the 120 look directions of PESA-H and 40 curves in the energy range from 67 keV to 7 MeV corresponding to the 40 look directions of the ion SST. Again, the PESA-H spectra are integrated over 50 seconds. The ion SST spectra are integrated over 6 seconds. Red colors correspond to ion fluxes in the positive X-direction (Earthward); blue colors correspond to ion fluxes in the tailward direction.

The second row contains the energy spectra for electrons. For each plot there are 88 curves in the energy range from 100 eV to 30 keV corresponding to the 88 look directions of EESA-H and 40 curves in the energy range from 22 keV to 7 MeV corresponding to the 40 look directions of the electron SST. All EESA spectra are integrated over 3 seconds; electron SST spectra are integrated over 12 seconds. The integration times of the electron spectra begin at the same time as the ion spectra above them. For the electrons, red colors correspond to fluxes in the direction of the local magnetic field, and blue colors correspond to fluxes in the direction opposite of the magnetic field.

The first panel shows the ion energy spectra representative of the quiet plasma sheet. There is little spread in the curves indicating that the ion fluxes in all directions are nearly equal, i.e., the distribution is isotropic (cf. the first ion distribution in Figure 3.13). In the second panel, there is a slight enhancement in the ion flux at energies greater than about 10 keV in the Earthward direction. The third panel shows
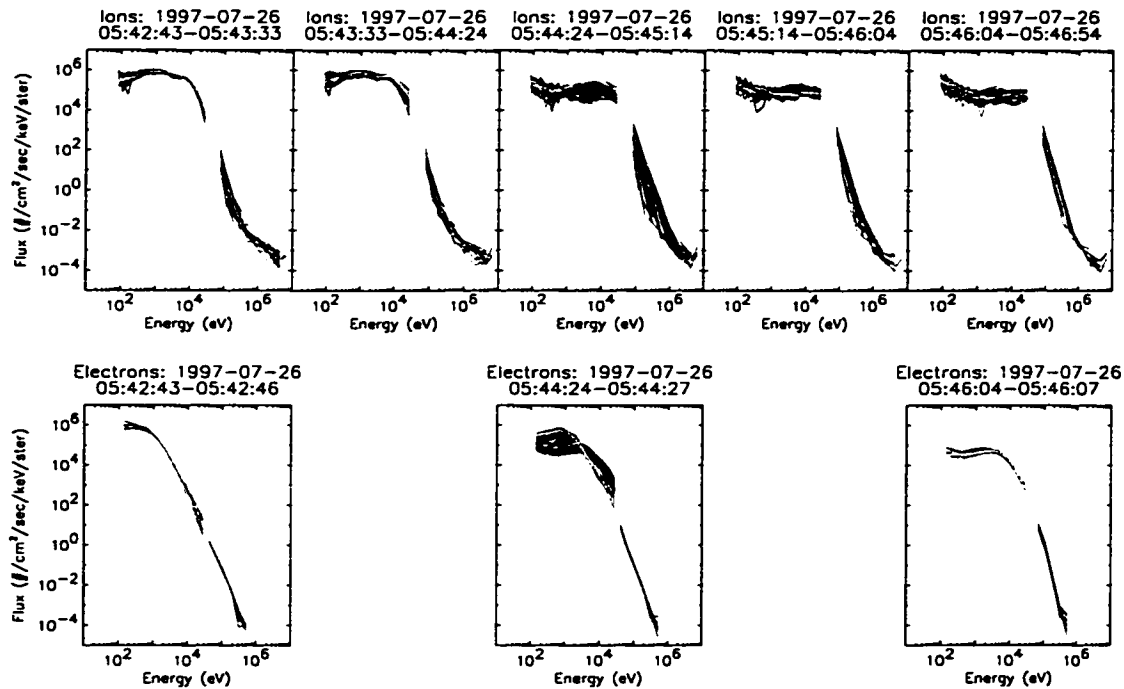
Figure 3.14: Ion and electron differential energy spectra covering the time interval 05:42:43 to 05:46:54 UT.

a significant change in the spectrum. The fluxes of ions with energies greater than 10 keV (the SST data and the top end of the PESA-H data) have increased and are very anisotropic with higher fluxes in the Earthward direction. The fourth panel reveals the presence of a weak tailward beam centered at a few keV (the tailward beam was overwhelmed by the flux increase in the Earthward direction in the third panel). Finally, the fifth panel shows a distribution slightly more isotropic than the previous two. Below 30 keV, the spectra in the fifth ion spectrum plot are flat. Compared to the first spectrum plot, the high energy (from > 10 keV up to MeV) flux has increased while fluxes at lower energies have decreased. These plots clearly show that the ion flux increases up to MeV energies, and that the directional anisotropies also extend up to these high energies.

The first electron plot shows the relatively isotropic electron distribution. At the lowest energies ($\sim$ 100 eV), the electrons appear field aligned. The second electron panel appears to be a mixture of the spectra from the first and third panels. The EESA-H spectra are very anisotropic but are not organized clearly by the magnetic field. The final electron plot shows a spectrum very much changed from the first panel. The electron flux at energies below a few keV have decreased while fluxes at energies above a few keV up to several hundred keV have increased. Likewise, the slope of the spectrum at SST energies has greatly increased.

Figure 3.15 is identical in format to Figure 3.13. Figure 3.15 covers five consecutive ion distributions during and after an interval of large $\langle v \rangle$. The onset of large $\langle v \rangle$ occurred about 4 minutes before the first distribution in Figure 3.15 at 05:58 UT. At 06:02 UT, the ion $\langle v \rangle$ is roughly 150 km/s. As seen in the first contour plot and 1-D cut, $\langle v \rangle$ is directed perpendicular to the ambient magnetic field due to the anisotropy of the energetic ions in the perpendicular direction. Also notice that there is a relatively high density, very low energy, isotropic core population. This cold population is clearly seen in the energy spectrograms in Figure 3.11. There is a large (almost an order of magnitude) drop in the phase space density in the "negative" perpendicular direction (the $-(B \times V) \times B$ direction) in the next distribution, leading to an even larger anisotropy in the perpendicular direction. The ion $\langle v \rangle$ increases to nearly 300 km/s. In the absence of the stagnant low energy component, the $\langle v \rangle$ would likely be much higher. The phase space density begins to recover during the next distribution. During the last two ion distributions in this figure, the ion $\langle v \rangle$ drops to less than 50 km/s. These distributions are still anisotropic with the width of the energetic component in the perpendicular direction slightly larger than the width in the direction parallel to the magnetic field.

In contrast to Figure 3.13, there are only two electron distributions shown. In both cases, the distributions are similar to the final distribution in Figure 3.13 and much hotter than the first electron distribution in that figure. In addition, the low
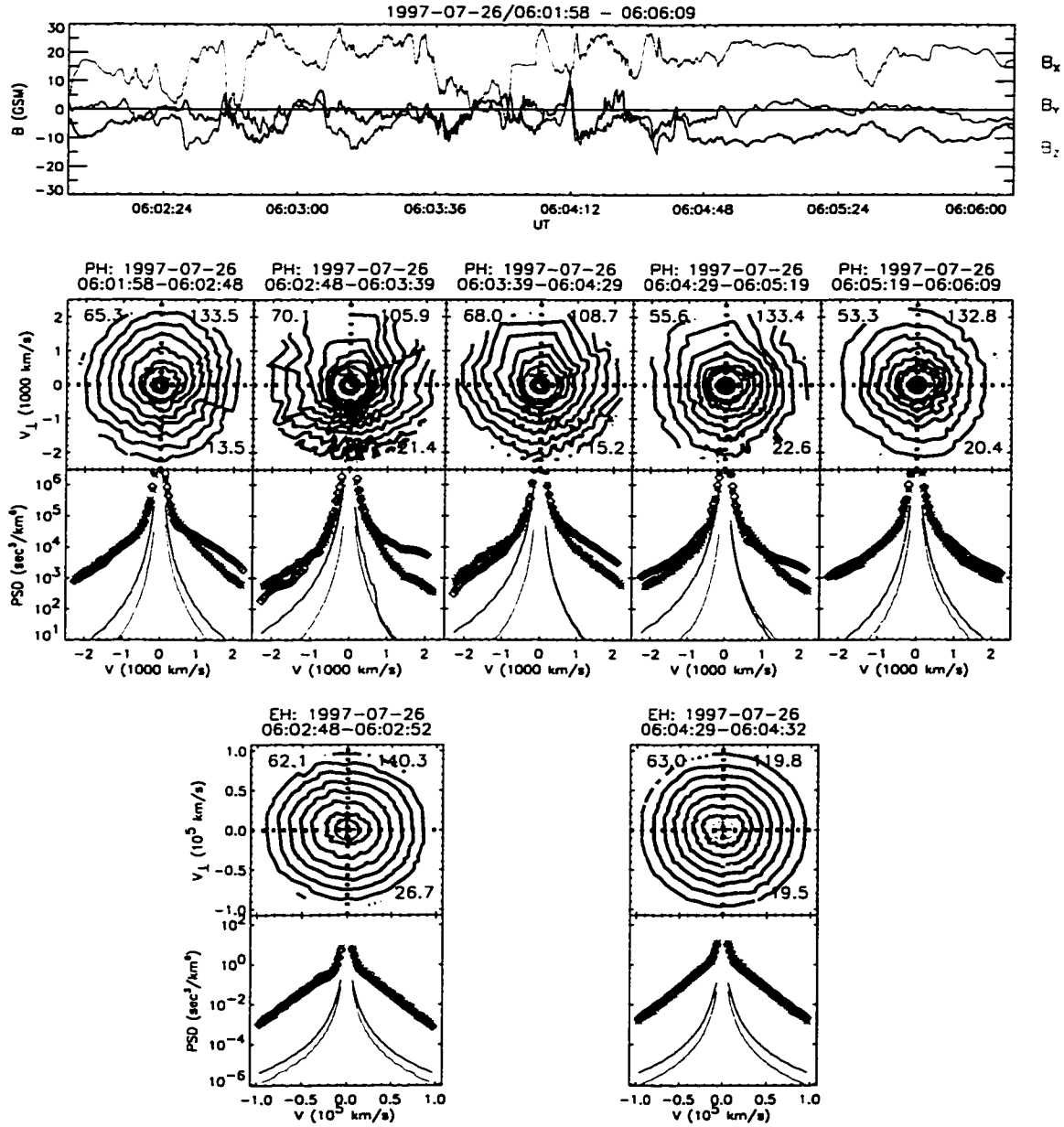
Figure 3.15: Ion and electron distribution functions covering the time interval 06:01:58 to 06:06:09 UT. The magnetic field is plotted for comparison.

energy component appears slightly peaked in the field aligned and anti-field aligned directions.
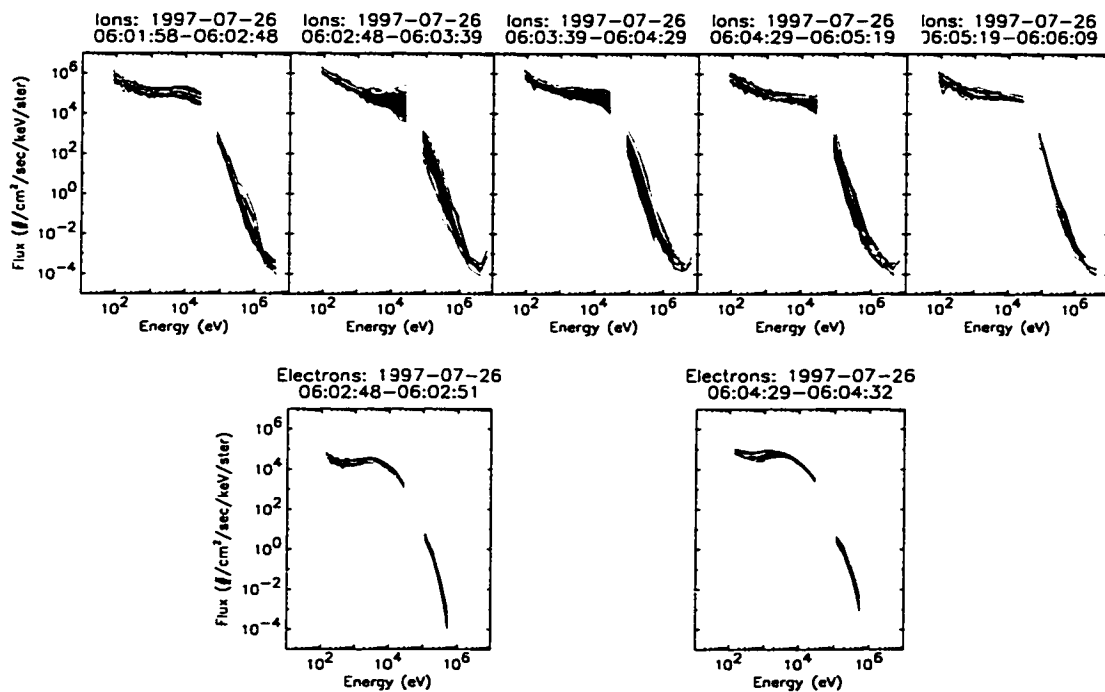
Figure 3.16: Ion and electron differential energy spectra covering the time interval 06:01:58 to 06:06:09 UT.

The differential energy spectra for the distributions in the previous figure are shown in Figure 3.16. The format of this figure is identical to that of Figure 3.14. All of the spectra show both low and high energy components. The high energy ion component is highly anisotropic with higher fluxes in the Earthward direction. These anisotropies extend up to MeV energies. The broad widths of these spectra in the vertical direction are associated with strong gradients in phase space density. In the second ion plot, there are nearly two orders of magnitude separating the Earthward and tailward fluxes at 30 keV. These large anisotropies at high energy begin to

decrease in the last two ion panels. The two electron spectra appear relatively similar to each other and are similar to the electron spectra in the third panel in Figure 3.14.

It is important to point out that there are large magnetic field variations during the integration times of the particle distribution functions and energy spectra. As a result, the distributions may be time aliased. As a case in point, let's examine the electron distribution from 05:44:23 UT.

The electron distributions are integrated over one spacecraft rotation. EESA-H and EESA-L instantaneously measure the 2-D electron distribution. As WIND makes one complete rotation in 3 seconds, the entire 3-D distribution is sampled. This fact allows us to look at electron data with sub-spin time resolution. Figure 3.17 shows the electron energy flux (normalized count rate) in four selected energy channels for one 3.14 second spacecraft revolution. The energy flux has been divided into 16 equal bins with a resulting time resolution of about 200 msec. The error bars are calculated from Poisson counting statistics. The two bottom panels show the magnetic field magnitude and magnetic field azimuth and elevation angles for comparison.

At the beginning of the integration, the energy flux in the 1 keV energy channels is higher than the energy flux in the 3 and 9 keV channels. About 2 seconds later, the 1 keV energy flux begins to decrease while the 9 keV energy flux begins to increase. The 3 keV energy flux remains largely unchanged. At the end of the integration time, the 9 keV energy flux is the highest while the energy flux in the 1 keV channels are the lowest. This signifies a change in the electron spectrum during the 3 second integration time. It appears that we are observing the change in the electron distribution from that seen in the first electron energy spectrum plot in Figure 3.14 at 05:42:43 UT to that in the third plot at 05:46:04 UT. The spectrum change takes place rapidly, in about 1 second.

Note that the electron energy flux in the 1 keV energy channel are measured by both EESA-H and EESA-L. The energy flux in this energy range from both detectors agree quite well throughout the entire integration period including during the rapid
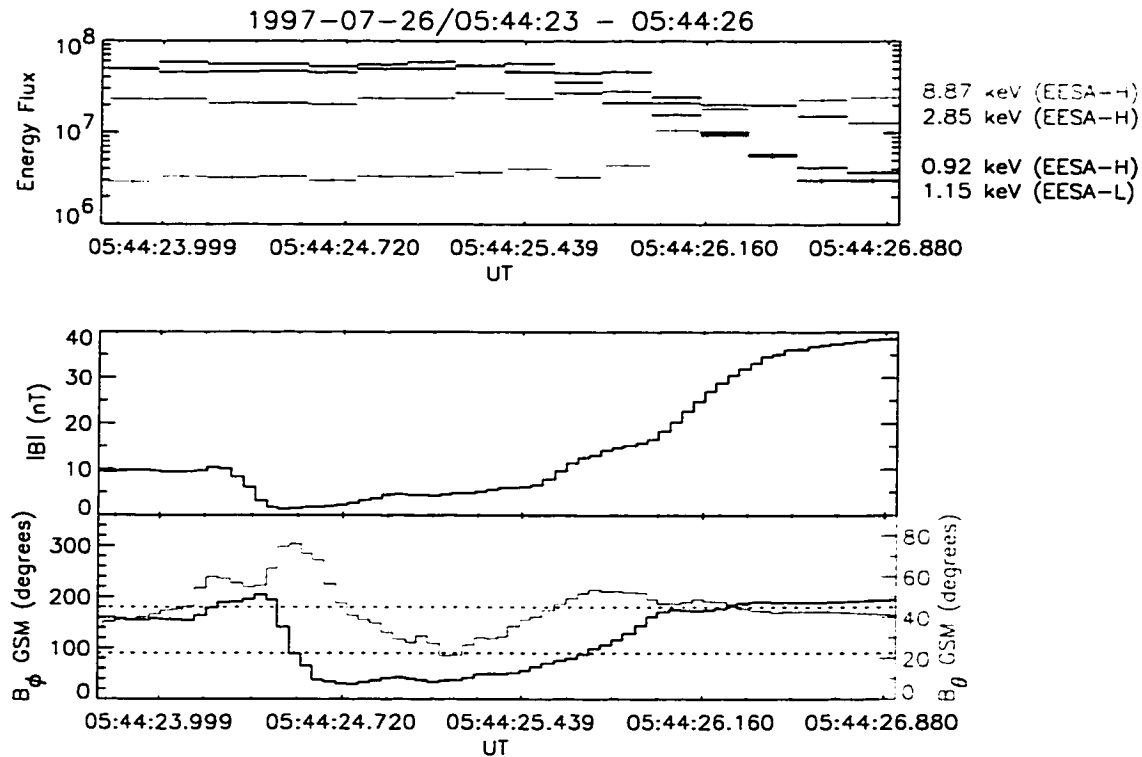
Figure 3.17: Electron and and magnetic field data at sub-spin resolution. Top: electron energy flux in four energy channels. Bottom: magnetic field magnitude, azimuth, and elevation.

change in spectrum. As mentioned in Chapter 2, the fields-of-view of EESA-H and EESA-L are offset by 90°. Such good agreement of these detectors looking in different directions suggests that the change in the electron population occurs simultaneously in all directions.

During the integration time, |B| rises from its minimum value of 1.4 nT to its maximum value of 39 nT in just over 2.5 seconds. Additionally, the direction of the magnetic field changes by nearly 180° while its magnitude is increasing. This yields a $\partial|B|/\partial t \approx 15$ nT/s and results in a large induced electric field. During the magnetic field increase, the electron gyroperiod varies from about 1 to 25 milliseconds. Since

the increase in |B| occurs on time scales much longer than the electron gyroperiod, the electrons are expected to behave adiabatically. The proton gyroperiod, on the other hand varies from about 45 seconds to just under 2 seconds. This suggests that the protons cannot behaving adiabatically, and that indeed kinetic effects are important.

Figure 3.17 provides good evidence that the electron distribution, integrated over 3 seconds, is time aliased. If so, then the ion distribution, integrated over 50 seconds is almost certainly time aliased, too. Unfortunately, there is no 3-second ion data at this time, so there is no way to extract some of the ion time variations like we can for the electrons. It is possible that the complex ion distribution functions in Figure 3.13 and Figure 3.15 are the result of time aliasing. For example, in the third ion distribution in Figure 3.13, it is unknown whether the two components (the parallel beam and the enhancement in phase space density in the upper left quadrant) were present at the same time or whether these two components were sampled during different parts of the integration.

3.2.4   Relative Timing Between Onset Signatures

Now we will address the issue of relative timing between the onset signatures seen in the aurora and in the particles and magnetic field in the plasma sheet. We will focus on the 05:45 and 06:00 UT events as representative examples.

From examining each UVI image, the first brightening of the UV aurora associated with the 05:45 UT event started between 05:43:00 and 05:44:13 UT. The first significant change in ion distribution occurs during the distribution sampled from 05:43:33 to 05:44:23 UT (second ion distribution in Figure 3.13). During this distribution, $\langle v \rangle > 100$ km/s. The first disturbed electron distribution seen with EESA-H occurs during the integration from 05:44:23 to 05:44:26 UT. However, the previous EESA-H distribution was integrated from 05:42:43 to 05:42:46 UT, and there was no signature present during this time. Therefore, the electron distribution must have changed sometime between 05:42:46 and 05:44:26 UT. Similarly, the first change in the electron

distribution seen with EESA-L occurs during the 05:44:23 to 05:44:26 UT distribution. There is no EESA-L data since 05:43:36 UT, so the change in the electron distribution as seen by EESA-L must have occurred between 05:43:36 and 05:44:26 UT. Determining the onset time from MFI can be a little bit trickier. One method is to pick out the start time of the rapid magnetic field fluctuations. However, upon closer examination, it is noticed that the magnetic field usually begins to slowly vary before the onset of rapid fluctuations. So here we define the onset time as the time when any of the three magnetic field components reaches a point three standard deviations away from the average of that component over the minute (> 1000 data points) before the fluctuations begin.

Figure 3.18 shows how the time of onset determined from five different instruments compares. From top to bottom, we show the onset time determined from UVI, PESA-H, EESA-H, EESA-L, and MFI. The bottom plot also shows the magnetic field magnitude. The first onset time (vertical line) shows the onset time determined by the method described above. The second time marks the beginning of the large amplitude magnetic fluctuations. These onset times differ by about 20 seconds. The remaining plots simply show the time interval during which either the particle distributions changed or the aurora brightened.

Within the uncertainties of all of these instruments, of which EESA-H's is the greatest since the time between distributions is almost two minutes, all of the signatures present in the plasma, magnetic field, and the aurora are simultaneous.

From our earlier discussion about the electron distribution at 05:44:23, we concluded that we observed the change in the electron distribution in progress, and that this change occurred two seconds into the three-second integration period at about 05:44:25 UT. This time is over 10 seconds after the increase in the auroral luminosity as observed by UVI and would suggest that the aurora brightens before the plasma sheet electrons are affected. However, by comparing the electron spectrum from the previous EESA-H distribution at 05:42:43 to that during the first two seconds of the
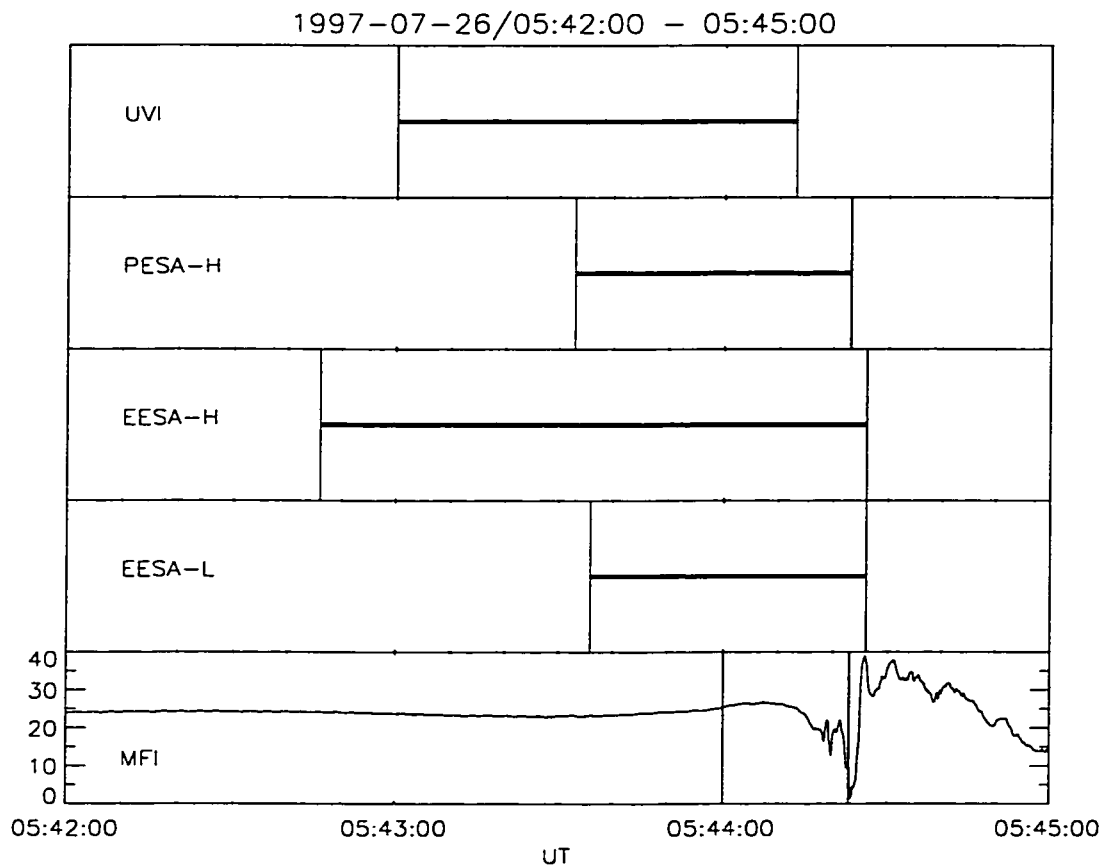
Figure 3.18: Comparison of onset time from five different instruments for the 05:45 UT ⟨v⟩ event. From top to bottom: onset time from UVI, PESA-H, EESA-H, EESA-L, and MFI.

05:44:23 distribution, we see a noticeable change in the electron spectrum. Electron fluxes below about 500 eV decrease while electron fluxes above this energy increase. The change that occurs during the 05:44:23 distribution is much more drastic, however. Therefore, we conclude that the initial electron distribution change occurs between 05:42:46 and 05:44:23 UT, and that additional changes can occur later.

The second auroral brightening during this interval occurs between 05:58:20 and 05:59:33 UT. Based on inspection of the particle distribution functions, the ions change during the PESA-H integration from 05:57:47 to 05:58:37 UT. The electrons as observed by EESA-H first change between the distribution at 05:57:47 to 05:57:50 UT and the distribution at 05:59:27 to 05:59:30 UT. For EESA-L, the first change is seen in the distribution at 05:58:37 to 05:58:40 UT. However, the previous EESA-L integration ended at 05:57:50 UT, so the electron distribution much have changed between 05:57:50 and 05:58:40 UT. Finally, MFI shows a gradual change beginning at 05:58:12 UT with the onset of large fluctuations near 05:58:34 UT, about 20 seconds later.

Figure 3.19 compares the onset times graphically in the same format at Figure 3.18. Again, within the uncertainties of the instruments, the timing is consistent with all signatures being simultaneous in the ionosphere and plasma sheet.

3.2.5 Summary of Observations

As mentioned in the last section, this detailed data shown here indicates that auroral brightenings are associated with large amplitude, high frequency fluctuations in the magnetic field, decreases in the plasma density, increases in the Earthward ion $\langle v \rangle$, and increases in the ion temperature. At the same time, differential energy spectra show that the energetic ion flux from a few 10s of keV up to 1 MeV increases in all directions with increases in the Earthward direction larger than increases in the tailward direction. At lower energies, the ion flux decreases in all directions, but the fluxes are still anisotropic. Below 100 eV the ion fluxes are isotropic and are
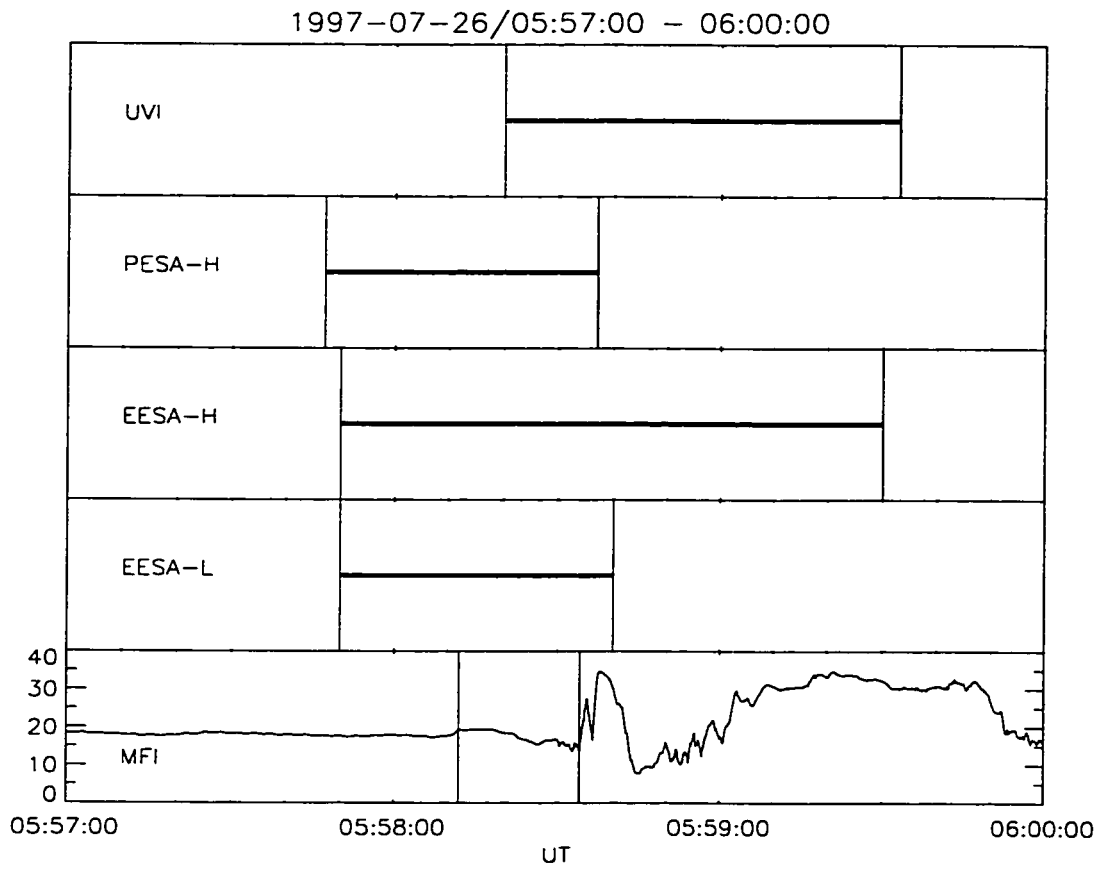
Figure 3.19: Comparison of onset time from five different instruments for the 06:00 UT ⟨v⟩ event. From top to bottom: onset time from UVI, PESA-H, EESA-H, EESA-L, and MFI.

increased after the 06:00 UT event. Additionally, the electron temperature increases due to a hardening of the spectrum as high energy ($>$ a few keV) fluxes increase and lower energy fluxes decrease. As the electron fluxes begin to recover, the distributions become field aligned.

Examination of the particle distribution functions reveals dynamic and complex ion and electron distributions. The ion distributions can be composed of multiple components behaving dynamically differently. The distributions can contain hot anisotropic components, beams, sharp gradients in phase space density, and a low energy stagnant component. The electron distribution is seen undergoing a rapid change in spectrum in 1 second.

The multicomponent nature of the ion distribution functions during intervals of large $\langle v \rangle$ shows that the large $\langle v \rangle$ are not due to an $E \times B$ drift as is usually assumed [*Angelopoulos et al.*, 1997; *Fairfield et al.*, 1999]. For example, the third and fourth ion distributions in Figure 3.13 show one component of the distribution anisotropic in the direction perpendicular to the magnetic field in the spacecraft frame. An electric field vertically out of the page ($-V \times B$ direction) could account for the anisotropy; however, there is also a beam component parallel to B that is not shifted in the perpendicular direction. The presence of the unshifted beam component argues against the presence of an electric field. Likewise, the two component ion distributions in the second and third distributions of Figure 3.15, one component shifted perpendicular to B and the other not, argue against the large $\langle v \rangle$ being the result of an $E \times B$ drift.

An alternative explanation for these seemingly non-gyrotropic distributions includes particle gradients. Strong energetic particle density gradients in the $V \times B$ direction (into the page) could reproduce the distributions seen in Figure 3.15.

Another possible explanation is that these distributions may be the result of time aliasing. The electron distributions show clear evidence of time aliasing during rapid magnetic field changes. The ion distributions could be similarly time aliased.

Finally, a comparison of the various auroral, magnetic field, ion, and electron

signatures indicates that the onset of all of the signatures occurs simultaneously within the uncertainties of the different instruments.

3.3 Plasma Observations on Kinetic Time Scales

During the 06:30 UT auroral brightening and large $\langle v \rangle$ event on July 26, 1997, PESA-H, EESA-L, and the SSTs were operating in burst mode, i.e., they measured the three-dimensional ion and electron distribution functions for each 3 second spacecraft spin. This allows us to obtain ion data with a time resolution comparable to the local proton gyroperiod.

3.3.1 Ion and Magnetic Field Behavior

Figure 3.20 shows a detailed look at the ion moments and magnetic field variations from 06:29 to 06:36 UT. At this time, WIND was at a GSM position of [-11, 2, 0.5] R_E. The figure shows, from top to bottom, the ion density, components of $\langle v \rangle$ (plus $|v|$) and temperature in GSM coordinates, three components of the magnetic field in GSM coordinates (plus $|B|$) the time derivative of the magnitude of the magnetic field, and a dynamic frequency spectrogram of the magnetic field.

The ion moments are calculated from the three-dimensional ion distribution functions integrated over 3.1 seconds (one spacecraft rotation and approximately the local proton gyroperiod) which were continuously sampled for the entire nearly 7 minute interval. The magnetic field data has a time resolution of 0.046 seconds. The dynamic frequency spectrogram was created by computing the Fast Fourier Transform for every 10 second interval of magnetic field data. The wave power in nT^2/Hz is plotted as a function of frequency from about 11 Hz (the Nyquist frequency) to 0.1 Hz and UT. The solid black line represents the local proton gyrofrequency and the red line represents the local lower hybrid frequency. Note that there is a 3 second sinusoidal variation most apparent in the X and Y components of B before 06:30 UT due to the
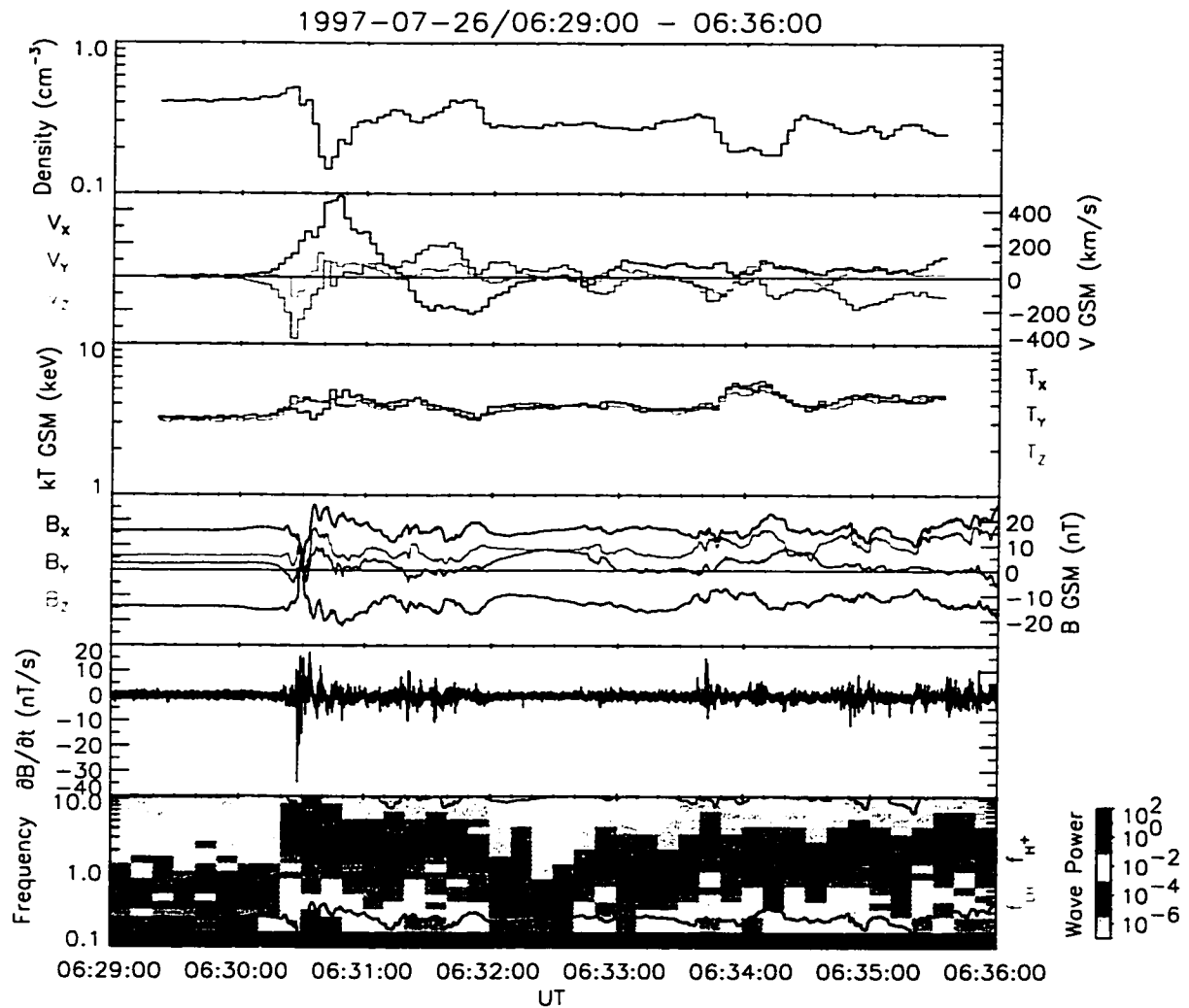
Figure 3.20: High time resolution magnetic field data and ion moments. From top to bottom: ion density; ion velocity; ion temperature; magnetic field; time derivative of the magnetic field; dynamic frequency spectrogram.

spacecraft rotation. As a result, there is a horizontal band centered on 0.3 Hz and a weaker band centered on 0.6 Hz before 06:30 UT present in the dynamic frequency spectrogram.

An important feature in this figure is the large changes seen in the ion density and $\langle v \rangle$ on time scales comparable to the proton gyroperiod. After 06:30 UT, the density increases gradually reaching its maximum value at 06:30:23 UT. Over the next 15 seconds, the density decreases by over a factor of 3, reaching it minimum value at 06:30:39 UT. During this interval, $|\mathbf{B}|$ passes through its minimum value of about 2.5 nT, corresponding to a local proton gyroperiod of about 26 seconds.

Before 06:30:12 UT, $\langle v \rangle$ increases very gradually, primarily in the $-Y$-direction. At 06:30:24 UT, the component of the velocity perpendicular to $\mathbf{B}$ (mostly in the $-Y$-direction) increases by almost 100% in 3.1 seconds. The X-component of $\langle v \rangle$ increases by 50% near 06:30:40. This leads to two peaks in $|\langle v \rangle|$ within a few gyroperiods of each other. The first peak is centered about 06:30:24 UT and is directed mainly in the $-Y$-direction with a smaller $-Z$-component. The second peak is centered around 06:30:45 UT and is directed largely in the X-direction.

The ion temperature does not increase much during this interval. However, it is clear that the temperature is not isotropic during the large $\langle v \rangle$. The three components of the temperature that are shown are not equal.

The rapid, large amplitude variations in the magnetic field on time scales faster than the proton gyroperiod can be clearly seen in the plot of the magnetic field. Near 06:30:30 UT, B_X briefly changes sign indicating that WIND may have crossed a current sheet or encountered strong local turbulence. There is also a brief excursion of B_Z to negative values just after the B_X sign change during the period of Earthward dominated $\langle v \rangle$.

$\partial B / \partial t$ can get quite large with a peak near -35 nT/s. More typical values are on the order of 10 nT/s. This translates to induced electric field strengths of several to 10 mV/m at scale lengths of the thermal proton gyroradius (several hundred km).

The dynamic frequency spectrogram shows significant wave power up to and exceeding the local proton gyrofrequency for an extended interval. There is also significant wave power above the local lower hybrid frequency for a short amount of time as the magnitude of **B** passes through a minimum. Since the fastest proton gyroperiod during this interval is about 2.5 seconds and the more typical value is 4 seconds, the ions cannot be behaving adiabatically during such large magnetic field changes over such short time scales.

Figure 3.21 again shows the magnetic field and ion $\langle v \rangle$ for reference. In addition, it shows the ion $\langle v \rangle$ in magnetic cooridantes, the omnidirectional ion flux at selected energies, and the Earthward and tailward energy spectrograms. In contrast to Figures 3.6 and 3.11, Figure 3.21 only displays SST data up to 300 keV in the energy spectrograms due to low counts.

The third panel shows that there are two peaks in the perpendicular velocity and one large peak in the parallel velocity. The first perpendicular peak corresponds to the peak in $\langle v \rangle$ in the Y-direction. The second perpendicular peak and the parallel peak both correspond to the large peak in the X-component of $\langle v \rangle$. As the direction of **B** changes (dipolarizes), the X-component of the velocity is first directed perpendicular and then parallel to the magnetic field suggesting that the direction of $\langle v \rangle$ is not constrained by the direction of **B**.

The fourth panel shows two increases in the omnidirectional ion flux at energies above 20 keV associated with the two peaks in $\langle v \rangle$. Fluxes below this energy decrease during the second velocity peak.

The energy spectrogram plots are similar to those we have shown earlier. There is an increase in the fluxes in both directions at energies greater than a few 10s of keV, though the flux increase in much greater in the Earthward direction. There is a large drop in the tailward ion flux at energies from $\sim$ 10 keV to 1 keV. There is also considerable structure present in these energy spectrograms with alternating Earthward and tailward anisotropies leading to variable $\langle v \rangle$.
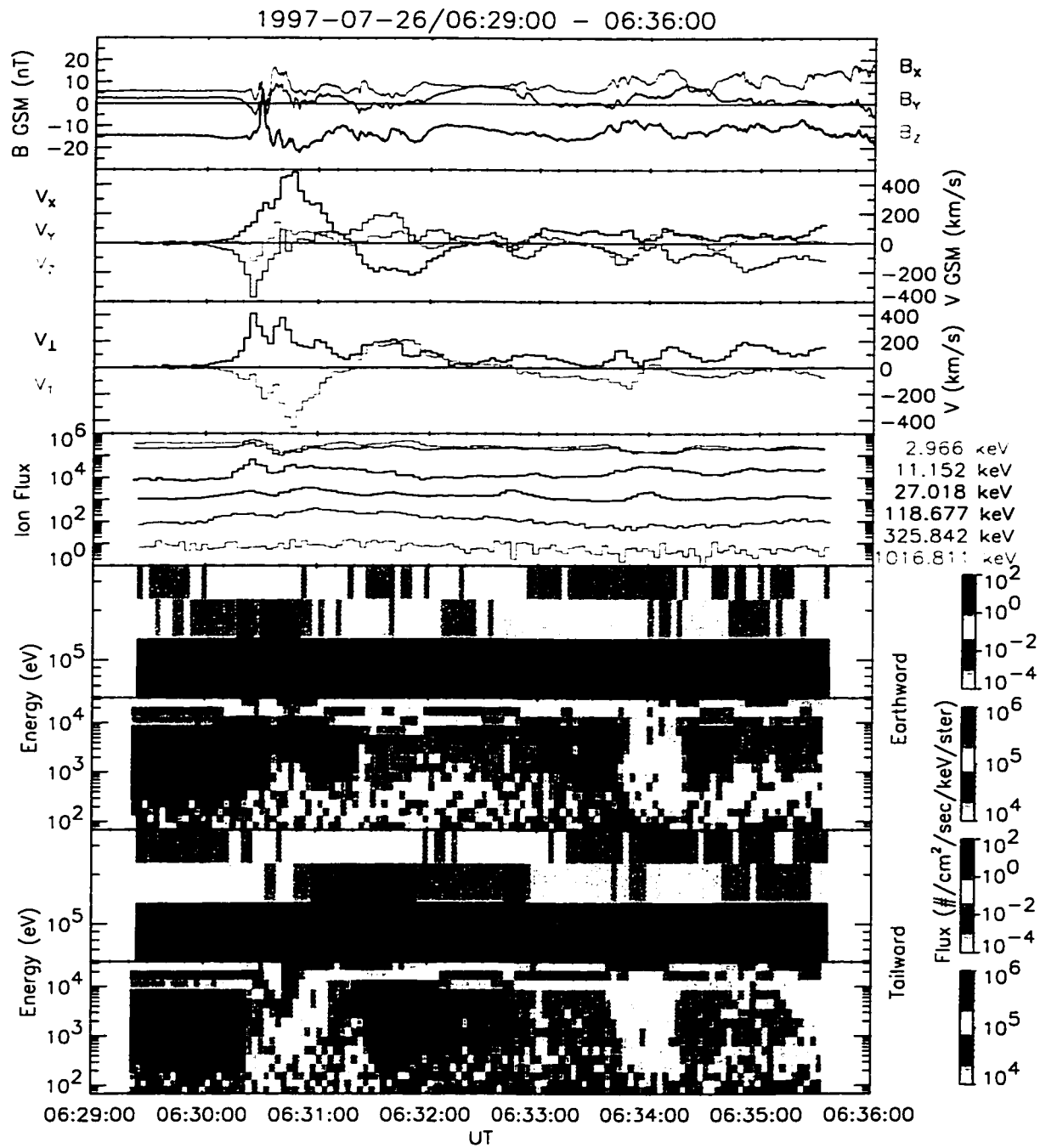
Figure 3.21: High time resolution magnetic field and ion data. From top to bottom: magnetic field; ion velocity in GSM and magnetic coordinates; omnidirectional ion flux; Earthward and tailward energy spectrograms.

3.3.2 Electron Behavior

Electron measurements from this same interval are shown in Figure 3.22. From top to bottom, this figure shows the magnetic field data, electron density, electron omnidirectional flux at three selected energies, and pitch angle spectrograms at two energies. For this mode of operation, EESA-L only measured electrons with energies up to 1 keV. EESA-H extends the energy range up to 30 keV, but EESA-H was not operating in burst mode at this time. Therefore, the omnidirectional electron flux plot and the top pitch angle spectrogram shows data for 1 keV electrons, the highest energy channel available.

By comparing the electron density with the ion density of Figure 3.20, we see that the electron density is typically a factor of two less than the ion density. This indicates that about half of the electron density is due to electrons with energies higher than 1 keV. After the large ion $\langle v \rangle$, the density discrepancy is even higher, suggesting that over half of the electron distribution is over 1 keV.

The electron omnidirectional flux plot and the pitch angle spectrograms support this conclusion. During intervals where the 1 keV flux drops, the flux at higher energies increases, showing that the spectrum becomes harder. The pitch angle spectrograms show a field aligned distribution at all energies throughout most of this interval. When the flux levels are rapidly increasing (at high energy) or decreasing (at low energy), the distributions are more isotropic.

There appears to be a lower flux anti-aligned to the magnetic field (180°) than there is along the magnetic field (0°) in the 100 keV pitch angle spectrogram. This is an artifact. During this interval, the magnetic field is pointing mostly in the tailward direction. Therefore, the anti-aligned direction is in the Earthward and Sunward direction. However, direct sunlight produces spurious counts that must be removed from the data, leaving the anti-field aligned direction undersampled.
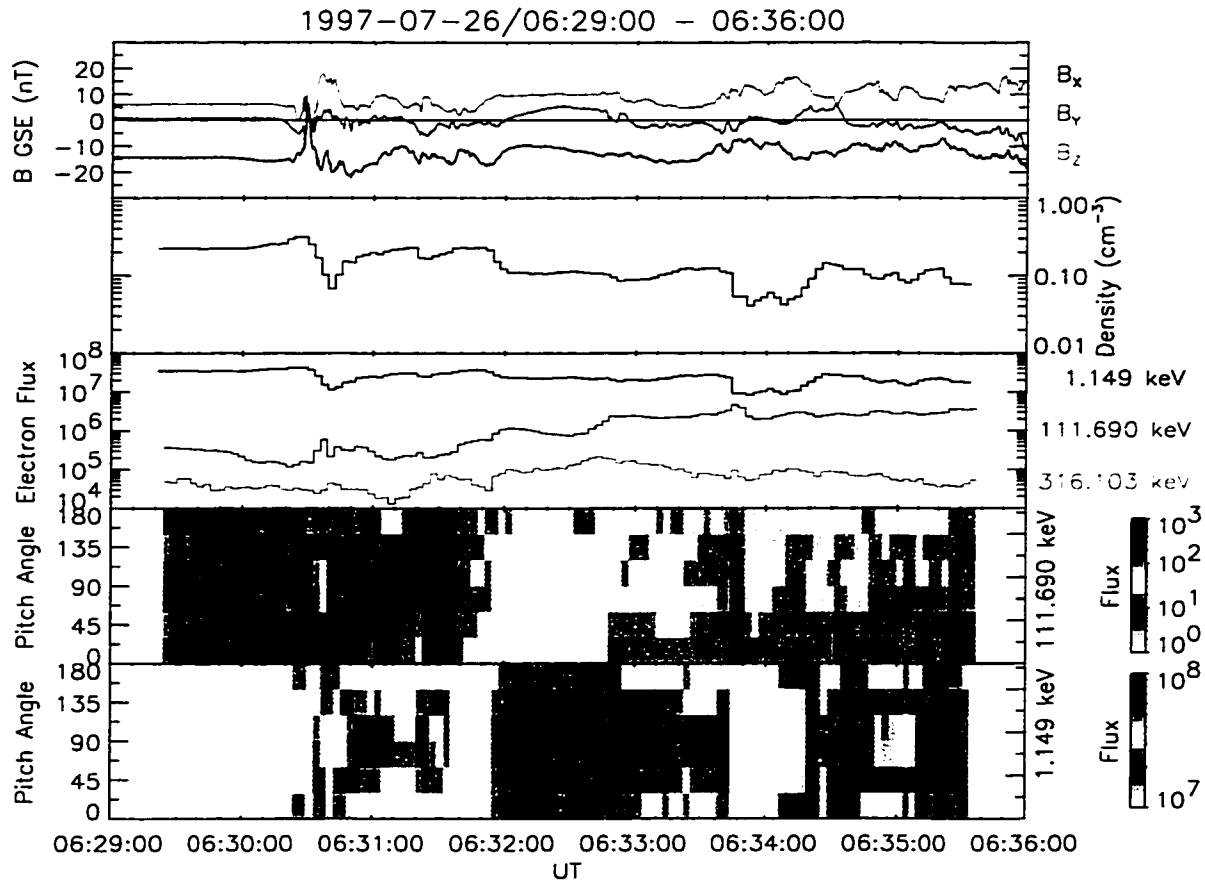
Figure 3.22: High time resolution magnetic field and electron data. From top to bottom: magnetic field; electron density; omnidirectional electron flux; pitch angle spectrograms.

3.3.3 Plasma Distribution Functions

Now we will take a closer look at the ion and electron dynamics during the large $\langle v \rangle$ event by examining the distribution functions. Ten phase space velocity distribution functions during the interval of large $\langle v \rangle$ are presented in Figure 3.23. Ten two-dimensional slices of the full three-dimensional distribution functions in the $\mathbf{B} - \mathbf{V}_\perp$ plane in the spacecraft frame of reference are shown along with one-dimensional cuts in the directions parallel (red asterisks) and perpendicular (blue diamonds) to the averaged magnetic field, similar in format to Figures 3.13 and 3.15. The second contour plot corresponds to the first peak in $\langle v \rangle$ in Figures 3.20 and 3.21.

The first distribution in this figure appears nearly isotropic in the plasma frame. There is a shift in the distribution toward the upper left quadrant resulting in a $\langle v \rangle$ of just over 200 km/s, but the contours are nearly circular and concentric. It appears as though two components are present. There is a "ledge" in the distribution near 1000 km/s. It is also apparent in the 1-D cuts as a break in the spectrum. This feature is seen in earlier distributions as well.

From the first to the second distribution, the $|\langle v \rangle|$ nearly doubles to over 400 km/s. The second distribution is much more complex and anisotropic; sharp gradients in the phase space density are present. There is an enhancement of high energy particles perpendicular to the magnetic field which gives rise to the first peak in $\langle v \rangle$ in the $-Y$-direction. A Galilean transformation of an isotropic distribution cannot reproduce the features seen here. However, the magnetic field is changing during the 3.1 second integration time, so some time aliasing may be occurring.

Notice that from the fifth to the sixth distribution, there is a large decrease in the phase space density of high energy particles in the lower right quadrant, which corresponds to particles traveling in the tailward direction. The phase space density decreases by an order of magnitude at 10 keV in this direction in one gyroperiod, about 3 seconds. A careful analysis shows that the decrease in this direction is not
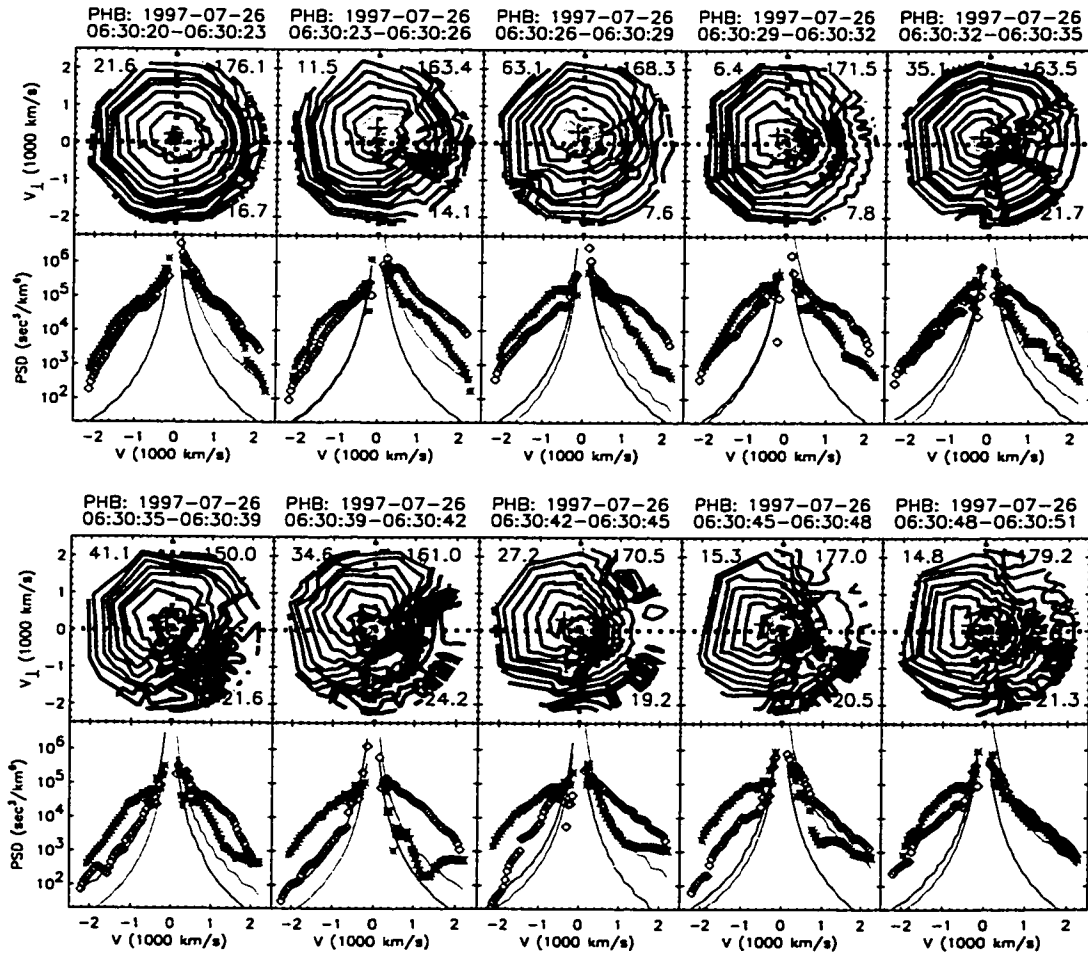
Figure 3.23: Ion distribution functions.

as extreme at higher and lower energies.

In the last five distributions, note how the direction of the enhancement in energetic particles and $\langle v \rangle$ as indicated by the plus sign changes from nearly perpendicular to **B** to nearly parallel to **B**. At the same time, the elevation angle of **B** changes from about 40° to 14° while the azimuth angle remains fairly constant. However, also note that, as shown in the second panel of Figures 3.20 and 3.21, $\langle v \rangle$ is directed almost entirely in the X-direction throughout this time interval. (The seventh, eighth, and ninth distributions represent the second, broad peak in $\langle v \rangle$ and the peak in the X-component of $\langle v \rangle$.) Therefore, the direction of $\langle v \rangle$ is not changing while the direction of **B** is changing. It appears that the ion dynamics at this point are not controlled by the local magnetic field.

The corresponding electron distribution functions are shown in Figure 3.24. The format is identical to that of the previous figure, except that these data were taken by EESA-L. The lack of a distribution between 06:30:26 and 06:30:29 UT is due to a data gap. The one-count levels in the 1-D cuts are off the bottom of the plot.

The first three distributions are relatively isotropic. There is some indication of anisotropy in the third distribution as seen in the 1-D cut. The fourth distribution is strongly anisotropic with the phase space density depleted at nearly all pitch angles. The fifth distribution is relatively isotropic, but the sixth and seventh distributions are highly anisotropic again with sharp decreases in the phase space density. In the last two contour plots, the distributions have become field aligned.

Both the ion and electron distributions are highly variable and highly dynamic even at these short time scales. We can use the fact that PESA-H and EESA-L are sweeping out 360° during each spacecraft spin to look at the ion and electron behavior with sub-spin time resolution, as shown in Figure 3.25. The top plot shows the PESA-H ion energy flux at 400 msec resolution (3.14 sec divided into 8 azimuthal sectors) at 11 keV and 1 keV (divided by 20 for clarity). The second plot shows the EESA-L electron flux at 200 msec resolution (3.14 sec divided into 16 azimuthal sectors) at
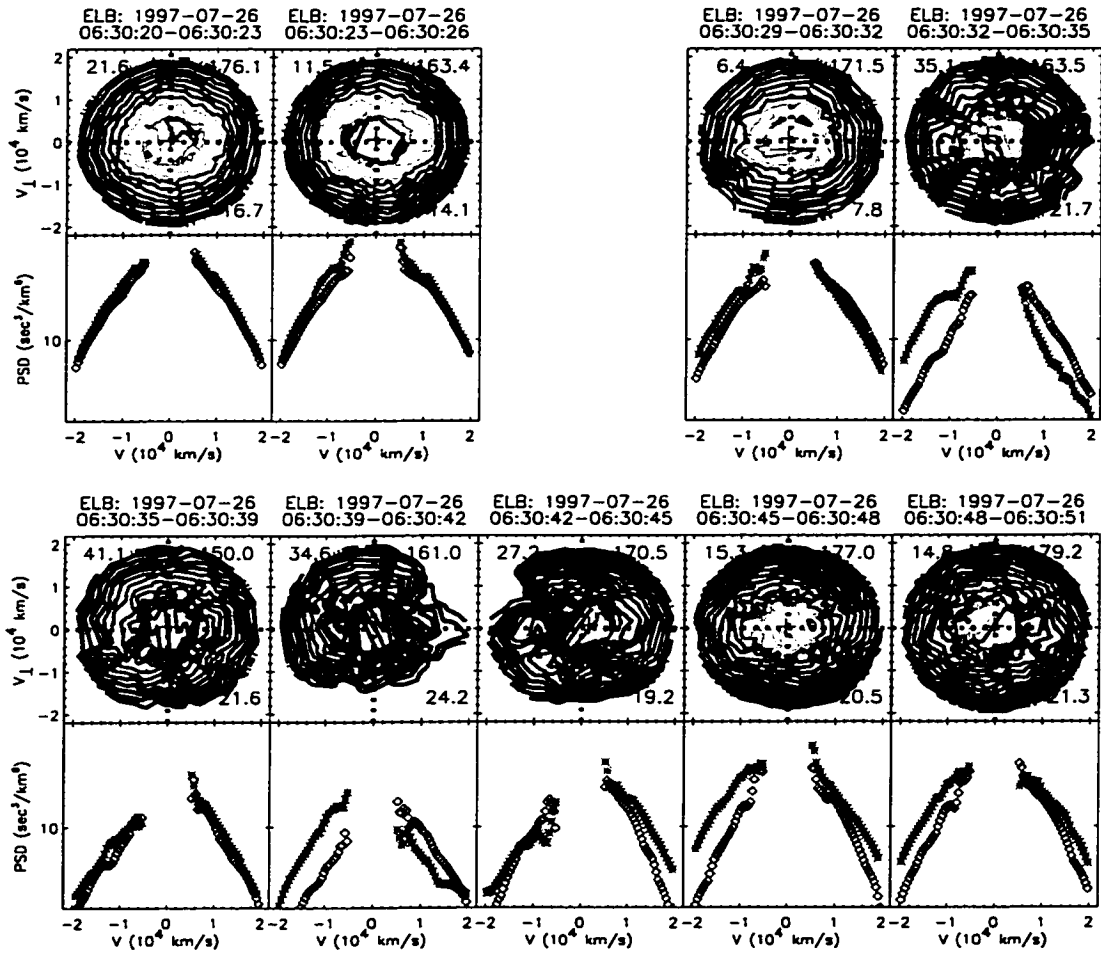
Figure 3.24: Electron distribution functions.

1 keV and 100 eV. The vertical lines through these panels delineate each 3 second sample. The bottom two plots show the magnitude, azimuth (phi), and elevation (theta) of the magnetic field at 46 msec time resolution.

At the beginning of this interval, the ion energy fluxes are anisotropic at both energies. The energy flux of 11 keV ions in the tailward direction (the envelope of the minimum values of the 11 keV ions in the ion plot) drops by an order of magnitude between 06:30:36 and 06:30:39 UT. This drop is also clearly seen by comparing the fifth and sixth distributions in Figure 3.23 The Earthward going energy fluxes (the envelope of maximum values) are slightly affected but remain above their pre-anisotropy level. The anisotropy becomes much stronger in the 11 keV ions than at 1 keV. We also see the energy flux of the 1 keV ions decreasing, reaching a minimum near the same time as the electron energy fluxes are at a minimum.

The electron energy fluxes begin relatively constant and isotropic. The electron fluxes drop sharply during the 3 second interval from 06:30:33 to 06:30:36 UT and drop even more to their minimum values 3 seconds later. These electron energy flux decreases correspond to the complex and anisotropic electron distributions seen in Figure 3.24. Based on the electron distributions shown in Figure 3.13, we suggest that these distributions are similarly time aliased, and, compared with the electron behavior shown in Figure 3.17, we predict that the electron energy flux above a few keV is increasing during the low energy electron decrease. However, we don't have any EESA-H data during this time to test this prediction. As the electron energy fluxes recover, there are two peaks per spin period in the 1 keV channel indicating a field aligned distribution.

3.3.4 Effects of Time Averaging

Finally, Figure 3.26 investigates the changes in the perceived plasma behavior as longer time integrations are considered. The horizontal scale is the same as that for Figures 3.20, 3.21, and 3.22. The dotted line in the top three panels show the

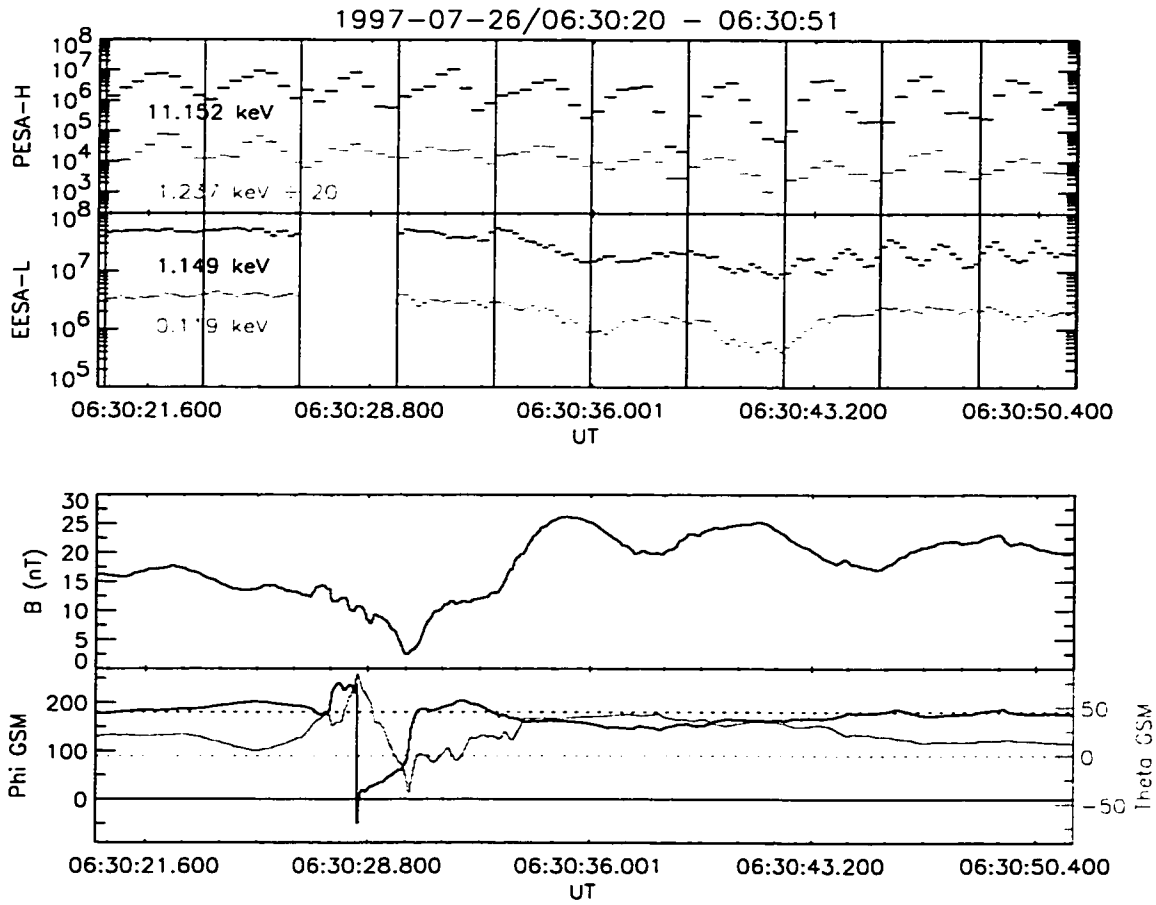Figure 3.25: Ion, electron, and magnetic field data at sub-spin resolution. From top to bottom: ion energy flux in two energy channels; electron energy flux in two energy channels; magnetic field magnitude, azimuth (phi), and elevation (theta).

46 msec resolution magnetic field in GSM coordinates. Time averaged data are shown as solid black (3.14 s), blue (25 s), and red lines (50 s). The bottom two panels of the figure show components of the ion velocity moment parallel and perpendicular to the magnetic field computed from averaged distribution functions. The corresponding magnetic field averages were similarly used.

As expected, the averaged magnetic field data miss some of the fine scale structure present in the high resolution data. There is a brief sign change of B_X near 06:30:30 UT. The sign change is missed even when averaging over 3.1 seconds. The difference between the peak value of B_X using the 0.046 second resolution and 3.1 second resolution data is nearly 12 nT. At about the same time as the B_X sign change, there are several large amplitude fluctuations in B_Y. The peak-to-peak amplitude of the largest fluctuation is about 14 nT, occurring in about 1.5 seconds. This oscillation is completely missed in the 3.1 second averages. Similar large amplitude fluctuations on second time scales are seen in B_Z as well. The peak-to-peak amplitude of these features are systematically underestimated in the longer time resolution data.

Typically, during the normal mode of operation in the magnetosphere, plasma data from 3DP is integrated over 25 (8 spacecraft rotations) or 50 seconds (16 spacecraft rotations). For the event shown here, the peak mean velocity computed from 24 second averages is 70% of the peak $|\langle v \rangle|$ computed using 3.1 second distribution functions. The peak using 50 second averages is less than 50% of that using 3.1 second data. This change of the mean arises because the distribution functions are dynamic and continuously changing on short time scales. Averaging also smears out structure present in $\langle v \rangle$; the multiple peaks seen in the perpendicular component of the velocity are replaced by a broader, smaller peak in both the 25 and 50 second averages. This leads to a different and incomplete picture of the plasma behavior during these dynamic processes.
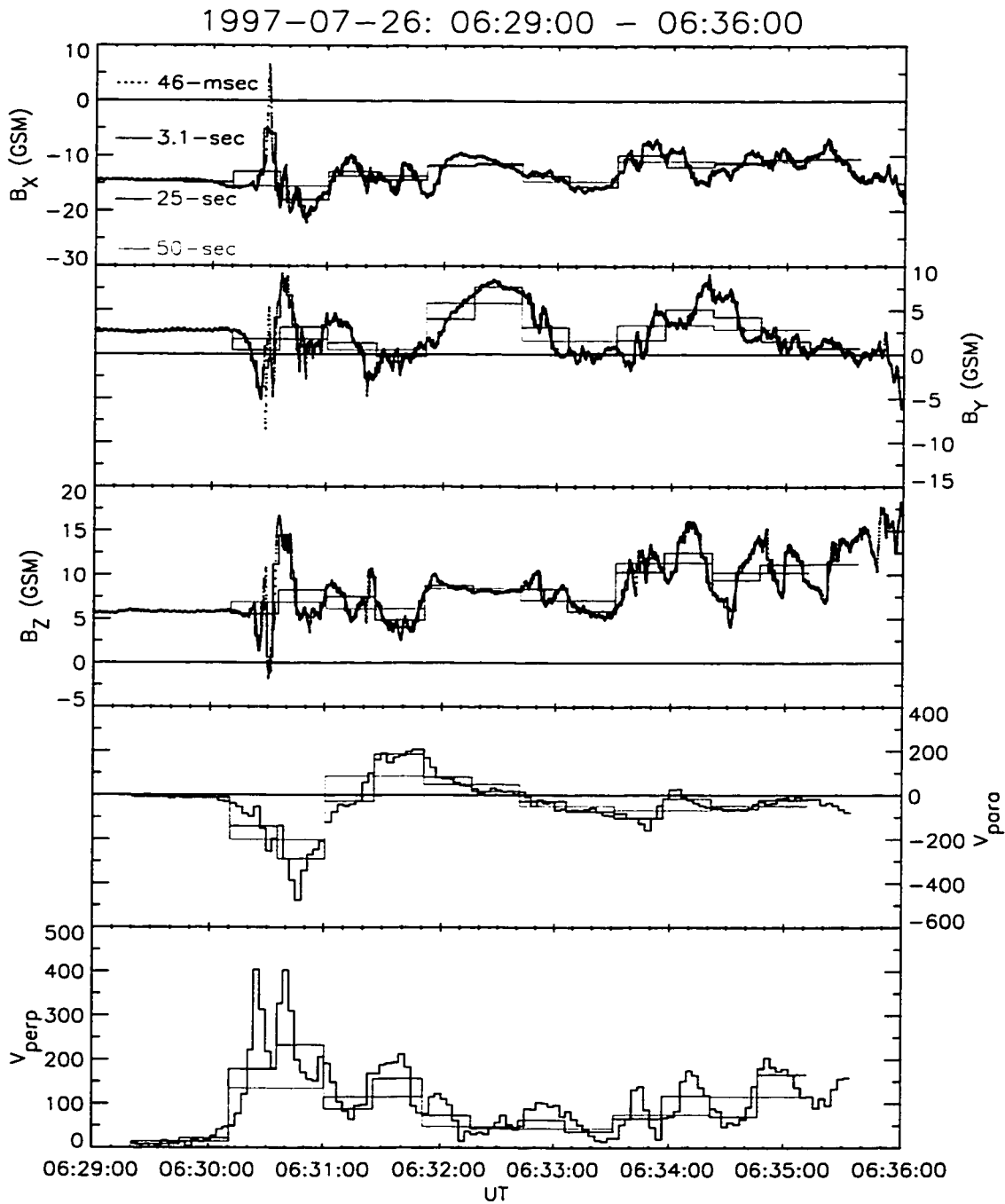
Figure 3.26: Magnetic field and ion data at varying time resolutions. From top to bottom: X, Y, and Z components of the magnetic field in GSM coordinates; parallel and perpendicular components of the ion $\langle \mathbf{v} \rangle$.

3.3.5 Summary of Observations

This section provides further evidence that the plasma sheet properties can change quite rapidly and that the ions are behaving kinetically. For example, large ion $\langle v \rangle$ can contain significant structure, that is, multiple peaks in $|\langle v \rangle|$ separated in time by a few proton gyroperiods and abrupt changes (up to 100%) in both the direction and magnitude of $\langle v \rangle$ on time scales comparable to the local proton gyroperiod.

At the same time, large amplitude, high frequency magnetic field fluctuations are seen with $|\partial B/\partial t|$ typically reaching 10 nT/s. These magnetic field fluctuations will give rise to strong, rapidly changing induced electric fields. At scale lengths on the order of the gyroradius of a 1 keV proton (several hundred km in a 10 to 20 nT field), the induced electric field strength will be on the order of 10 mV/m. This is at least an order of magnitude larger than typical expected dawn-to-dusk electric fields of a few tenths of mV/m. This is similar in magnitude to $\langle v \rangle \times B$ (500 km/s $\times$ 20 nT = 10 mV/m), which is usually interpreted as an enhanced convective electric field [*Angelopoulos et al.*, 1997]. However, the induced electric fields, rather than being quasi-static in the Y-direction for Earthward transport, are rapidly changing in direction and magnitude as B varies on time scales faster than the proton gyroperiod. These magnetic fluctuations have significant wave power present at frequencies up to and exceeding the local proton gyrofrequency and, at times, the local lower hybrid frequency.

The ion distribution functions contain complex features that include large gradients and anisotropies in phase space. These features cannot be reproduced by a superposition of several Maxwellian distributions. Significant changes also occur in these distribution functions on time scales comparable to the local proton gyroperiod indicating that the plasma is very dynamic. It is clear from the rapid fluctuations in B and from the changes in the ion distribution functions that the ions cannot be behaving adiabatically. Furthermore, the direction of $\langle v \rangle$ at times is not affected by

changes in the direction of **B**, suggesting that the ions also may not be magnetized.

The electron distribution functions also appear complex and anisotropic. However, this is most likely due to time aliasing. The electron distributions, while still behaving adiabatically, can change dramatically on time scales faster than the three second integration time.

Changing the integration time drastically changes the picture we get of the plasma dynamics. The magnitude of fast fluctuations in **B** are usually underestimated and some are completely missed when integrating over time scales longer than about 1 second. Also peaks in the ion $\langle \mathbf{v} \rangle$ are substantially lower and structure is smeared out when averaging over several proton gyroperiods. This bursty behavior of $\langle \mathbf{v} \rangle$ was similarly noted by [*Baumjohann et al.*, 1990] and [*Angelopoulos et al.*, 1992] as an increase in the peak $|\langle \mathbf{v} \rangle|$ with shorter time resolution. Peak $\langle \mathbf{v} \rangle$ are measured when the integration time is on the order of the gyroperiod. This suggests that the $\langle \mathbf{v} \rangle$ are not a bulk plasma phenomenon but are the result of kinetic processes.

Chapter 4

SUBSTORM OBSERVATIONS

In the previous chapter, we analyzed the behavior of the plasma sheet during pseudobreakups. Now we will compare those results with the plasma sheet dynamics observed during larger auroral events. By comparing the plasma sheet observations for these two different types of auroral activity, we hope to shed some light on what plasma sheet properties, if any, are different during large and small auroral events. Both of the substorm intervals shown here have features commonly seen during WIND perigee passes during auroral activity. In this regard, they can be considered two different but still "typical" substorms.

First we examine the auroral and plasma sheet behavior during several large substorms on March 27, 1996. The plasma sheet dynamics during this data have been discussed earlier from both an MHD point of view [*Angelopoulos et al.*, 1997] and from a kinetic point of view [*Chen et al.*, 2000b; *Fillingim et al.*, 2001]. We extend the analysis of the previous kinetic work and also consider the electron behavior which has been ignored.

Next we analyze another substorm interval from September 29. 1997. During this pass, WIND was again in a mode in which ion and electron distributions with a resolution of 3 seconds were transmitted. With this data we are able to compare the plasma sheet dynamics during pseudobreakups and substorms on kinetic time scales.

4.1 March 27, 1996

4.1.1 Auroral Observations

In Figure 4.1, we show a sequences of images taken by UVI on March 27, 1996. The integration time for each image is about 37 seconds. The time between images is about 5 minutes, except between the third and fourth images, between which there is a nearly 20 minute gap. The ionospheric footprint of the Wind spacecraft is marked on each image. At 14:30 UT on March 27, 1996, Wind was located in the plasma sheet at a GSM position of $[-15, 7, 1]$ R_E.
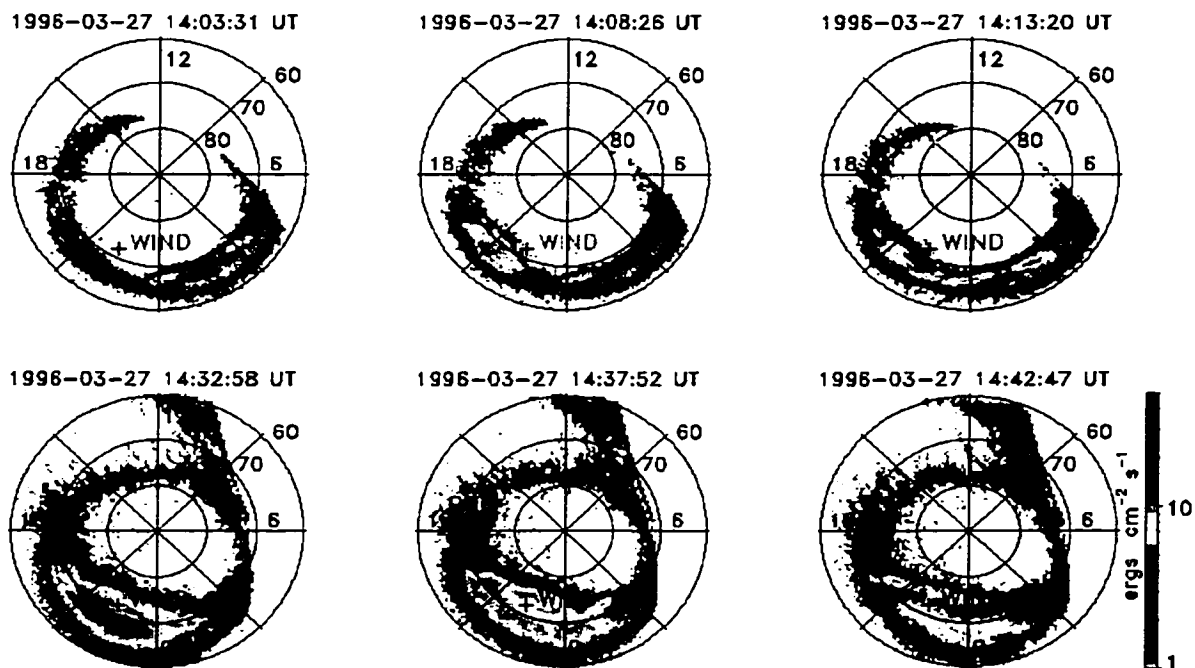

Figure 4.1: A sequence of UVI images from March 27, 1996, showing a substorm expansion. The magnetic footprint of WIND is also shown.

Compare these images with the images taken on July 26, 1997 (Figure 3.1). The

auroral brightening begins in a localized area, but the region of intense electron precipitation expands globally in latitude and longitude and persists for nearly an hour in contrast to the short localized brightenings shown in Figure 3.1.

4.1.2   Ion Observations

Figure 4.2 shows a summary of the auroral activity measured by UVI and of the magnetic field and plasma behavior measured in the plasma sheet by WIND covering 7 hours on March 27, 1996. The first three panels, the keogram, the local time extent of the aurora, and the energy deposition rate, summarize the auroral activity for this day. The fourth panel shows the plasma sheet magnetic field at 3 second resolution. The bottom four panels show the ion moments computed from the 3-D ion distribution function: density, velocity in GSM and magnetic field aligned coordinates, and temperature in GSM coordinates at 25 or 50 second resolution, depending upon the instrument mode.

The top three panels should be compared to Figure 4.2. Note that the spatial extent of the intense auroral emission is much greater on this day. At its greatest extend, the active aurora covers over 20 degrees in latitude and nearly the entire nightside hemisphere. The energy deposition rate in the ionosphere is more than double the peak seen during pseudobreakups. Also, since the energy deposition rate is only integrated over the midnight quadrant from 18 to 06 MLT, the actual energy deposition rate into the ionosphere is larger than this value. Since WIND is at a larger radial distance during this day (15 R_E as opposed to 11 R_E on July 26, 1997, its footprint maps to a higher latitude. Typically the WIND footprint is poleward of the auroral emission except during periods of large expansion. The large jump in latitude in the keogram and the jump in the energy deposition rate curve near 14:30 UT is not real but is the result of a 20 minute data gap in the UVI data.

The magnetic field appears highly variable throughout this period. Large amplitude, high frequency fluctuations are usually present when WIND maps to the region
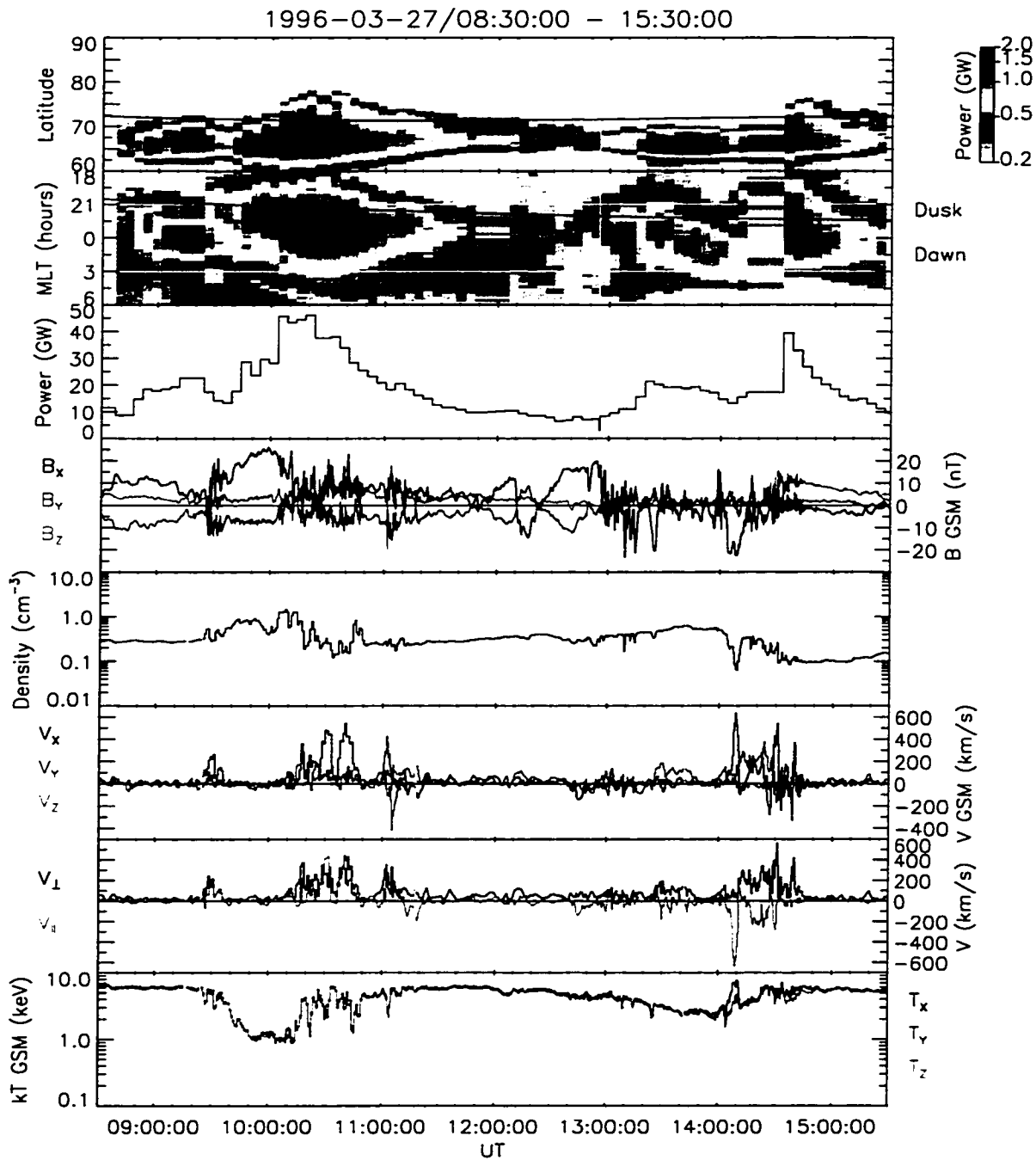
Figure 4.2: Comparison of auroral imagery data with plasma sheet magnetic field data and ion moments. From top to bottom: latitude and local time keograms; auroral power; magnetic field; ion moments (density, velocity, and temperature).

of intense aurora: from 10:00 through 11:00 UT and again near 14:30 UT. However, large magnetic field fluctuations are seen at other times as well. There are also several large, low frequency magnetic field variation present in the data. Between 12 and 13 UT, the X-component of the magnetic field rapidly changes from positive to negative and then gradually back to positive again indicating two crossings of the current sheet. There are several more large amplitude B_X sign changes between 13 and 14:30 UT.

There are several large ion velocity moment events present during this interval as well, mostly directed Earthward. There are also a few events with a large positive or negative Y-component. Nearly every large $\langle v \rangle$ is associated with large magnetic fluctuations, with the sole exception occurring at 14:10 UT. Also nearly every large $\langle v \rangle$ occurs when WIND maps to the region of intense aurora. Exceptions occur near 09:30 and at 14:30 UT. During the 09:30 UT $\langle v \rangle$ event, the magnetic field is rapidly fluctuating and auroral activity is present in the same local time sector as WIND, but WIND maps poleward of the auroral emission.

The seventh panel shows that the components of the velocity parallel and perpendicular to the magnetic field are usually roughly equal during the large $\langle v \rangle$ events. Again the sole exception occurs at 14:10 UT, where the velocity is almost entirely directed parallel to the magnetic field. Also during this event, the magnetic field is strong (~ 20 nT), dominated by the X-component, and not fluctuating. Based on these facts, and analysis of the ion distribution functions, we have concluded that the large $\langle v \rangle$ at 14:10 UT is a field aligned beam in the plasma sheet boundary layer (PSBL) and is not present in the plasma sheet proper.

Again, similar to July 26, 1997, the density and temperature appear roughly anti-correlated. Although there does not appear to be a clear correlation between the density, temperature, and $\langle v \rangle$, when $\langle v \rangle$ is large and the magnetic field is rapidly fluctuating, there are significant variations in the density and temperature. This is especially apparent between 10 and 11 UT.

Following the same procedure as Chapter 3, we now look at the ion behavior in more detail. Figure 4.3 again shows the keogram, magnetic field, and ion $\langle v \rangle$ as was show in the previous figure. The fourth panel shows the ion omnidirectional flux at six selected energies. The bottom four panels show the Earthward and tailward ion energy spectrograms for energies from 70 eV up to greater than 1 MeV.

Figure 4.3 can be directly compared to Figure 3.6. Again during intervals of large $\langle v \rangle$, the energetic ion flux increases up to MeV energies. The largest increases occur just after 10:00 UT and again near 14:30 UT. There is an increase in the energetic ion flux near 13:20 UT that is not associated with a large $\langle v \rangle$ event. The energetic ion fluxes increase in both directions during large $\langle v \rangle$, but anisotropies in the Earthward direction are present. Note that during the two large $\langle v \rangle$ near 10:30 and 10:40 UT, as the medium energy (1 to 10 keV) fluxes are anisotropic in the Earthward direction, the fluxes below a few hundred eV appear anisotropic in the tailward direction. Fluxes below 1 keV are generally relatively isotropic. Finally, after 14:30 UT, while auroral activity is continuing, the flux of low energy ions below 100 eV increases and is mainly in the tailward direction.

4.1.3   Electron Observations

The electron behavior on March 27, 1996, is also quite similar to that observed on July 26, 1997. Figure 4.4 illustrates the electron behavior during March 27, 1996, in the identical format as Figure 3.7.

When WIND maps to the region of intense auroral emission, the electron temperature increases and can be quite variable. At the same time, the energetic electron fluxes increase. Near 10:30 UT the lower energy electron fluxes also increase as the energetic electron fluxes increase, but after 14:30 UT the electron fluxes at energies below a few keV decrease as the more energetic electron fluxes increase. The latter behavior is what was typically observed on July 26, 1997. As was noticed in the ion fluxes, near 13 UT there is an increase in the most energetic electron fluxes that

Figure 4.3: Comparison of auroral imagery data with plasma sheet magnetic field and ion data. From top to bottom: keogram; magnetic field; ion velocity; ion omnidirectional flux; ion energy spectrograms.
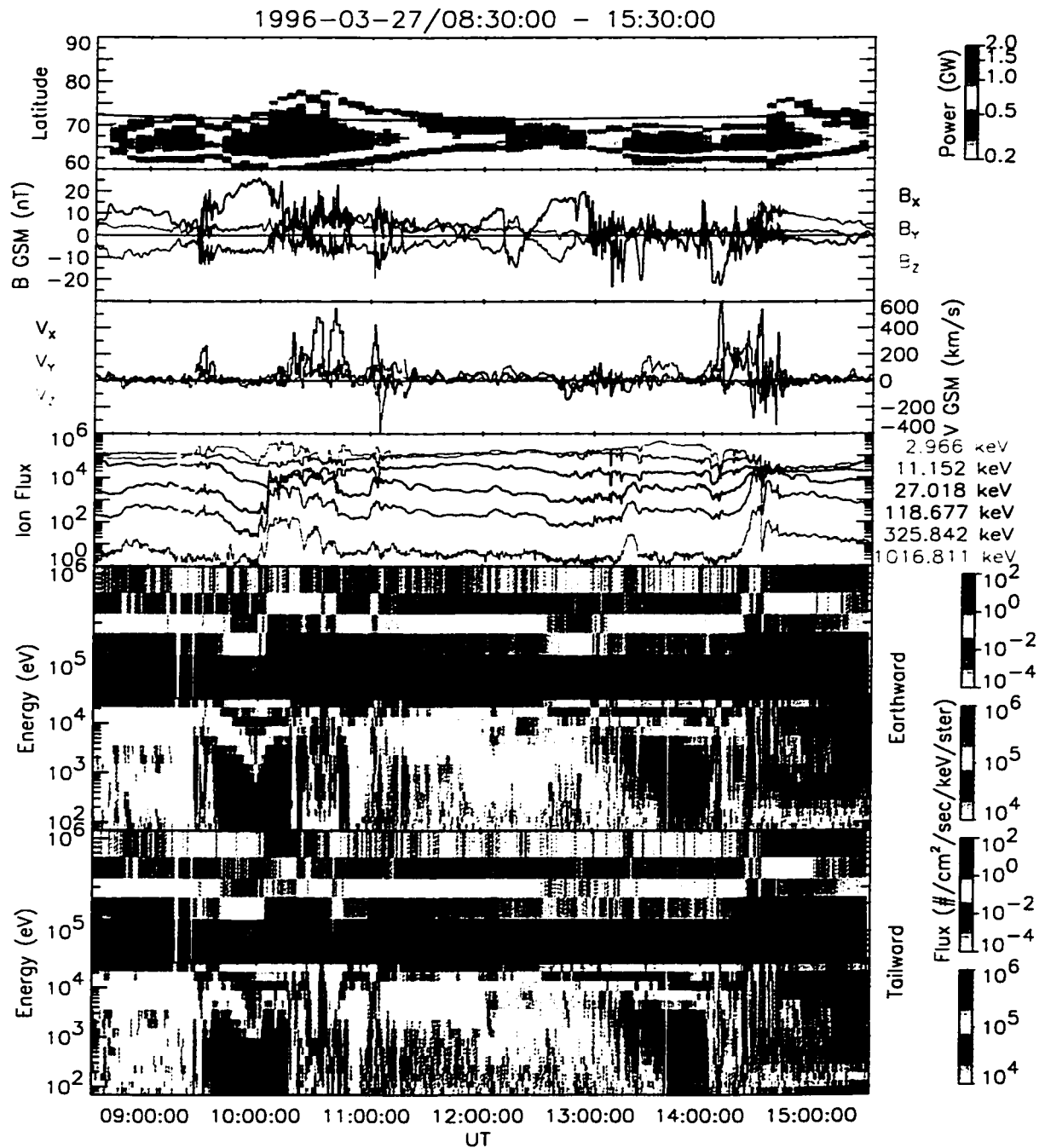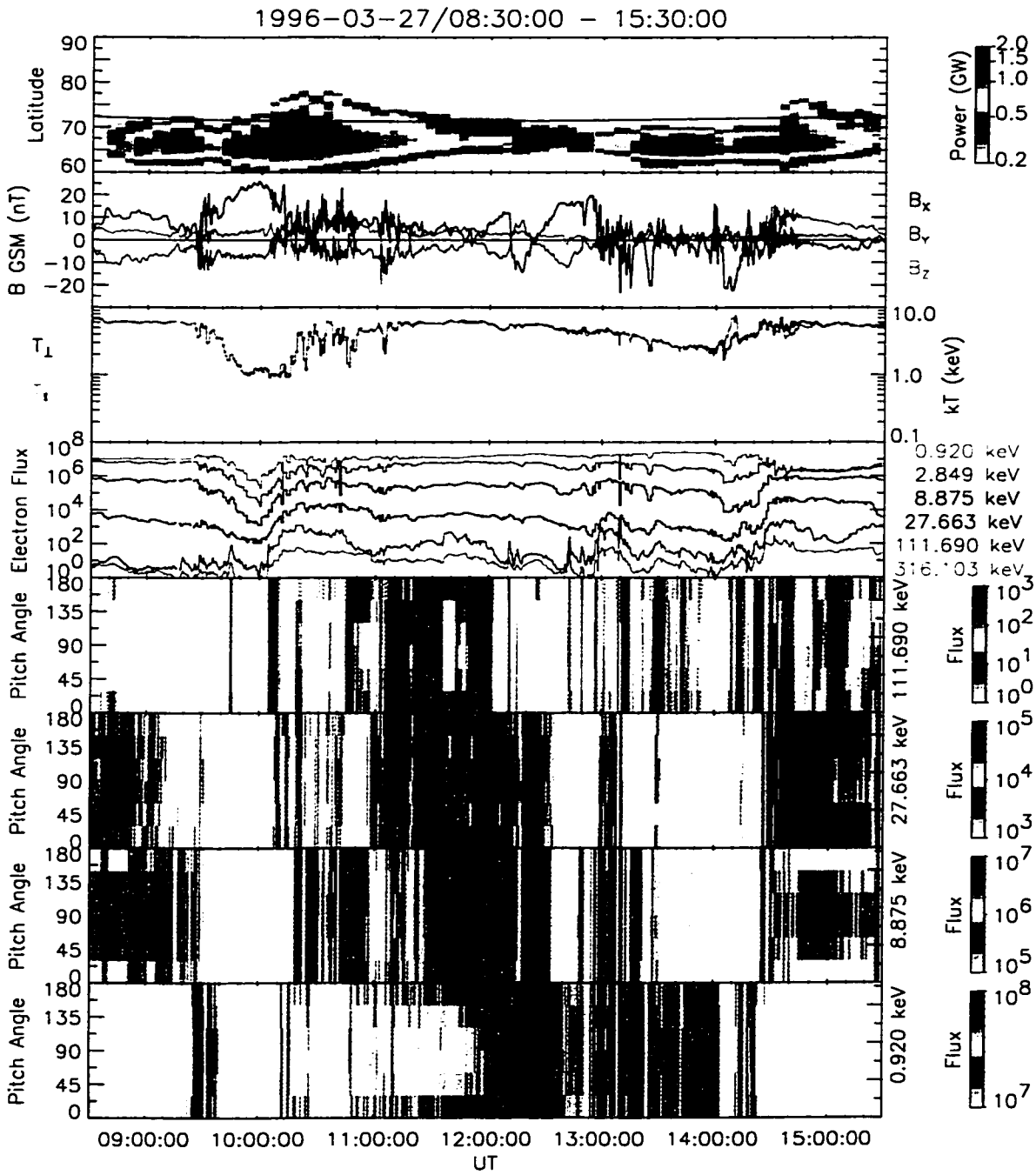
Figure 4.4: Comparison of auroral imagery data with plasma sheet magnetic field and electron data. From top to bottom: keogram; magnetic field; electron temperature; electron omnidirectional flux; electron pitch angle spectrograms.

occurs when WIND does not appear connected to the region of auroral activity in the ionosphere. The electron distributions appear mostly field aligned throughout this time period.

4.1.4 Plasma Distribution Functions and Spectra

In order to compare specific phase space features in the plasma sheet during pseudo-breakups and substorms, we examine the ion distribution functions. Figure 4.5 and 4.7 shows isocontour plots of phase space densities and cuts of the isocontour plots for some representative ion distribution functions. These figures are identical in format to Figures 3.13 and 3.15. Figure 4.5 covers the time interval from 10:30 to 10:35 UT. In contrast to data from July 26, 1997, there is one three-second electron distribution for every ion distribution. This figure shows the ion and electrons distributions during and after the large $\langle v \rangle$ at 10:30 UT.

The first four ion distributions are very similar. They each contain a broad beam directed parallel to the magnetic field at a velocity of nearly 1000 km/s, or about 5 keV. There is also a population of anisotropic low energy ions that is slightly shifted in the anti-parallel direction and elongated in the perpendicular direction. Both the core and the beam population are displaced from the origin by a few hundred km/s, indicating that the plasma was being convected by an electric field based on its velocity independent nature. The resulting $\langle v \rangle$, as indicated by the small cross, is partly in the perpendicular direction due to the $\mathbf{E} \times \mathbf{B}$ drift and partly in the parallel direction due to the parallel beam, but the parallel velocity is less than the beam velocity due to the presence of the low energy population. In the fifth ion distribution, the beam is no longer present. The low energy component also appears to have diminished. The distribution no longer contains sharp gradients and large anisotropies, though there is a slight anisotropy in the energetic ions in the perpendicular direction leading to a $\langle v \rangle$ of about 100 km/s.

The first four electron distributions also appear similar to each other. All four

Figure 4.5: Ion and electron distribution functions covering the time interval 10:30:53 to 10:34:14 UT. The magnetic field is plotted for comparison.
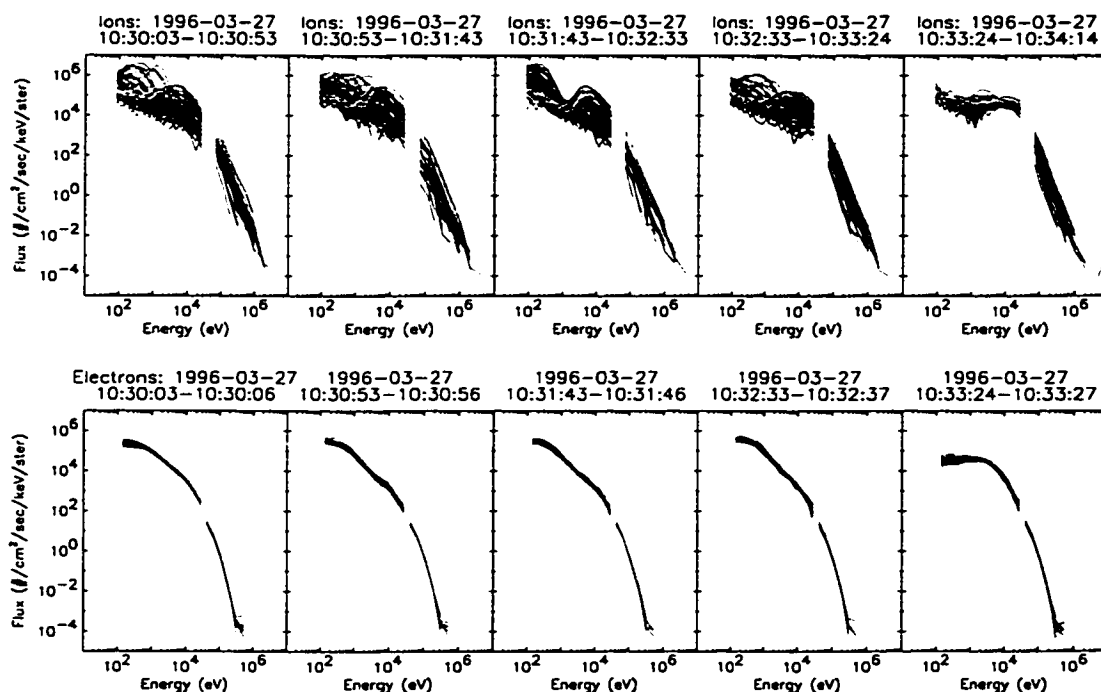
Figure 4.6: Ion and electron differential energy spectra covering the time interval 10:30:53 to 10:34:14 UT.

appear isotropic at all energies The distributions seem to be composed of two components with a break in the spectrum around 40,000 km/s ($\sim$ 4 keV). The last electron distribution shows a dramatic change in the electron populations. The high energy component is relatively unchanged, but there is now only a very weak low energy component at energies below 1 keV.

In Figure 4.6 we again show the ion and electron differential energy spectra for these distributions. The format of this figure is the same as Figure 3.14 and 3.16. The only difference is that the SST electron fluxes are integrated over 6 seconds rather than 12 seconds as on July 26, 1997.

The ion distributions are highly anisotropic. From a few keV up to MeV energies, the fluxes are peaked in the Earthward direction and are minimum in the tailward

direction. These anisotropies are due to the large parallel beam. At lower energies, the ion distributions are peaked in the intermediate directions (green curves). In the fifth ion spectrum plot, the anisotropy is not as large, but it still extends to the highest energy channels of the detectors.

The electron spectra clearly show a two component distribution with a break in the spectrum around a few keV for the first four panels. The low energy electron flux is enhanced relative to that observed during periods of plasma sheet activity on July 26, 1997. The flux of low energy electrons drops in the fifth panel, at the same time as the low energy ion population disappears. Both the ion and electron spectra are relatively flat out to 30 keV and 5 keV, respectively, in the fifth column. These spectra are very similar to those seen on July 26, 1997.

Figure 4.7 shows the distribution functions for the large $\langle v \rangle$ event near 14:30 UT. During this event, the ion data had a time resolution of 25 seconds while the electron distributions have a time resolution of 3 seconds but are sampled only once every 50 seconds.

The second and third ion distributions in this plot contain an extremely energetic component in the positive perpendicular $((\mathbf{B} \times \mathbf{V}) \times \mathbf{B})$ direction and steep phase space density gradients. The 1-D cuts of these two distributions show a plateau which extends off the scale (> 30 keV). The energy spectrograms (Figure 4.3) show that the increase in ion flux (not the plateau, per se) extends to several MeV. In the fourth and fifth ion distributions in Figure 4.6, the high energy plateau is gone and the large anisotropy in the phase space density is no longer present.

The first electron distribution appears isotropic. The second electron distribution, measured during the large perpendicular anisotropy in the ions, is field aligned at energies below about 4 keV ($\sim 40,000$ km/s) and is peaked in the perpendicular direction at higher energies. In the third electron plot, the distribution is field aligned at all energies with the lower energies (below about 10 keV) being more strongly peaked in the field aligned direction.
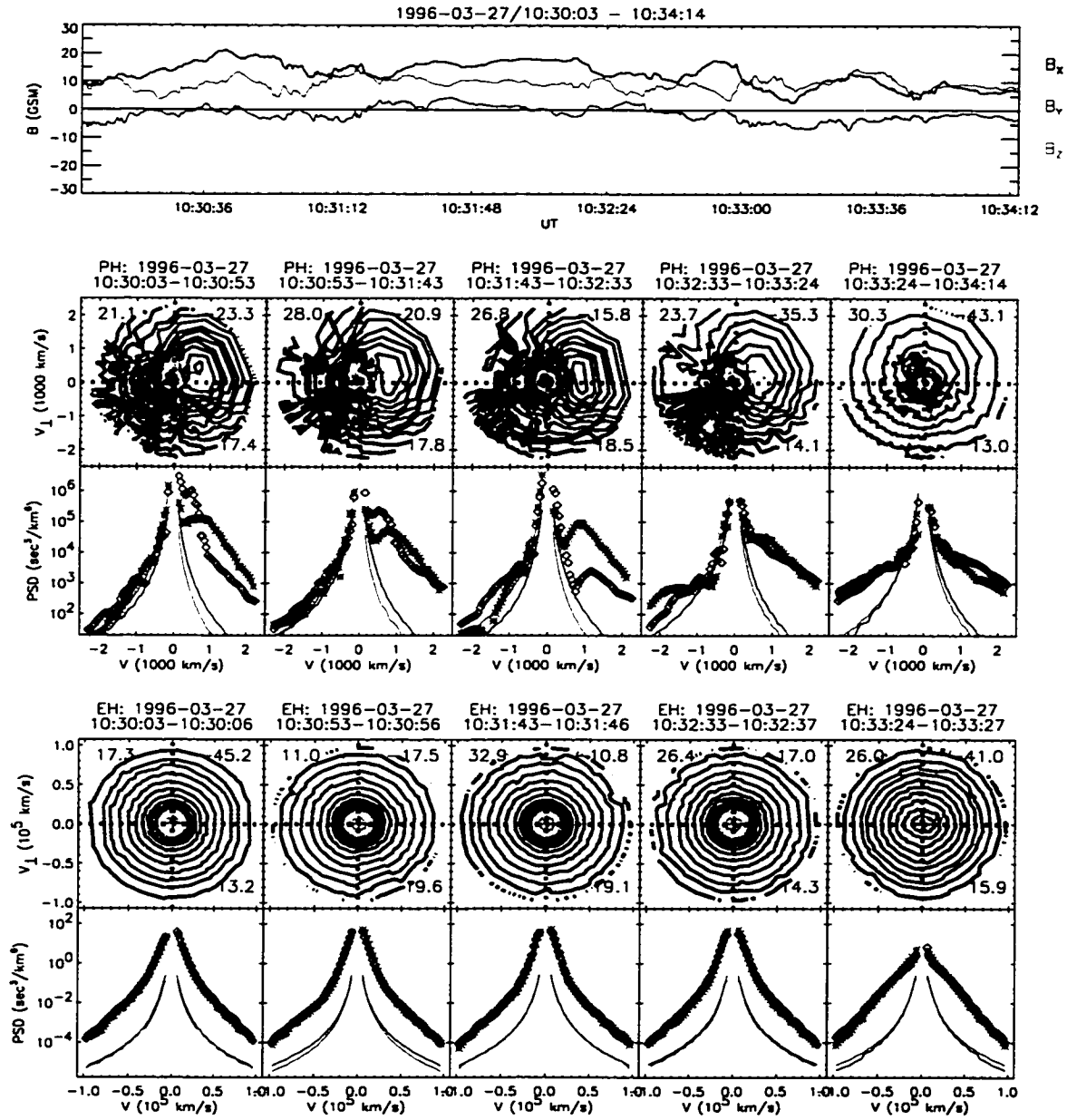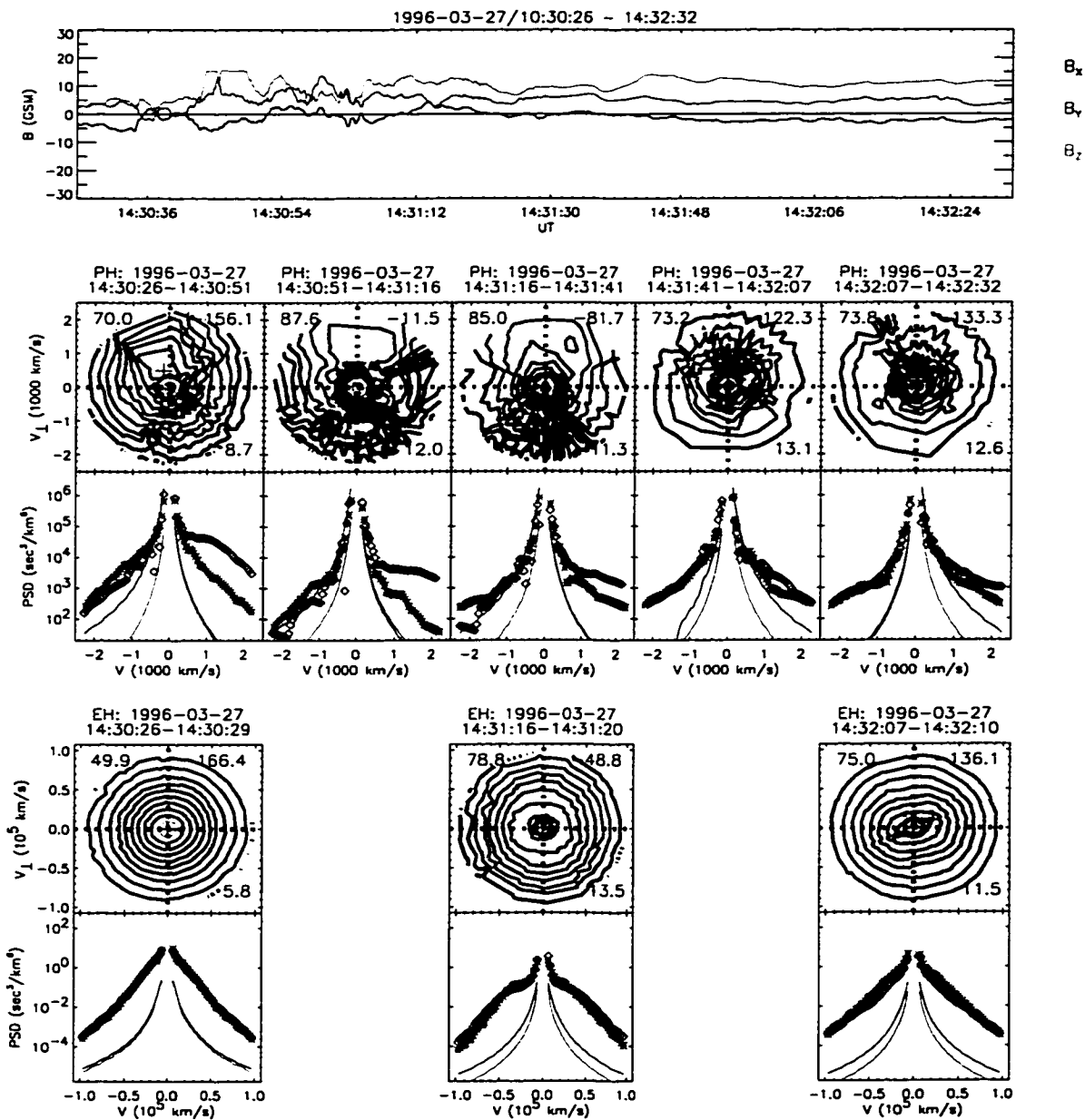
Figure 4.7: Ion and electron distribution functions covering the time interval 14:30:26 to 14:32:32 UT. The magnetic field is plotted for comparison.

The magnetic field, shown in high resolution in the top plot of Figures 4.5 and 4.5, is variable throughout both intervals, though the amplitudes of the fluctuations are not as large as those seen on July 26, 1997. In both Figures 4.7 and 3.15, B_X is near zero, indicating that the spacecraft is in the vicinity of the current sheet.

Finally, the energy spectra are shown in Figure 4.8. Again, the ion fluxes are high anisotropic with Earthward fluxes greater than tailward fluxes up to the highest energy channels of the SSTs. Note that in the second and third panels, the peak of the spectra lie at (or above) the high end of the energy detection threshold (30 keV) of PESA-H. This incomplete sampling of the ion population indicates that the velocity moments calculated from the distribution functions under represent the actual values of the real population.
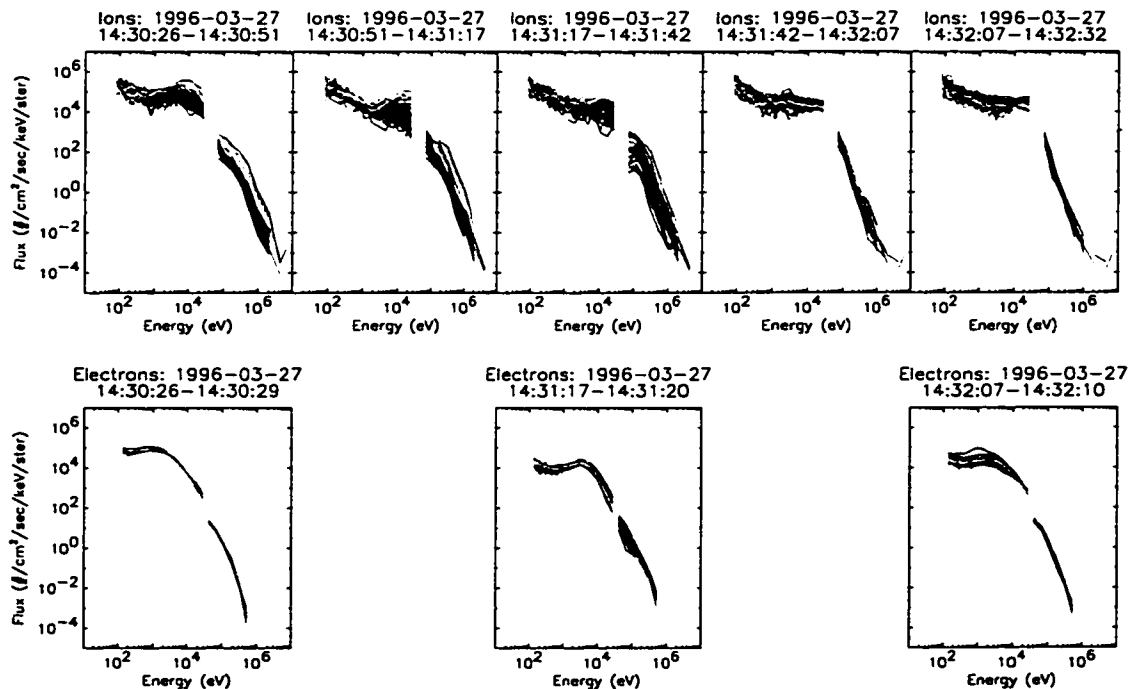

Figure 4.8: Ion and electron differential energy spectra covering the time interval 14:30:26 to 14:32:32 UT.

There appears to be an energization of the high energy electron component as the peak in the spectra move to higher energies between the first and second electron plots. The pitch angle distribution appears very complex in the second electron plot. Below several keV, the distribution is field aligned. Between several keV and about 100 keV, the distribution is peaked perpendicular the the magnetic field; above 100 keV, the distribution appears isotropic. The last electron spectrum plot indicates that bi-directional, field aligned and anti-aligned electron beams are present at energies below a few keV. The presence of these beams suggests that the field aligned distributions, as seen in the pitch angle spectrograms, may be due to narrow, intense field aligned beams.

4.1.5 Summary of Observations and Comparison to Pseudobreakups

This section shows that the plasma sheet dynamics during large substorms appears very similar to that observed in the previous chapter during pseudobreakups. When WIND maps to the region of intense auroral emission in the ionosphere, magnetic fluctuations, large ion $\langle v \rangle$, and increases in the fluxes of energetic ions and electrons are observed. The particle distribution functions observed during large $\langle v \rangle$ events during substorms contain many of the same features seen during pseudobreakups, including multiple components, strong gradients in the phase space density, field aligned beams (Figure 4.5 and Figure 3.13), and anisotropic plateaus extending to high energy (Figure 4.7 and Figure 3.15). These similarities suggest that the processes occurring in the plasma sheet during substorms are the same as those occurring during pseudobreakups.

The similarity of the plasma sheet dynamics is in contrast to the difference in the auroral activity for these intervals. The only apparent difference between these events is the size of the region of intense auroral emission in the ionosphere. The similarities in the plasma sheet behavior during both large and small auroral events suggests that the underlying plasma sheet processes are the same.

In the previous chapter, we saw that the plasma sheet disturbances occurred at the same time as the aurora brightening, implying a temporal relationship between the plasma sheet and aurora. Here we see that the plasma sheet disturbances are observed when WIND maps to the region of intense aurora, not when the aurora brightens. This shows that a spatial relationship exists as well and suggests that only limited regions of the plasma sheet are disturbed during auroral activity. This complex spatial and temporal dependence may help explain why a clear correlation between auroral activity and plasma sheet disturbances has not been seen earlier.

The conclusions of this section are based on particle distributions integrated over 25 or 50 seconds. The proton gyroperiod in the plasma sheet is typically on the order of 5 seconds. Therefore, these observations only give us an average picture of the ion dynamics. In the next section, we will analyze high resolution (3-second) ion and electron data. We will then be able to compare the plasma behavior observed on kinetic time scales during substorms to that during pseudobreakups.

4.2   September 30, 1997

4.2.1   Auroral Observations

Figure 4.9 shows a sequences of images taken by UVI on September 30, 1997. Similar to the images in the previous section, each image is integrated over 37 seconds. The time between images is about 5 minutes. The ionospheric footprint of the Wind spacecraft is marked on each image. At 4:00 UT on September 30, 1997, Wind was located in the plasma sheet at a GSM position of about $[-14, 5, -2]$ R_E.

A large portion of the auroral oval is outside the UVI field-of-view. During this time, POLAR was in the ascending phase of its orbit and only started imaging the aurora at 3:53 UT. Even though UVI's field-of-view is limited, it is clear that intense aurora covers a large part of the ionosphere, similar to the images shown in Figure 4.1 from March 16, 1997, and in contrast to the images from July 26, 1997, shown in
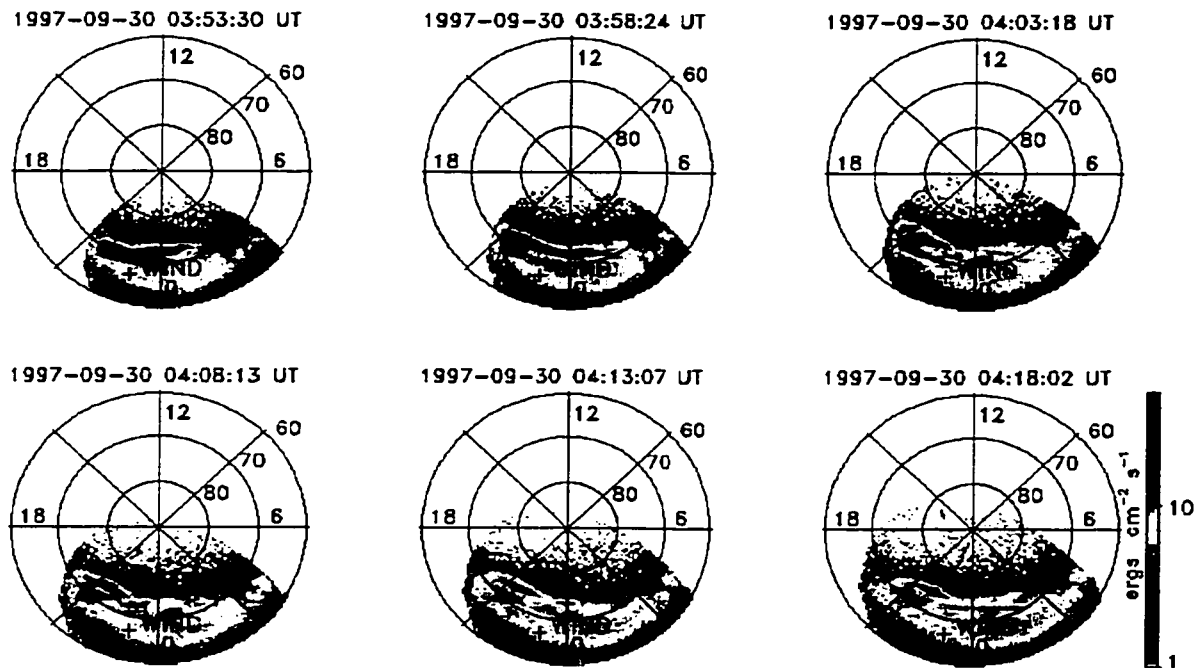
Figure 4.9: A sequence of UVI images from September 30, 1997, showing a substorm expansion. The magnetic footprint of WIND is also shown.

Figure 3.1. WIND maps to the region of intense emission but is equatorward of the most intense emission in these images.

4.2.2 Overview of Plasma Sheet Dynamics

The first three panels of Figure 4.10 clearly show that a substorm is underway as UVI starts imaging the aurora. The region of intense emission is still expanding in latitude and local time. After about an hour or so, the auroral intensity begins to decrease and the region of intense emission decreases. Activity continues for some time at the poleward edge of the aurora.

The remaining five panels of Figure 4.10 show the plasma sheet magnetic field
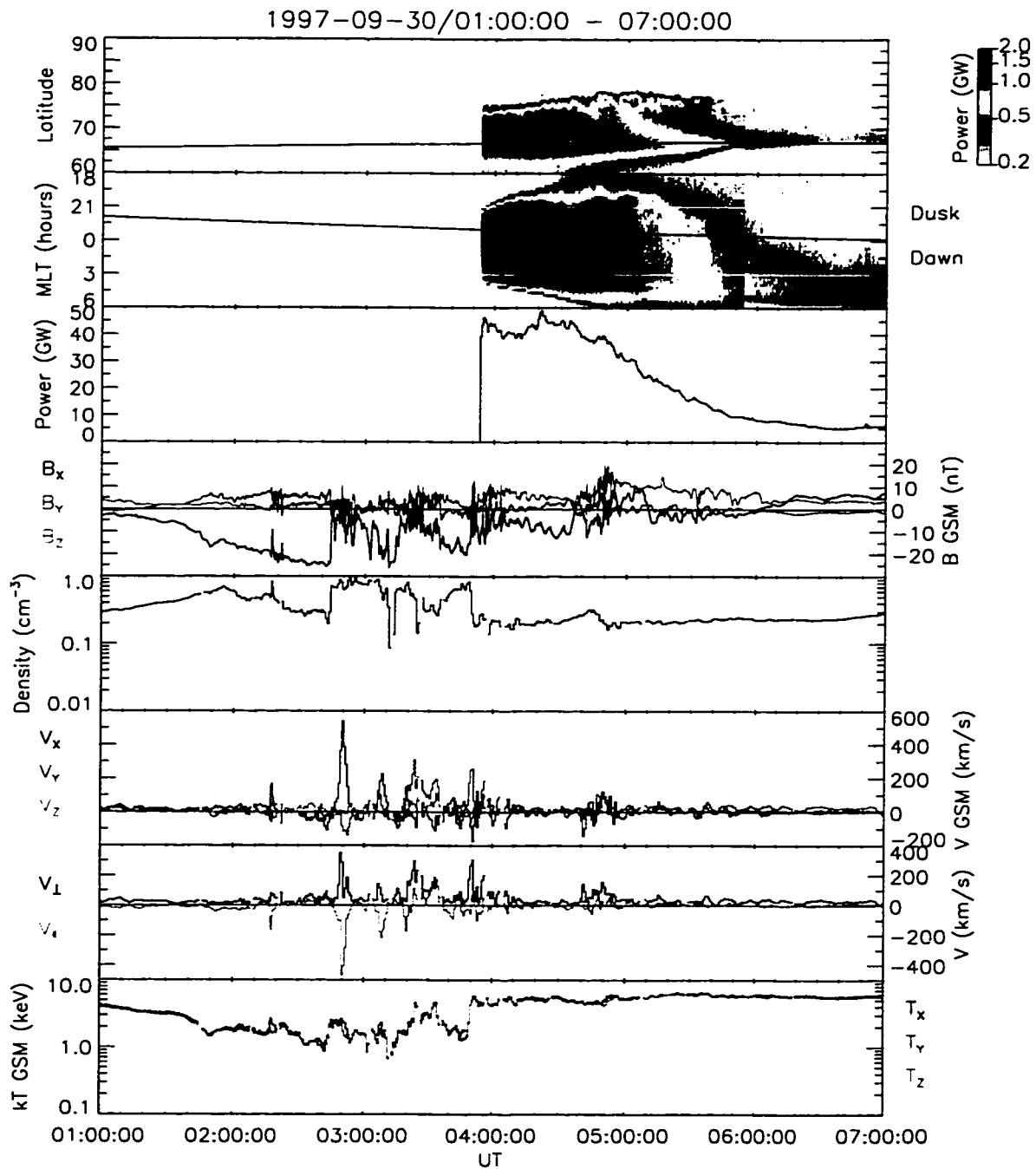
Figure 4.10: Comparison of auroral imagery data with plasma sheet magnetic field data and ion moments. From top to bottom: latitude and local time keograms; auroral power; magnetic field; ion moments (density, velocity, and temperature).

and ion moments, identical in format to Figure 4.2. Based on the plasma sheet behavior and what we have learned from the previous chapters and sections, we predict that substorm onset or a pseudobreakup occurred near 02:20 UT, and that poleward expansion of the aurora began no later than 02:45 UT, coincident with the large magnetic field fluctuations and large ion $\langle v \rangle$ seen at WIND. Ground based magnetometers located in the Canadian sector (local midnight near 6 UT) show a small deflection near 3:20 UT and a larger deflection around 3:50 UT. These may be related to magnetic fluctuations observed at WIND at about the same times. Magnetometers in the Scandinavian sector also show evidence for activity just after 3 UT and again just before 4 UT. Neither set of observations indicate activity before this time.

As seen in the previous examples, every large ion $\langle v \rangle$ is associated with large magnetic field fluctuations. The large ion $\langle v \rangle$ are generally directed Earthward, though there can be a significant positive or negative Y-component or $-X$-component. In general, the density decreases and the temperature increases during intervals of large ion $\langle v \rangle$. However, density increases are associated with the first two $\langle v \rangle$ in this case.

4.2.3 Ion Observations on Kinetic Time Scales

For the remainder of this section, we will focus on the large ion $\langle v \rangle$ that occurs just before 04 UT. During this event, 3DP was measuring the ion and electron distributions with 3-second resolution. These observations allow us to compare the behavior of the plasma during pseudobreakups and substorms on kinetic time scales

Figure 4.11 shows the ion moments with 3-second resolution, the magnetic field with 46-millisecond resolution, the time derivative of the magnitude of the magnetic field, and the dynamic frequency spectrogram.

There is some interesting behavior seen in the ion moments. At the beginning of this interval, the ion $\langle v \rangle$ is already elevated (> 100 km/s), pointed mostly in the Y-direction, and gradually increasing. The density and temperature, which are anti-
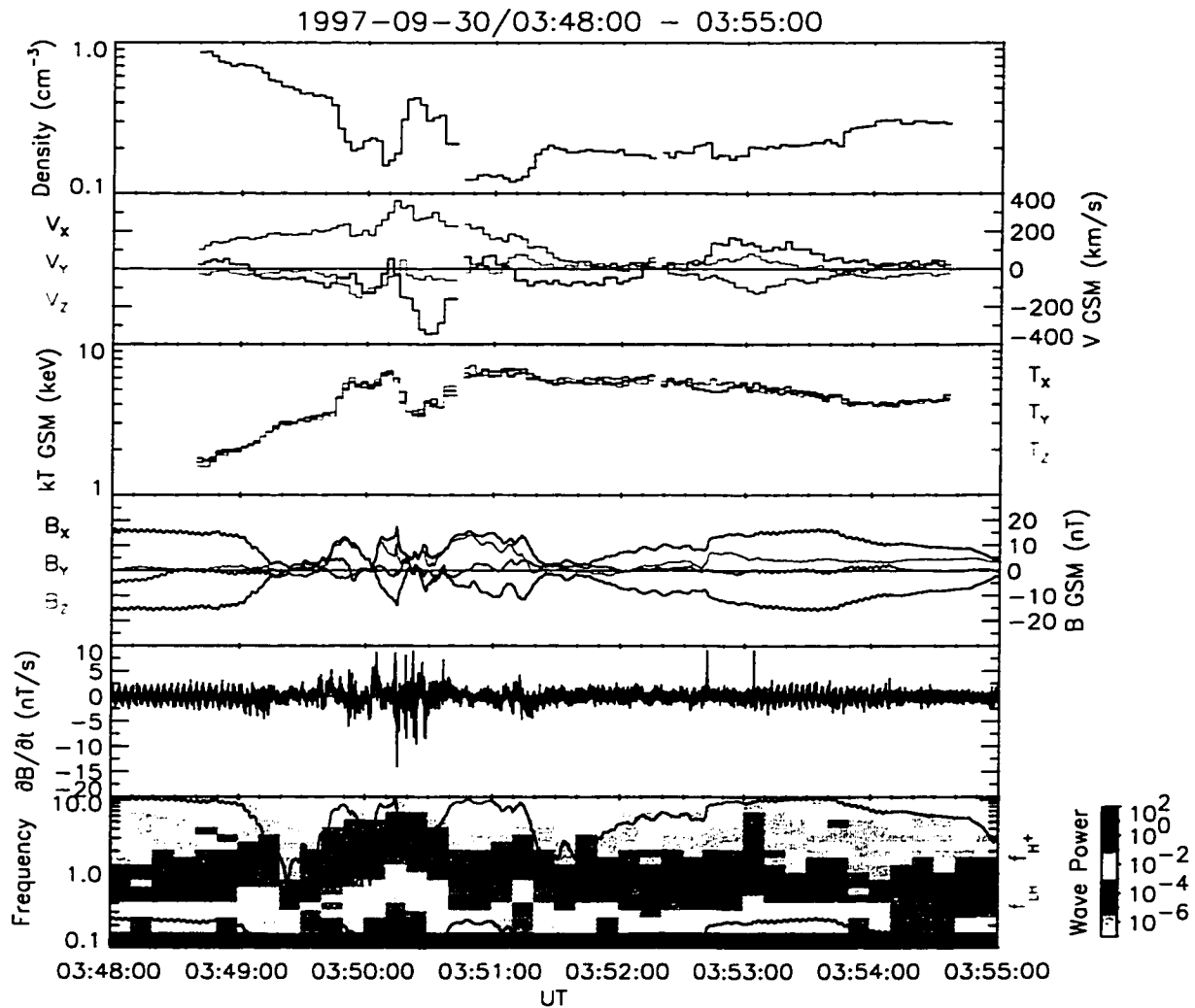
Figure 4.11: High time resolution magnetic field data and ion moments. From top to bottom: ion density; ion velocity; ion temperature; magnetic field; time derivative of the magnetic field; dynamic frequency spectrogram.

correlated throughout the 7-minute interval, are gradually decreasing and increasing, respectively. At about 03:49:45 UT, the density (temperature) decreases (increases) sharply. A few seconds later, the velocity peaks in the Y-direction followed by an increase and peak in the $-X$-component. Coincident with the increase in the $-X$-component of $\langle v \rangle$, there is a brief increase (decrease) in the density (temperature). As $\langle v \rangle_X$ decreases, $\langle v \rangle_Y$ remains above 200 km/s and the density (temperature) decreases (increases) even further compared to before the $-\langle v \rangle_X$ increase. Throughout this 20 second period, $|B|$ is between 5 and 10 nT, so the entire duration of this $-\langle v \rangle_X$ increase is just a few ion gyroperiods.

The bottom three panels show that the magnetic field is highly variable during this interval. B_X changes sign several times between 03:49 and 03:52 UT, indicating either a crossing of the current sheet or strong local turbulence. The minimum value of $|B|$ is about 1 nT, indicating that WIND is near the neutral sheet. $\partial B/\partial t$ routinely reaches values on the order of 10 nT/s. While smaller than the peak values observed on July 26, 1997, the induced electric field can still be $\sim$ 10 mV/m at length scales of the gyroradii of the thermal protons. Similar to July 26, 1997, the dynamic frequency spectrogram shows that there is wave power above the local proton gyrofrequency throughout this interval. In several instances there is significant wave power above the local lower hybrid frequency as well.

Figure 4.12 provides us with additional information in the form of $\langle v \rangle$ broken down into perpendicular and parallel components, omnidirectional ion fluxes up to 1 MeV, and Earthward and tailward energy spectrograms. This figure can be compared directly to Figure 3.21.

First, notice from the perpendicular and parallel velocity plot that the large ion $\langle v \rangle$ is directed largely in the perpendicular direction. There are transient parallel components mostly due to the changing direction of B. The brief velocity component pointing in the $-X$-direction also contributes to the small, varying parallel component.
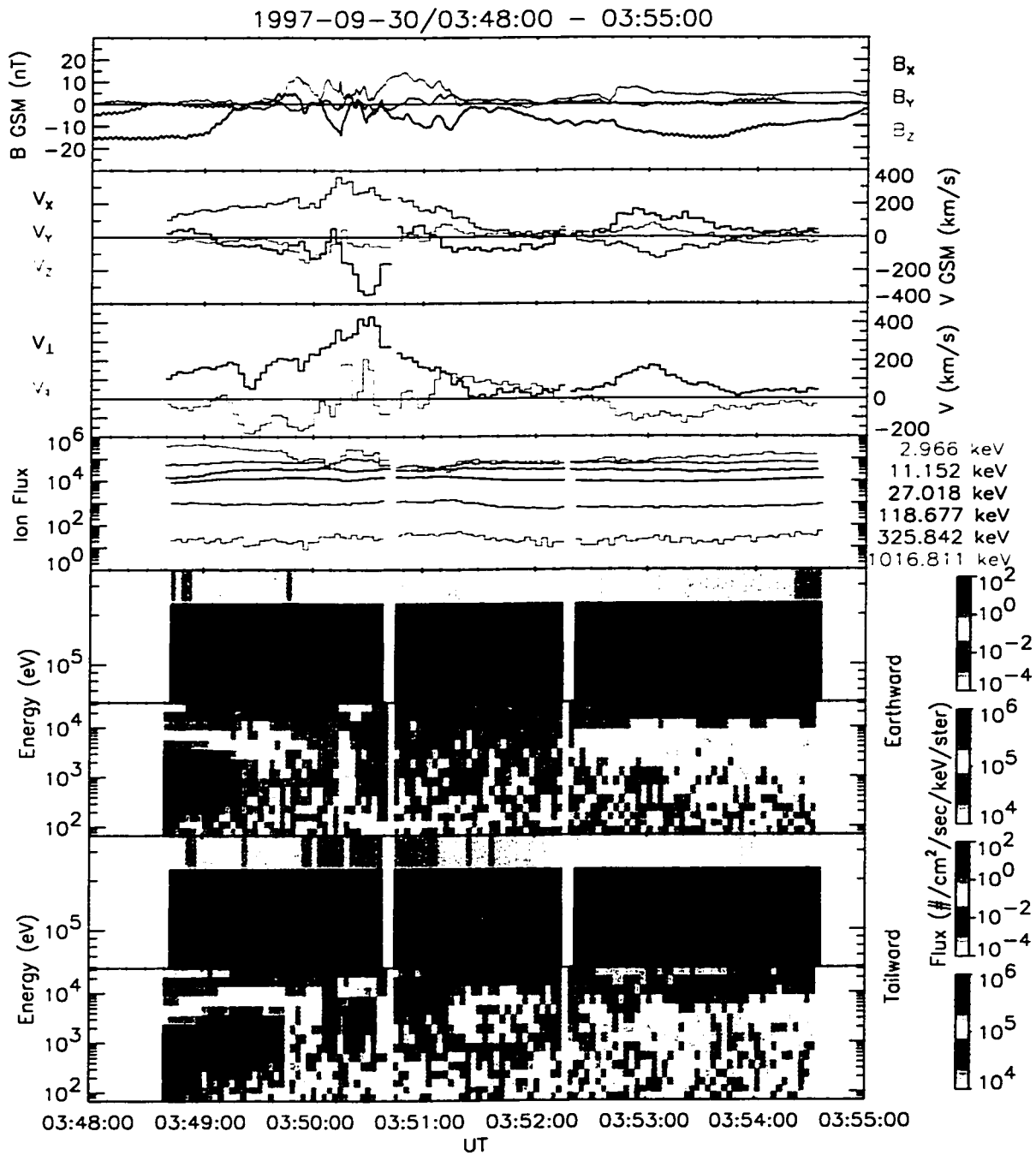
Figure 4.12: High time resolution magnetic field and ion data. From top to bottom: magnetic field; ion velocity in GSM and magnetic coordinates; omnidirectional ion flux; Earthward and tailward energy spectrograms.

The omnidirectional ion flux plot shows the ions with energies below a few keV gradually decreasing in flux as $\langle v \rangle$ increases. Ion fluxes from > 10 keV up to 100 keV show a gradual increase at the same time. This trend is interrupted briefly by an increase in the ion flux at energies below a few keV during the $-\langle v \rangle_X$ followed by their continued decrease.

The ion population responsible for the $-\langle v \rangle_X$ is clearly identifiable in the tailward energy spectrogram plot. Near the beginning of the interval, the fluxes of ions from 100 eV to a few keV are slowly decreasing in both directions. Around 03:49:45 UT, the fluxes at these energies drop dramatically leaving the higher energy component behind. At roughly 03:50:15 UT, there is an increase in the flux in the tailward direction between 1 and 10 keV. There is a slight decrease in the flux in the Earthward direction at the same time. This leads to the $-X$-component of $\langle v \rangle$. After this population disappears, there are only slight anisotropies in the high energy ion fluxes for the remainder of the interval, similar to July 26, 1997.

4.2.4 Electron Observations

High resolution electron data is shown in Figure 4.13. The format of this figure is the same as that of Figure 3.22. However, the scale on the 1 keV pitch angle spectrogram has been changed to improve clarity.

The electron density should be compared to the ion density shown in Figure 4.11. At the beginning of the interval, the densities are in good agreement. As the plasma density begins to decrease, the electron and ion density agreement becomes poor. In fact, the ion density becomes 3 to 4 times greater than the electron density when the densities are at their lowest. This indicates that at the beginning of the interval, most of the electrons had energies less than 1 keV. As the density began to decrease, the bulk of the electron distribution moved to higher energies above the limit of the electron detector. Similar behavior is seen on July 26, 1997 (Figure 3.22).

This effect is alluded to in the omnidirectional flux plot and the pitch angle spec-
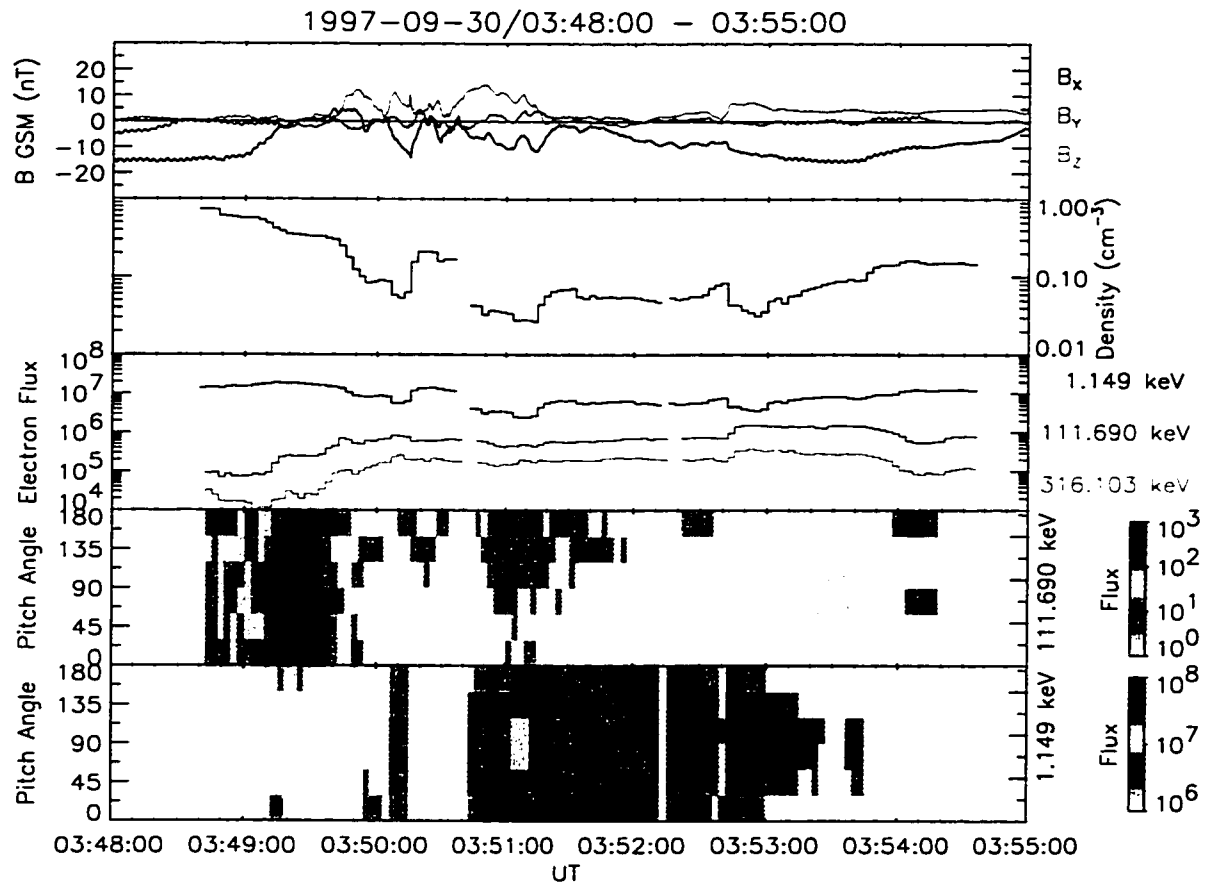
Figure 4.13: High time resolution magnetic field and electron data. From top to bottom: magnetic field; electron density; omnidirectional electron flux; pitch angle spectrograms.

trograms, as well. As the flux at 1 keV decreases after the beginning of the interval, the flux at higher energies increases. Based on the results from Chapter 3, particularly Figure 3.17, we would expect the transition energy, below which fluxes decrease and above which fluxes increase, to be around a few keV. The pitch angle spectrograms also show that the electron distribution can be quite field aligned during and after these active periods.

4.2.5 Plasma Distribution Functions

Ten three-second resolution ion distribution functions are shown in Figure 4.14. These distributions cover the time interval of the $-X$-component of $\langle v \rangle$. The first two distributions were taken immediately before the start of the large $-\langle v \rangle_X$; the second distribution corresponds to the maximum in $\langle v \rangle_Y$.

The first two distributions are quite energetic with very few particles with energies below about 1 keV (~ 500 km/s) present. The distributions are anisotropic in the direction perpendicular to the magnetic field. In the third distribution, the phase space density of ions with energies around a few keV increases noticeably. This increase is most clearly seen in the upper right quadrant. This lower energy but anisotropic component which is responsible for the $-\langle v \rangle_X$ persists for the next six distributions. Throughout these seven distributions, the direction of the $\langle v \rangle$ does not change; it remains pointed duskward and tailward. However, the direction of $\langle v \rangle$ as indicated by the small crosses in the contour plots does change as the magnetic field changes direction. In the final distribution, the high density, medium energy component begins to disappear leaving the anisotropic energetic component and a $\langle v \rangle_Y > 200$ km/s behind.

Eight electron distribution functions covering the same time interval as the ion distributions in the previous figure are shown in Figure 4.15. There is a data gap from 03:50:21 to 03:50:24 UT and another from 03:50:36 to 03:50:39 UT.

In the first two distributions, there are very few electrons present with energies
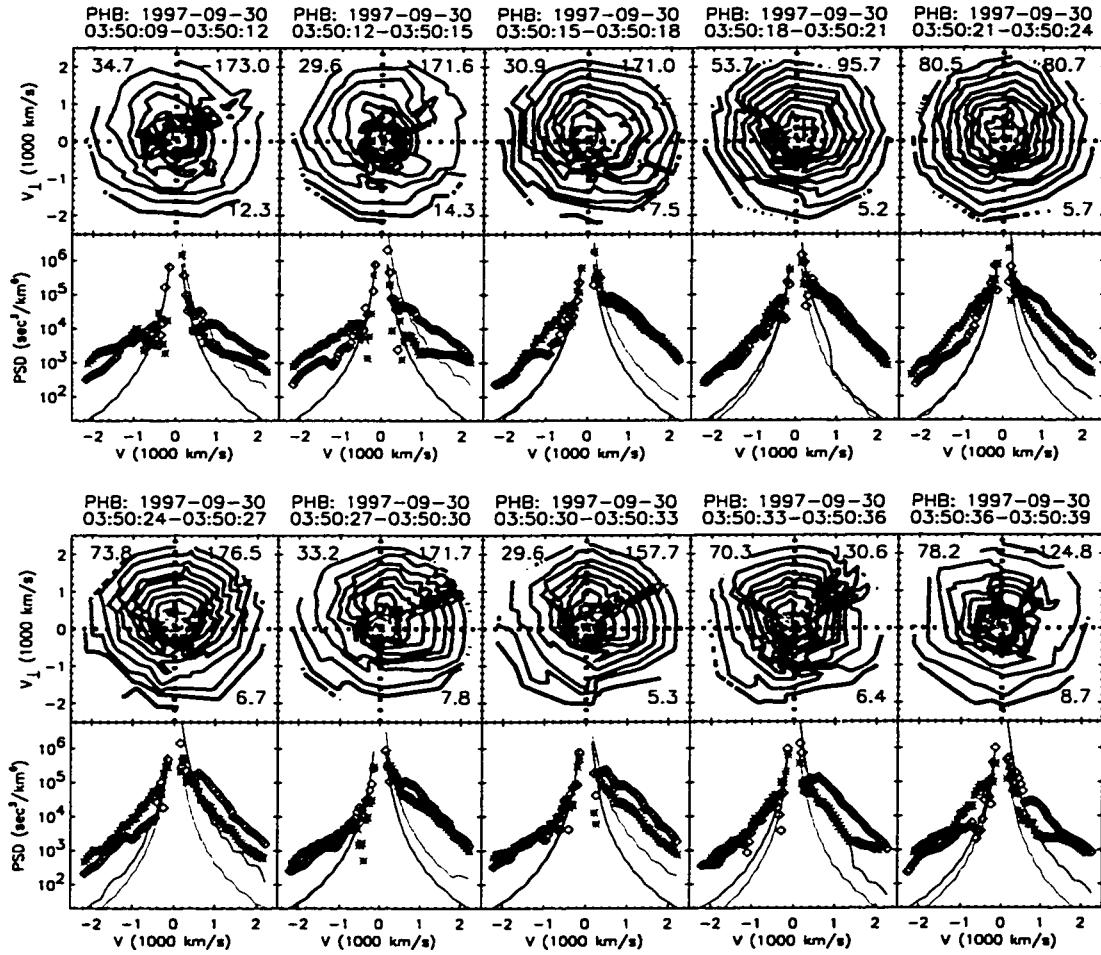
Figure 4.14: Ion distribution functions.
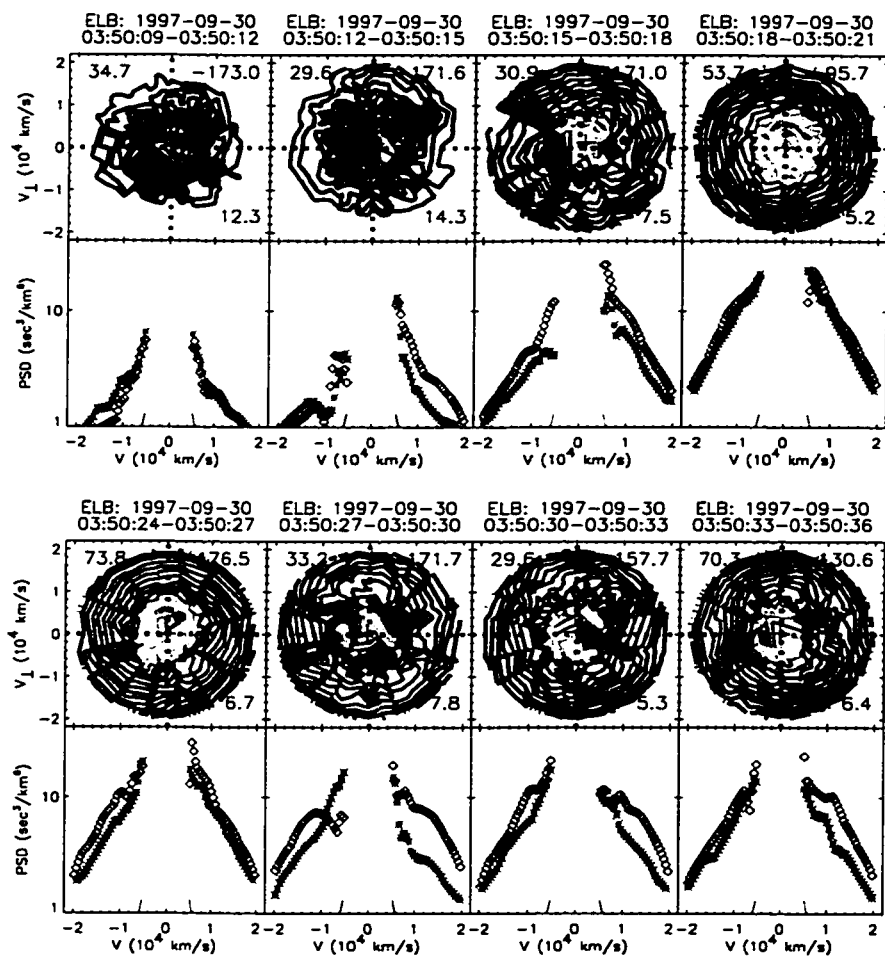
Figure 4.15: Electron distribution functions.

less that 1 keV. Presumably, most of the electron density is present at higher energies based on the disagreement between the ion and electron densities. The phase space density increases at all energies less than 1 keV during the third distribution. Since the electron population is changing during the integration time, this anisotropic distribution is most likely time aliased. The last five distributions gradually become more peaked in the perpendicular direction. This is in contrast to the electron distributions from July 26, 1997, shown in Figure 3.24 which are peaked in the filed aligned direction. However, the roles are reversed. In Figure 3.24, the low energy population is decreasing; in Figure 4.15, the low energy population is increasing. Figure 4.13 shows that shortly after this time, near 03:50:40 UT, the low energy electron flux drops, and the distribution becomes field aligned.

Finally, Figure 4.16 again looks at the ion and electron distributions at sub-spin time resolution, at 400 and 200 milliseconds, respectively, during the same time interval as covered in Figures 4.14 and 4.15. This figure is in the same format as Figure 3.25; however, the scale for the particle energy fluxes has been changed for clarity.

As seen in the top plot, the ion flux, particularly at 1 keV, starts out with very little anisotropy present. During and after the third frame, the anisotropy grows larger reaching a maximum amplitude of greater than an order of magnitude at both energies. This large anisotropy is due to the presence of the tailward going medium energy (1 to 10 keV) population. The last frame shows a significant decrease in the amplitude of the anisotropy at 11 keV as the tailward component disappears.

The electron energy fluxes show a gradual increase throughout the third frame in the second panel. The 100 eV electrons increase by nearly an order of magnitude. The low energy electron energy flux decreases slightly during the seventh frame, but otherwise the electron energy fluxes are fairly stable throughout the rest of the interval.

The magnetic field during this interval varies from about 5 to 20 nT. The direction

Figure 4.16: Ion, electron, and magnetic field data at sub-spin resolution. From top to bottom: ion energy flux in two energy channels; electron energy flux in two energy channels; magnetic field magnitude, azimuth (phi), and elevation (theta).
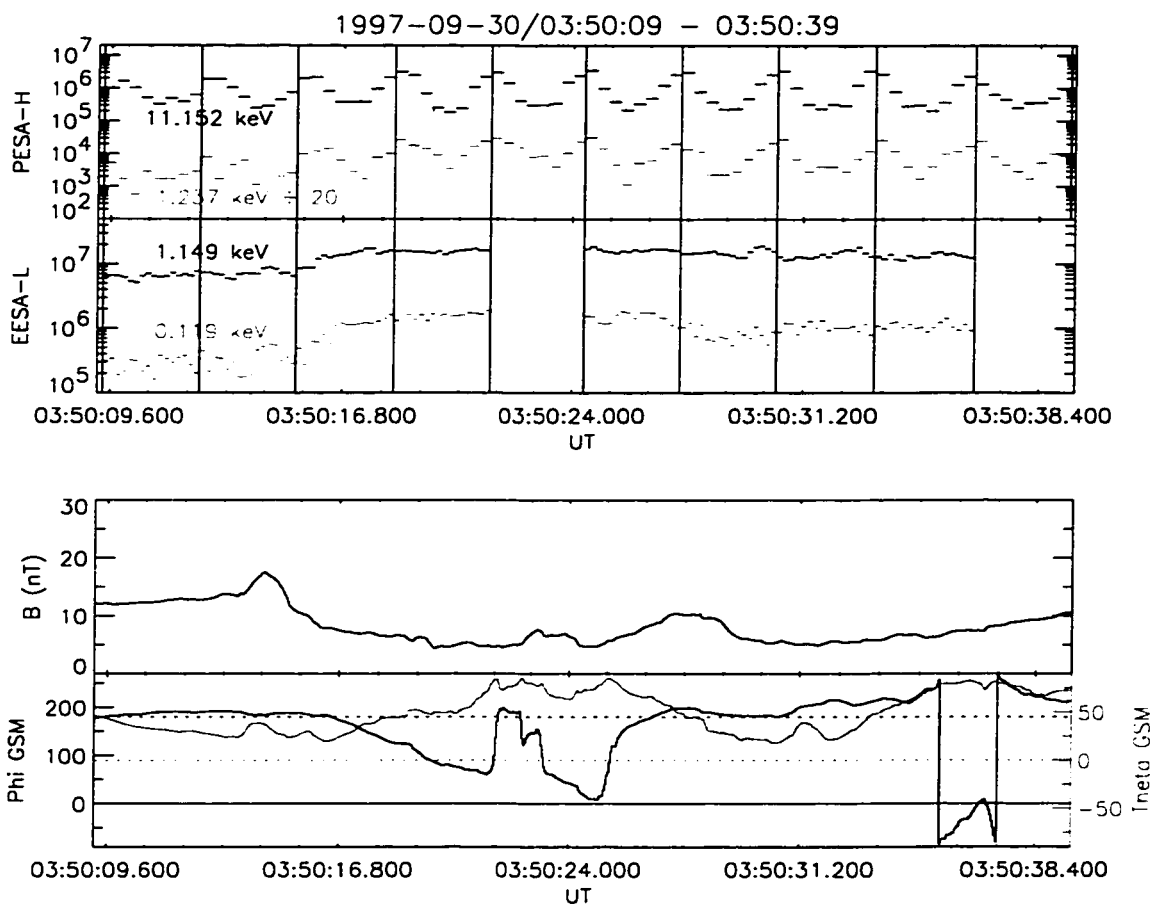
of **B** changes from nearly Sun-Earth aligned to vertical as WIND encounters the current sheet. There are significant perturbations in the Y-direction as well signified by the azimuth (phi) angle approaching 90 or 270°. During these cases, B_Y dominates over B_X, though B_Z is often the largest component during these excursion as signified by the large elevation (theta) angle.

4.2.6 Summary of Observations and Comparison to Pseudobreakups

The $\langle v \rangle$ event shown here is different from the previous events shown in that there appears to be a $\langle v \rangle$ embedded within another large $\langle v \rangle$. A large $\langle v \rangle$ mainly directed in the Y-direction is observed associated with a fluctuating magnetic field, a decrease in density and an anisotropic increase in the flux of high energy plasma as is typically the case. Within this $\langle v \rangle$ event, a tailward going, medium energy (1 to 10 keV) ion component appears, as evidenced by the ion spectrograms and distribution functions, resulting in an increase in the density, a decrease in the temperature and a large, brief $\langle v \rangle$ pointed in the $-X$-direction.

During this event, WIND approaches the current sheet where $|B|$ can be quite small, only a few nT. At these small magnetic fields, the gyroperiod becomes long ($\sim$ 10s of seconds) and the gyroradius of the thermal ions becomes quite large (over 1000 km), possibly larger than the scale size of gradients in the magnetic field. Under these conditions, an average picture of the plasma behavior cannot accurately describe the ion dynamics.

Many of the same features seen during this event are also seen during pseudo-breakups. These features include multicomponent distributions, large changes in the ion distributions on time scales comparable to and faster than the ion gyroperiod, large, rapidly fluctuating induced electric fields, and wave power at and above the local proton gyrofrequency. The similarity in the plasma behavior during this sub-storm event and during pseudobreakups as shown in the previous chapter suggests that the microphysical processes occurring in the plasma sheet are the same during

pseudobreakups and substorms.

Chapter 5

SUMMARY AND CONCLUSIONS

The goal of this dissertation has been to study the highest quality data on hand and to provide the most complete set of observations of the plasma sheet dynamics related to auroral activity. First, we find that the plasma sheet behavior appears the same during a wide range of auroral activity levels from pseudobreakups to substorms. Also, we have revealed several previously unreported and currently unexplained features. In spite of these new findings, many aspects of plasma sheet dynamics still remain unexplained. However, the new results presented in this thesis can be used as a stepping stone and guide for future work.

5.1   Summary of Ion Dynamics

We find that when WIND maps to the region of auroral activity, the plasma sheet is very dynamic. Fluctuations in the magnetic field, density decreases, ion velocity increases (typically in the Earthward direction), and temperature increases all coincident with auroral brightenings are observed. Other researchers, looking exclusively at ion moments, have reported many of the same features during large $\langle v \rangle$ increases including density decreases, temperature increases, and magnetic field variations [*Angelopoulos et al.*, 1992, 1997; *Fairfield et al.*, 1999], though their relation to auroral activity was not as stressed. Based on the work of *Nakamura et al.* [1991], most of this previous work considered the plasma sheet plasma as a single component fluid. Since a significant fraction of the $\langle v \rangle$ can be directed perpendicular to the magnetic field [*Baumjohann et al.*, 1990], the large $\langle v \rangle$ have been interpreted to be $\mathbf{E} \times \mathbf{B}$ flows

and have been assumed to be the result of an enhanced convection electric field in the dawn-dusk direction. Due to their intermittent behavior, the large $\langle v \rangle$ have been termed "bursty bulk flows," or BBFs [*Angelopoulos et al.*, 1992].

Even though the large $\langle v \rangle$ events shown here could be classified as BBFs, we refrain from using this nomenclature because our results show that that are additional new features present and that these events are not, in fact, "bulk flows." Large $\langle v \rangle$, then, are a result of anisotropic high energy ions typically with energies above 10 keV. Coincident with large $\langle v \rangle$, the fluxes of ions above a few 10s of keV increase in all directions, though the increase is usually anisotropic. At the same time, fluxes at lower energies usually drop, indicating a change in the ion population. It is not possible to know whether this change in population is a temporal effect due to local particle acceleration or a spatial effect as the spacecraft crosses a particle boundary.

A careful analysis of the ion and electron distribution functions shows that the plasma can be made up of multiple components including parallel beams, anisotropic energetic ions, and a low energy core. These different components are often observed behaving dynamically differently. For example, Figure 3.11 shows ion distributions containing a parallel beam and an anisotropic energetic component. The calculated $\langle v \rangle$ is in the Earthward direction, yet the beam is directed nearly 135° from the Earthward direction. Its presence is missed by only considering the moments. Similarly, distributions shown in Figure 4.5 also reveal the presence of a beam this time accompanied by an anisotropic low energy component. Both the beam and the low energy component are shifted perpendicular to $\mathbf{B}$ by $\sim$ 200 km/s, but the total magnitude of $\langle v \rangle$ is > 400 km/s. Hence, the observed large $\langle v \rangle$ do not adequately describe the ion dynamics and cannot be completely explained by an $\mathbf{E} \times \mathbf{B}$ drift.

At other times, the ion distributions appear non-gyrotropic (see, for example, Figures 3.12 and 4.6). In these cases, there is a highly energetic plateau extending off the scale in the positive perpendicular direction and a steep gradient in phase space density in the opposite direction with a seemingly stagnant low energy component

present. Possible explanations for these complex ion distributions include large energetic particle gradients in the $\mathbf{v} \times \mathbf{B}$ direction, time aliasing due to rapid changes in the magnetic field and particle distributions during the integration time, and complex, poorly understood ion behavior as a result of large, temporally and spatially varying induced electric fields.

5.2 Summary of Electron Dynamics

Also during plasma sheet disturbances associated with auroral activity, we observe changes in the electron population. Typically, the density decreases and the temperature increases as a result of a decrease of a high density, low temperature (< 1 keV) component and an increase in a low density, high temperature (few keV) component. The high temperature component extends up to 100s of keV in energy. The transition energy, above which electron fluxes increase and below which electron fluxes decrease, is around a few keV. We observe rapid changes in the electron spectrum occurring in about 1 second. During the rapid flux increase, the electrons are typically isotropic but become more field aligned at all energies a few minutes afterwards as the fluxes recover.

Hada et al. [1981] suggested that the field aligned electron distributions were the result of a Fermi acceleration mechanism due to highly curved field lines in the plasma sheet. However, this does not explain why the distributions become field aligned a few minutes after the spectrum change. Associated with the electron spectrum change, the magnetic field is typically fluctuating rapidly and becoming more dipolar, that is, less curved. Therefore, one would expect this mechanism to produce field aligned distributions before onset when the field lines are highly curved rather than a few minutes after.

5.3   Summary of Ion Dynamics on Kinetic Time Scales

Observations made on kinetic time scales reveal new, previously unreported features. For example, the ion moments can contain significant structure, that is, multiple peaks in $|\langle v \rangle|$ separated in time by a few proton gyroperiods and abrupt changes (up to 100%) in both the direction and magnitude of $\langle v \rangle$ on time scales comparable to the local proton gyroperiod. Also, new ion components can appear and disappear in a few gyroperiods.

Directional changes in $\langle v \rangle$ do not appear constrained by or correlated with the direction of **B**. Figures 3.18 and 3.20 show that even though the direction of $\langle v \rangle$ is constant (in this case, in the X-direction), $\langle v \rangle$ is first directed perpendicular to then parallel along the magnetic field as the direction of the magnetic field changes. This implies that the ions are not responding exclusively to local magnetic field effects. It is possible that the ions in these events are non-magnetized; the local β of the plasma at this time is of order 1. The magnetic field may also be changing in direction or magnitude over scale sizes of the ion gyroradius, hundreds of km for keV ions in the plasma sheet. The locally measured magnetic field may not be representative of the magnetic field that the ions encounter during a significant fraction of their orbits. Inductive electric fields and time changes in inductive electric fields will additionally influence particle dynamics.

At the same time, large amplitude, high frequency magnetic field fluctuations are seen with $|\partial B/\partial t|$ often reaching ~ 10 nT/s. These magnetic field fluctuations will give rise to strong, rapidly changing induced electric fields. At scale lengths on the order of the gyroradius of a 1 keV proton (several hundred km in a 10 to 20 nT field), the induced electric field strength will be on the order of 10 mV/m. This is at least an order of magnitude larger than typical expected dawn-to-dusk electric fields of a few tenths of mV/m. This is similar in magnitude to $\langle v \rangle \times$ **B** (500 km/s $\times$ 20 nT = 10 mV/m), which is usually interpreted as an enhanced con-

vective electric field [*Angelopoulos et al.*, 1992]. However, the induced electric fields, rather than being quasi-static in the Y-direction for Earthward transport, are rapidly changing in direction and magnitude as **B** varies on time scales faster than the proton gyroperiod.

These magnetic fluctuations have significant wave power present at frequencies up to and exceeding the local proton gyrofrequency and, at times, the local lower hybrid frequency. *Lui et al.* [1992] saw similar broadband increases in wave power at similar locations and interpreted their observations as a signature of a cross field current instability giving rise to current disruption. *Perraut et al.* [2000] have also noted enhanced wave power at and above the proton gyrofrequency at geosynchronous altitudes which may be related to a parallel current-driven instability.

The ion distribution functions contain complex features that include large gradients and anisotropies in phase space. These features cannot be reproduced by a superposition of several shifted isotropic distributions. Significant changes also occur in these distribution functions on time scales comparable to the local proton gyroperiod indicating that the plasma is very dynamic. It is clear from the rapid fluctuations in **B** and from the changes in the ion distribution functions that the ions cannot be behaving adiabatically.

The electrons undergo similar changes on 3-second time scales. However, the electron gyroperiod, which is on the order of milliseconds for typical observed magnetic field values, is far below our temporal resolution. Unless there are large changes in the magnetic and electric fields at these short time scales, we expect the electrons to behave adiabatically.

Lastly, our observations clearly indicate that variations occur on kinetic time scales. These results highlight the need for high time resolution data. Changing the integration time drastically changes the picture we get of the plasma dynamics. The magnitude of fast fluctuations in **B** are usually underestimated and some are completely missed when integrating over time scales longer than about 1 second.

Also peaks in the ion $\langle v \rangle$ are substantially lower and structure is smeared out when averaging over several proton gyroperiods. This bursty behavior of $\langle v \rangle$ was similarly noted by *Baumjohann et al.* [1990] and *Angelopoulos et al.* [1992] as an increase in the peak $|\langle v \rangle|$ with shorter time resolution. Peak $\langle v \rangle$ are measured when the integration time is on the order of the gyroperiod. Clearly, an incomplete picture of the plasma sheet behavior is obtained using lower time resolution data.

5.4 Relationship of Pseudobreakups to Substorms

By studying additional events including expansive auroral substorms, we find that the plasma sheet dynamics appears the same regardless of the size of the region of the ionosphere covered by intense emission. The same features are seen in the ion and electron distributions during pseudobreakups and large substorms. This similarity persists down to the shortest time scales observable. On the basis of this similarity, we conclude that the microphysical processes occurring in the plasma sheet are the same for pseudobreakups and substorms. We suggest, that, analogous to the aurora, which is observed with a continuum of spatial and temporal scales and intensities, plasma sheet disturbances occur with a similar continuum of scales and intensities.

Using a wide variety of ground based, ionospheric, and magnetospheric observations, *Nakamura et al.* [1994], *Rostoker* [1998], and *Aikio et al.* [1999] have also concluded that pseudobreakups and substorms are the result of the same physical processes in the magnetosphere. The only difference is the scale size of the resulting aurora.

Even though the exact physical processes or instabilities which lead to the dynamic plasma sheet behavior described above and in turn are related to the mechanisms which precipitate electrons to generate the intense aurora are unknown, *Parks et al.* [2002] have described a phenomenology of how the plasma becomes unstable, based in part on these results. Given a plasma distribution that is initially in equilibrium

in an inhomogeneous environment such as the plasma sheet, gradient, curvature and time dependent electromagnetic forces will modify the distribution. Different regions of phase space will be transported into different regions of the plasma sheet, and the original distribution will become altered and more complex as plasmas of different origins are mixed. As the plasma evolves in space and time, a non-equilibrium component can develop locally that contributes to free energy. This would permit a considerable amount of free energy to be built up in selected regions of the plasma sheet which instability processes could tap into. How much free energy and over what regions this free energy accumulates determines the total energy available to be dissipated and the size and intensity of the resulting aurora. Local properties of the ambient plasma distributions would then be important in determining what instability criteria are satisfied.

5.5 Future Work

We have demonstrated that the plasma sheet dynamics are much more complicated than currently envisioned. Many of the physical causes of the features that we have shown are not understood. It is clear that kinetic and nonlinear processes are operating. These features are also not incorporated in existing models of magnetospheric processes. For example, with the exception of *Winglee* [1998], current models do not include the presence of multiple components in the plasma sheet. It is important that these new features be included in future models so that a comprehensive picture of magnetospheric process can be developed. In addition, modeling efforts must incorporate kinetic and nonlinear mechanisms.

This dissertation has not addressed what physical mechanism or instability is responsible for the observed plasma dynamics. Whatever the processes are, our results show that kinetic and nonlinear physics are important. Detailed analyses of specific features in the distributions and their time rate of change correlated with electric and

magnetic wave data may give us a deeper understanding of the microphysics involved. For example, what is responsible for accelerating the ions to MeV energies and the electron to hundreds of keV energies? Separating adiabatic from non-adiabatic features to identify the specific acceleration processes is one avenue of possibly fruitful future research. How important are wave-particle interactions in accelerating particles and modifying the distributions? Can we identify what these interactions are and if the plasma distributions are favorable for instability growth? The identification of particular plasma processes may help constrain or eliminate current competing theories. As a result new models of how the plasma sheet operates and how substorms develop may be formulated.

Even though we have presented the most complete set of observations currently available, there are still limitations to the data. There are features that we have not and cannot address. First, we haven't addressed the issue of composition. The work of *Chappell et al.* [1987] and the recent simulations of *Winglee* [2000] have suggested that a considerable amount of ionospheric plasma may be present in the plasma sheet. As a result, there can be multiple ion species present including He^+ and O^+. Our analysis has assumed all ions are protons. Since He^+ and O^+ are more massive than H+ by a factor of 4 and 12, respectively, the gyroperiod of these heavier ions are longer than the proton gyroperiod by the same factors. If heavier ions are present in significant quantities, then the conclusions that the ions are not behaving adiabatically and that kinetic effects are important in describing the particle dynamics would be further strengthened.

We also don't have information available about the plasma dynamics below 70 eV. Typical ionospheric plasma temperatures are on the order of 1 eV. Even if the plasma is heated during transport to the plasma sheet, the bulk of the ionospheric contribution may be below the threshold of the instruments.

Additionally, there are still features present in the data that are not time resolved. Features in the electron and ion data can change on time scales faster than the local

ion gyroperiod. The electron data as well as the ion data appear time aliased, but we currently do not have the time resolution necessary to fully describe the processes responsible for the changing distributions.

Finally, an inherent problem of single spacecraft measurements is one of temporal and spatial ambiguity. We do not know whether the observed plasma sheet processes are temporal ones which we see evolving or spatial effects caused by different regions of the magnetotail passing over the spacecraft. Multispacecraft observations should help resolve this ambiguity. Observations of these plasma processes by Cluster II or, in the future, MMS in the near-Earth plasma sheet will most likely play a large role in the advancement of our knowledge of plasma sheet dynamics.

BIBLIOGRAPHY

[*Aikio et al.*, 1999] Aikio, A. T., V. A. Sergeev, M. A. Shukhtina, L. I. Vagina, V. Angelopoulos, and G. D. Reeves, Characteristics of pseudobreakups and substorms observed in the ionosphere, at geosynchronous orbit, and in the midtail, *J. Geophys. Res.*, *104*, 12,263, 1999.

[*Akasofu*, 1964] Akasofu, S.-I., The development of the auroral substorm, *Planet. Space Sci.*, *12*, 273, 1964.

[*Angelopoulos et al.*, 1992] Angelopoulos, V., W. Baumjohann, C. F. Kennel, F. V. Coroniti, M. G. Kivelson, R. Pellat, R. J. Walker, H. Lühr, and G. Paschmann, Bursty bulk flows in the inner central plasma sheet, *J. Geophys. Res.*, *97*, 4027, 1992.

[*Angelopoulos et al.*, 1997] Angelopoulos, V., T. D. Phan, D. E. Larson, F. S. Mozer, R. P. Lin, K. Tsuruda, H. Hayakawa, T. Mukai, S. Kokubun, T. Yamamoto, D. J. Williams, R. W. McEntire, R. P. Lepping, G. K. Parks, M. Brittnacher, G. Germany, J. Spann, H. J. Singer, and K. Yumoto, Magnetotail flow bursts: Association to global magnetospheric circulation, relationship to ionospheric activity and direct evidence for localization, *Geophys. Res. Lett.*, *24*, 2271, 1997.

[*Arballo et al.*, 1998] Arballo, J. K., C. M. Ho, G. S. Lakhina, B. T. Tsurutani, X.-Y. Zhou, Y. Kamide, J.-H. Shue, S.-I. Akasofu, R. P. Lepping, C. C. Goodrich, K. Papadopoulos, A. S. Sharma, and J. G. Lyon, Pseudobreakups during January 10, 1997, in *Substorms-4*, S. Kokubun and Y. Kamide, eds., Terra Scientific Publish-

134

ing Company/Kluwer Acacdemic Publishers, Tokyo/Dordrecht, The Netherlands, 1998.

[*Bame et al.*, 1978] Bame, S. J., J. R. Asbridge, H. E. Felthauser, J. P. Glore, G. Paschmann, P. Hemmerich, K. Lehmann, and H. Rosenbauer, ISEE-1 and ISEE-2 fast plasma experiment and the ISEE-1 solar wind experiment, *IEEE Trans. Geosci. Electronics, GE-16*, 216, 1978.

[*Baumjohann et al.*, 1990] Baumjohann, W., G. Paschmann, and H. Lühr, Characteristics of high-speed ion flows in the plasma sheet, *J. Geophys. Res., 95*, 3801, 1990.

[*Berkey and Kamide*, 1976] Berkey, F. T., and Y. Kamide, On the distribution of global auroras during intervals of magnetospheric quiet, *J. Geophys. Res., 81*, 4701, 1976.

[*Carlson et al.*, 1982] Carlson, C. W., D. W. Curtis, G. Paschmann, and W. Michael, An instrument for rapidly measuring plasma distribution functions with high resolution, *Adv. Space Res., 2*, 67, 1982.

[*Chappell et al.*, 1987] Chappell, C. R., T. E. Moore, J. H. Waite, Jr., The ionosphere as a fully adequate source of plasma for the Earth's magnetosphere, *J. Geophys. Res., 92*, 5896, 1987.

[*Chen et al.*, 2000a] Chen, L., D. Larson, R. P. Lin, M. McCarthy, and G. Parks, Multicomponent plasma distributions in the tail current sheet associated with substorms, *Geophys. Res. Lett., 27*, 843, 2000a.

[*Chen et al.*, 2000b] Chen, L-J., G. K. Parks, M. McCarthy, D. Larson, and R. P. Lin, Kinetic properties of bursty bulk flow events, *Geophys. Res. Lett., 27*, 1847, 2000b.

[*Coates et al.*, 1985] Coates, A. J., J. A. Bowles, R. A. Gowen, B. K. Hancock, A. D. Johnstone, and S. J. Kellock, The AMPTE UKS three-dimensional ion experiment, *IEEE Trans. Geosci. Remote Sens.*, *GE-23*, 287, 1985.

[*Coroniti et al.*, 1968] Coroniti, F. V., R. L. McPherron, and G. K. Parks, Studies of the magnetospheric substorm, 3, Concept of the magnetospheric substorm and its relation to electron precipitation and micropulsations, *J. Geophys. Res.*, *73*, 1715, 1968.

[*Cummings et al.*, 1968] Cummings, W. D., J. N. Barfield, and P. J. Coleman, Jr., Magnetospheric substorms observed at the synchronous orbit, *J. Geophys. Res.*, *73*, 6687, 1968.

[*Eastman et al.*, 1984] Eastman, T. E., L. A. Frank, W. K. Peterson, and W. Lennartsson, The plasma sheet boundary layer, *J. Geophys. Res.*, *89*, 1553, 1984.

[*Elvey*, 1957] Elvey, C. T., Problems of auroral morphology, *Proc. Nat. Acad. Sci., Wash.*, *43*, 63, 1957.

[*Erickson et al.*, 1996] Erickson, G. M., W. J. Burke, M. Heinemann, J. C. Samson, and N. C. Maynard, Towards a complete conceptual model of substorm onsets and expansions *Proc. Third International Conference on Substorms (ICS-3)*, ESA SP-389, 315, 1996.

[*Fairfield et al.*, 1999] Fairfield, D. H., T. Mukai, M. Brittnacher, G. D. Reeves, S. Kokubun, G. K. Parks, T. Nagai, H. Matsumoto, K. Hashimoto, D. A. Gurnett, and T. Yamamoto, Earthward flow bursts in the inner magnetotail and their relation to auroral brightenings, AKR intensifications, geosynchronous particle injections and magnetic activity, *J. Geophys. Res.*, *104*, 355, 1999.

[*Fillingim et al.*, 2000] Fillingim, M. O., G. K. Parks, L. J. Chen, M. Brittnacher, G. A. Germany, J. F. Spann, D. Larson, and R. P. Lin, Coincident POLAR/UVI and WIND observations of pseudobreakups, *Geophys. Res. Lett., 27,* 1379, 2000.

[*Fillingim et al.*, 2001] Fillingim, M. O., G. K. Parks, L. J. Chen, M. McCarthy, J. F. Spann, and R. P. Lin, Comparison of plasma sheet dynamics during pseudobreakups and expansive aurora, *Phys. Plasmas, 8,* 1127, 2001.

[*Fillingim et al.*, 2002] Fillingim, M. O., G. K. Parks, R. P. Lin, M. McCarthy, and A. Szabo, Observations of magnetospheric disturbances during auroral activity, in *Storm-Substorm Relationship*, Geophysical Monograph Series, in press.

[*Frank et al.*, 1978] Frank, L. A., D. M. Yeager, H. D. Owens, K. L. Ackerson, and M. R. English, Quadrispherical LEPEDEAS for ISEE's-1 and -2 plasms measurements, *IEEE Trans. Geosci. Electronics, GE-16,* 221, 1978.

[*Frank et al.*, 1994] Frank, L. A., K. L. Ackerson, W. R. Paterson, J. A. Lee, M. R. English, and G. L. Pickett, The comprehensive plasma instrumentation (CPI) for the GEOTAIL spacecraft, *J. Geomag. Geoelectr., 46,* 23, 1994.

[*Germany et al.*, 1998] Germany, G. A., J. F. Spann, G. K. Parks, M. J. Brittnacher, R. Elsen, L. Chen, D. Lummerzheim, and M. H. Rees, Auroral observations from the POLAR ultraviolet imager (UVI), in *Geospace Mass and Energy Flow: Results From the International Solar-Terrestrial Physics Program*, Geophysical Monograph 104, J. L. Horwitz, D. L. Gallagher, and W. K. Peterson, eds., American Geophysical Union, Washington, DC, 1998.

[*Hada et al.*, 1981] Hada, T., A. Nishida, T. Terasawa, E. W. Hones, Jr., Bi-directional electron pitch angle anisotropy in the plasma sheet, *J. Geophys. Res., 86,* 11,211, 1981.

[*Hones et al.*, 1967] Hones, E. W., Jr., J. R. Asbridge, S. J. Bame, and I. B. Strong, Outward flow of plasma in the magnetotail following geomagnetic bays, *J. Geophys. Res.*, *72*, 5879, 1967.

[*Hones et al.*, 1976] Hones, E. W., Jr., S.-I. Akasofu, J. H. Wolcott, S. J. Bame, D. H. Fairfield, and C.-I. Meng, Correlated observations of several auroral substorms on February 17, 1971, *J. Geophys. Res.*, *81*, 1725, 1976.

[*Kan et al.*, 1988] Kan, J. R., L. Zhu, and S.-I., Akasofu, A theory of substorms: Onset and subsidence, *J. Geophys. Res.*, *93*, 5624, 1988.

[*Kaufmann*, 1987] Kaufmann, R. L., Substorm currents: Growth phase and onset *J. Geophys. Res.*, *92*, 7471, 1987.

[*Koskinen et al.*, 1993] Koskinen, H. E. J., R. E. Lopez, R. J. Pellinen, T. I. Pulkkinen, D. N. Baker, and T. Bosinger, Pseudobreakup and substorm growth phase in the ionosphere and magnetosphere, *J. Geophys. Res.*, *98*, 5801, 1993.

[*Lepping et al.*, 1995] Lepping, R. P., M. H. Acuña, L. F. Burlaga, W. M. Farrell, J. A. Slavin, K. H. Schatten, F. Mariani, N. F. Ness, F. M. Neubauer, Y. C Whang, J. B. Byrnes, R. S. Kennon, P. V. Panetta, J. Scheifele, and E. M. Worley, The WIND magnetic field field investigation, *Space Sci. Rev.*, *71*, 207, 1995.

[*Lin et al.*, 1995] Lin, R. P., K. A. Anderson, S. Ashford, C. Carlson, D. Curtis, R. Ergun, D. Larson, J. McFadden, M. McCarthy, G. K. Parks, H. Rème, J. M. Bosqued, J. Coutelier, F. Cotin, C. D'uston, K.-P. Wenzel, T. R. Sanderson, J. Henrion, J. C. Ronnet, and G. Paschmann, A three-dimensional plasma and energetic particle investigation for the WIND spacecraft, *Space Sci. Rev.*, *71*, 125, 1995.

138

[*Lui*, 1991] Lui, A. T. Y., A synthesis of magnetospheric substorm models, *J. Geophys. Res.*, *96*, 1849, 1991.

[*Lui et al.*, 1992] Lui, A. T. Y. R. E. Lopez, B. J. Anderson, K. Takahashi, L. J. Zanetti, R. W. McEntire, T. A. Potemra, D. M. Klumpar, E. M. Greene, and R. Strangeway, Current disruptions in the near-earth neutral sheet region, *J. Geophys. Res.*, *97*, 1461, 1992.

[*McPherron*, 1970] McPherron, R. L., Growth phase of magnetospheric substorms, *J. Geophys. Res.*, *75*, 5592, 1970.

[*McPherron*, 1972] McPherron, R. L., Substorm related changes in the geomagnetic tail: The growth phase, *Planet. Space. Sci.*, *20*, 1521, 1972.

[*McPherron*, 1979] McPherron, R. L., Magnetospheric substorms, *Rev. Geophys. Space Phys.*, *17*, 657, 1979.

[*McPherron*, 1991] McPherron, R. L., Physical processes producing magnetospheric substorms and magnetic storms, in *Geomagnetism*, vol. 4, J. A. Jacobs, ed., Academic Press, San Diego, CA, 1991.

[*Mukai et al.*, 1994] Mukai, T., S. Machida, Y. Saito, M. Hirahara, T. Terasawa, N. Kaya, T. Obara, M. Ejiri, and A. Nishida, The low energy particle (LEP) experiment onboard the GEOTAIL satellite, *J. Geomag. Geoelectr.*, *46*, 669, 1994.

[*Nakamura et al.*, 1991] Nakamura, M., G. Paschmann, W. Baumjohann, and N. Sckopke, Ion distributions and flows near the neutral sheet, *J. Geophys. Res.*, *96*, 5631, 1991.

[*Nakamura et al.*, 1992] Nakamura, M., G. Paschmann, W. Baumjohann, and N. Sckopke, Ion distributions and flows in and near the plasma sheet boundary layer, *J. Geophys. Res.*, *97*, 1449, 1992.

[*Nakamura et al.*, 1994] Nakamura, R., D. N. Baker, T. Yamamoto, R. D. Belian, E. A. Bering III, J. R. Benbrook, and J. R. Theall, Particle and field signatures during pseudobreakup and major expansion onset, *J. Geophys. Res.*, *99*, 207, 1994.

[*Ohtani et al.*, 1993] Ohtani, S., B. J. Anderson, D. G. Sibeck, P. T. Newell, L. J. Zanetti, T. A. Potemra, K. Takahashi, R. E. Lopez, V. Angelopoulos, R. Nakamura, D. M. Klumpar, and C. T. Russell, A multisatellite study of a pseudo-substorm onset in the near-Earth magnetotail, *J. Geophys. Res.*, *98*, 19,355, 1993.

[*Parks*, 1991] Parks, George K., *Physics of Space Plasmas: An introduction*, Addison-Wesley, Redwood City, CA, 1991.

[*Parks et al.*, 2001] Parks, G. K., L. J. Chen, M. Fillingim, and M. McCarthy, Kinetic characterization of plasma sheet dynamics, *Space Sci. Rev.*, *95*, 237, 2001.

[*Parks et al.*, 2002] Parks, G. K., L. J. Chen, M. Fillingim, R. P. Lin, D. Larson, and M. McCarthy, A new framework for studying the relationship of aurora and plasma sheet dynamics, *J. Atmos. Terrestr. Phys.*, *64*, 115, 2002.

[*Paschmann et al.*, 1985] Paschmann, G., H. Loidl, P. Obermayer, M. Ertl, R. Laborenz, N. Sckopke, W. Baumjohann, C. W. Carlson, and D. W. Curtis, The plasma instrument for AMPTE IRM, *IEEE Trans. Geosci. Remote Sens.*, *GE-23*, 262, 1985.

[*Perraut et al.*, 2000] Perraut, S., O. Le Contel, A. Roux, and A. Pedersen, Current-driven electromagnetic ion cyclotron instability at substorm onset, *J. Geophys. Res.*, *105*, 21,097, 2000.

[*Pulkkinen*, 1996] Pulkkinen, T. I., Pseudobreakup or substorm?, *Proc. Third International Conference on Substorms (ICS-3)*, ESA SP-389, 285, 1996.

[*Pulkkinen et al.*, 1998] Pulkkinen, T. I., D. N. Baker, M. Wiltberger, C. Goodrich, R. E. Lopez, and J. G. Lyon, Pseudobreakup and substorm onset: Observations and MHD simulations compared, *J. Geophys. Res.*, *103*, 14,847, 1998.

[*Richmond*, 1995] Richmond, A. D., Ionospheric electrodynamics using magnetic apex coordinates, *J. Geomag. Geoelectr.*, *47*, 191, 1995.

[*Rostoker*, 1998] Rostoker, G., On the place of the pseudo-breakup in a magnetospheric substorm, *Geophys. Res. Lett.*, *25*, 217, 1998.

[*Sauvaud et al.*, 1987] Sauvaud, J. A., J. P. Treilhou, A. Saint-Marc, J. Dandouras, H. Rème, A. Korth, G. Kremser, G. K. Parks, A. N. Zaitzev, V. Petrov, L. Lazutine, and R. Pellinen, Large scale response of the magnetosphere to a southward turning of the interplanetary magnetic field, *J. Geophys. Res.*, *92*, 2365, 1987.

[*Scudder et al.*, 1995] Scudder, J., F. Hunsacker, G. Miller, J. Lobell, T. Zawistowski, K. Ogilvie, J. Keller, D. Chornay, F. Herrero, R. Fitzenreiter, D. Fairfield, J. Needell, D. Bodet, J. Googins, C. Kletzing, R. Torbert, J. Vandiver, R. Bentley, W. Fillius, C. McIlwain, E. Whipple, and A. Korth, HYDRA - A 3-dimensional electron and ion hot plasma instrument for the POLAR spacecraft of the GGS mission, *Space Sci. Rev.*, *71*, 459, 1995.

[*Sergeev et al.*, 1986] Sergeev, V. A., A. G. Yahnin, R. A. Rakhmatulin, S. I. Solovjev, F. S. Mozer, D. J. Williams, and C. T. Russell, Permanent flare activity in the magnetosphere during periods of low magnetic activity in the auroral zone, *Planet. Space Sci.*, *34*, 1169, 1986.

[*Shah et al.*, 1985] Shah, H. M., D. S. Hall, and C. P. Chaloner, The electron experiment on AMPTE UKS, *IEEE Trans. Geosci. Remote Sens.*, *GE-23*, 293, 1985.

[*Shelley et al.*, 1995] Shelley, E. G., A. G. Ghielmetti, H. Balsiger, R. K. Black, J. A. Bowles, R. P. Bowman, O. Bratschi, J. L. Burch, C. W. Carlson, A. J. Coker, J. F. Drake, J. Fischer, J. Geiss, A. Johnstone, D. L. Kloza, O. W. Lennartsson, A. L. Magoncelli, G. Paschmann, W. K. Peterson, H. Rosenbauer, T. C. Sanders, M. Steinacher, D. M. Walton, B. A. Whalen, and D. T. Young, The toroidal imaging mass-angle spectrograph (TIMAS) for the POLAR mission, *Space Sci. Rev.*, *71*, 497, 1995.

[*Takahashi and Hones*, 1988] Takahashi, K. and E. W. Hones, Jr., ISEE 1 and 2 observations of ion distributions at the plasma sheet-tail lobe boundary, *J. Geophys. Res.*, *93*, 8558, 1988.

[*Torr et al.*, 1995] Torr, M. R., D. G. Torr, M. Zukic, R. B. Johnson, J. Ajello, P. Banks, K. Clark, K. Cole, C. Keffer, G. Parks, B. Tsurutani, and J. Spann, A far ultraviolet imager for the International Solar-Terrestrial Physics mission, *Space Sci. Rev.*, *71*, 329, 1995.

[*Tsyganenko*, 1989] Tsyganenko, N. A., A magnetospheric magnetic field model with a warped tail current sheet, *Planet. Space Sci.*, *37*, 5, 1989.

[*Winglee*, 1998] Winglee, R. M., Multi-fluid simulations of the magnetosphere: the identification of the geopause and its variation with IMF, *Geophys. Res. Lett.*, *25*, 4441, 1998.

[*Winglee*, 2000] Winglee, R. M., Mapping of ionospheric outflows into the magnetosphere for varying IMF conditions, *J. Atmos. Terrestr. Phys.*, *62*, 527, 2000.

VITA

A long time ago (at least to him), Matthew Owen Fillingim was born in Bedford, IN, the second son of Brian and Brenda Fillingim. In 1980 his family and he packed up and moved to Vincennes, IN. There he graduated from Lincoln High School as salutatorian in 1991. After graduation he attended Florida Institute of Technology in Melbourne, FL, where he earned a Bachelor of Science in Space Sciences in 1995 (and a spouse in 1996) and a Master of Science in Space Sciences in 1997. He finally received his *Philosophiae Doctor* in Geophysics at the University of Washington in the early months of 2002. After a brief hiatus in the Southern Hemisphere that purposefully had absolutely nothing to do with science, his wife and he moved yet again so that he could work at the University of California, Berkeley.